University of Southern Queensland

EFFECT OF FIBRE DISTRIBUTION ON STRUCTURAL BEHAVIOUR OF PULTRUDED COMPOSITE PROFILES

A Thesis submitted by

Songming Qi

MSC (Civil/Structural), BSc (Civil)

For the award of

Doctor of Philosophy

2023

ABSTRACT

Fibre-reinforced polymer (FRP) composites are widely used in various industries due to their high strength-to-weight ratio, corrosion resistance, and tailored mechanical properties. However, manufacturing-induced imperfections, such as non-uniform fibre distribution (NUFD), voids, and fibre waviness, can compromise their performance and structural integrity. This thesis comprehensively investigates fibre distribution imperfections in hollow box FRP structures, focusing on manufacturing, characterization, and performance analysis to enhance the understanding of their impact on mechanical properties and structural behaviour. A novel approach, Filtered Canny Misalignment Analysis (FCMA), is introduced for characterizing fibre waviness in continuous fibre-reinforced composites, demonstrating improved accuracy, efficiency, and robustness compared to existing methods. The FCMA method is applied to quantify in-plane and out-of-plane fibre waviness in hollow composite columns, which is then used as input for a finite element model to evaluate the impact of fibre waviness on stress distribution under axial compression. The formation and impact of Non-Uniform Fibre Distribution (NUFD) in pultruded fibre-reinforced polymer (PFRP) composite profiles are investigated using image analysis and experimental testing. It is demonstrated that compressive strength at the material level decreases proportionally with the fibre volume fraction caused by NUFD, while finite element modelling highlights corner defects generated by NUFD at the full-scale structural level are more sensitive to local buckling failure compared to wall defects. The effect of NUFD on the flexural performance of pultruded glass FRP box beams is investigated, revealing that corner NUFD has a greater negative impact on local buckling capacity than flange NUFD. A linear relationship between the rotational restraint coefficient and corner fibre volume fraction is established, providing insight into the influence of material imperfections on load capacity. Finally, a numerical simulation and experimental investigation of the pull-braiding process for manufacturing braided composite profiles are conducted. A bi-axial braiding technique combined with pultrusion is employed, and the developed numerical model accurately simulates the braiding process, predicting the geometrical features of the braided structures. The study identifies defects in the composite profiles, providing a foundation for future research in the development of advanced composite materials with tailored mechanical properties.

CERTIFICATION OF THESIS

I ***Songming Qi*** declare that the PhD Thesis entitled ***EFFECT OF FIBRE DISTRIBUTION ON STRUCTURAL BEHAVIOUR OF PULTRUDED COMPOSITE PROFILES*** is not more than 100,000 words in length including quotes and exclusive of tables, figures, appendices, bibliography, references, and footnotes.

This Thesis is the work of ***Songming Qi*** except where otherwise acknowledged, with the majority of the contribution to the papers presented as a Thesis by Publication undertaken by the student. The work is original and has not previously been submitted for any other award, except where acknowledged.

Date: 20 May 2023

Endorsed by:

Professor Xuesen Zeng
Principal Supervisor

Omar Alajarmeh
Associate Supervisor

Tristan Shelley
Associate Supervisor

Professor Peter Schubel
Associate Supervisor

Student and supervisors' signatures of endorsement are held at the University.

STATEMENT OF CONTRIBUTION

The articles produced from this study were a joint contribution of the authors. The details of the scientific contribution of each author are provided below:

Paper 1:

Songming Qi, Omar Alajarmeh, Tristan Shelley, Peter Schubel, Kendric Rendle-Short, Xuesen Zeng, (2023), Fibre waviness characterisation and modelling by Filtered Canny Misalignment Analysis (FCMA), Composite Structures. Vol. 307, p. 116666. IF：6.603.

DOI: https://doi.org/10.1016/j.compstruct.2023.116666

The overall contribution of Songming QI was 65% related to the conceptualisation, methodology, design of experiments, experimental works, data collection and curation, software, analysis and interpretation of data, writing the original draft and revising the final submission. Xuesen Zeng, Peter Schubel, Omar Alajarmeh, Tristan Shelley, and Kendric Rendle-Short contributed to the concept development, design of experiments, reviewing, editing, and providing important technical advice.

Paper 2:

Qi S, Alajarmeh O, Shelley T, Schubel P, Rendle-Short K, Zeng X. Formation of non-uniform fibre distributions in winding-pultrusion process and its effect on axial compressive properties of hollow GFRP profiles. Composites Part A: Applied Science and Manufacturing. 2023;173:107659. IF：9.463.

DOI: https://doi.org/10.1016/j.compositesa.2023.107659

The overall contribution of Songming QI was 70% related to the conceptualisation, methodology, design of experiments, experimental works, data collection and curation, software, analysis and interpretation of data, writing the original draft and revising the final submission. Xuesen Zeng, Peter Schubel, Omar Alajarmeh, Tristan Shelley, and Kendric Rendle-Short contributed to the concept development, design of experiments, reviewing, editing, and providing important technical advice.

Paper 3:

Songming Qi, Omar Alajarmeh, Mohammad Alhawamdeh, Tristan Shelley, Peter Schubel, Kendric Rendle-Short, Xuesen Zeng, (2023) “Formation of non-uniform fibre distribution and its effect on the flexural performance of pultruded GFRP box beams” Submitted to Composite Structures. IF：6.603. (Minor revision)

The overall contribution of Songming QI was 65% related to the conceptualisation, methodology, design of experiments, experimental works, data collection and curation, software, analysis and interpretation of data, writing the original draft and revising the final submission. Xuesen Zeng, Peter Schubel, Omar Alajarmeh, Mohammad Alhawamdeh, Tristan Shelley, and Kendric Rendle-Short contributed to the concept development, design of experiments, reviewing, editing, and providing important technical advice.

ACKNOWLEDGEMENTS

I am deeply grateful to my principal supervisor, Professor **Xuesen Zeng**, for their unwavering support and mentorship throughout my research. His expertise and guidance have been invaluable in shaping my ideas and approaches to the project. Special thanks and gratitude to my associate supervisor Professor **Peter Schubel** and Dr **Tristan Shelley** for their help and support. Their constructive feedback has helped me to refine and improve my work at every stage.

Dr **Omar Alajarmeh** has been a constant source of encouragement and inspiration. His enthusiasm for the subject matter and his passion for teaching and research have inspired me to work harder and aim higher, even when the going got tough.

My sincere appreciation to **Wagner CFT** for their generous support and collaboration throughout my research. Their contribution to materials and expertise in the production process has been invaluable in the successful completion of this project.

I would also like to thank my **family** for their unwavering support and understanding during the ups and downs of my academic journey. Their love and encouragement have been a constant source of strength and inspiration.

I would like to acknowledge the help and support of my friends and colleagues at USQ, especially in the **Centre of Future of Materials**, whose advice and assistance have been invaluable in shaping my ideas and refining my research.

Finally, The work was funded through a Cooperative Research Centres Projects (CRC - P) Grant and has been supported by the UniSQ scholarships

TABLE OF CONTENTS

LIST OF TABLES

LIST OF FIGURES

ABBREVIATIONS

CSMs: continuous strand mats

DIC: digital image correlation

FE: finite element

FEA: finite element analysis

FEM: finite element method

FRP: fibre-reinforced polymer

FCMA: filtered Canny misalignment analysis

FLB: flange local buckling

GFRP: glass fibre-reinforced polymer

GWT: guided wave testing

NDT: non-destructive technique

NUFD: non-uniform fibre distribution

PFRP: pultruded fibre-reinforced polymer

PAUT: phased array ultrasonic testing

RTM: resin transfer moulding

SEM: scanning electron microscopy

T4L: Transportation 4 Life

UD: unidirectional

VOIs: volume of interests

CHAPTER 1: INTRODUCTION

1.1. Background

Fibre-reinforced polymer (FRP) composites are increasingly utilised in various industries, including aerospace, automotive, and construction, due to their high strength-to-weight ratio, corrosion resistance, and ability to tailor their mechanical properties (Starr & Ketel, 2000). Among the manufacturing processes, pultrusion has gained prominence for civil structure applications in the last decade due to its highly automated, low-cost, and high-quality control process. The integration of pull-winding or pull-braiding technology has marked a significant advancement in pultrusion, enhancing the lateral properties of FRP composites through the continuous winding of fibres (Al-saadi, Aravinthan, & Lokuge, 2019; Alajarmeh et al., 2021; Hoa, 2009).

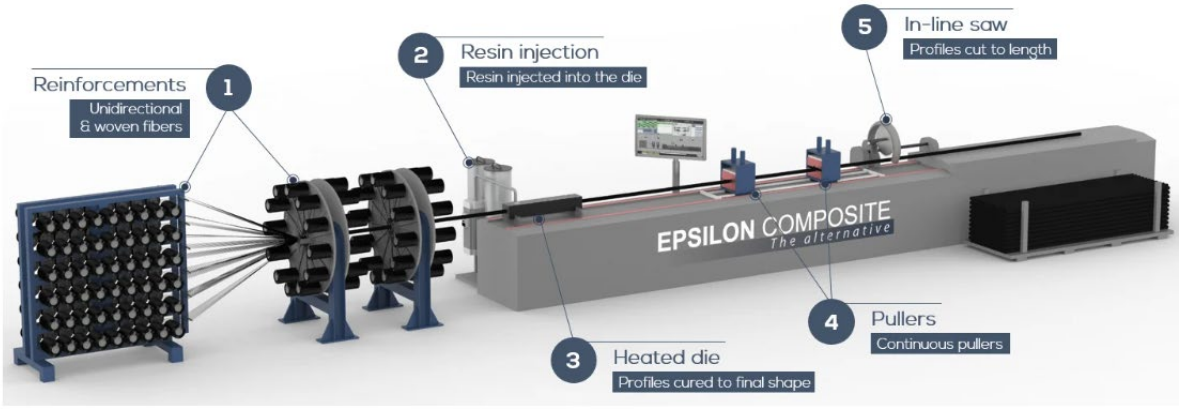

Figure 1.1. Illustration of pull-winding pultrusion process (Epsilon Composite).

Figure 1.1 illustrates a typical pull-winding production line, consisting of pull-winding fibre delivery and pultrusion systems. The manufacturing process can be divided into two primary stages. In the first stage, dry fibre preforms are produced by winding fibres around a mandrel. The circular mandrel shape in the preform section is often utilized to enhance winding stability and achieve uniform tension distribution. During the second stage, the dry fibre preforms undergo resin infusion, where they are impregnated with a resin matrix to create a composite material. After the resin infusion, the composite undergoes a curing process to harden the material, followed by cutting it into the desired lengths.

These pultruded fibre-reinforced polymer composites have been developed for various applications (see Figure 1.2) as they are well-suited to endure harsh environments, requiring

minimal maintenance and offering long-lasting benefits to local communities. These materials are particularly suitable for use in coastal, marine, and environmentally sensitive areas.

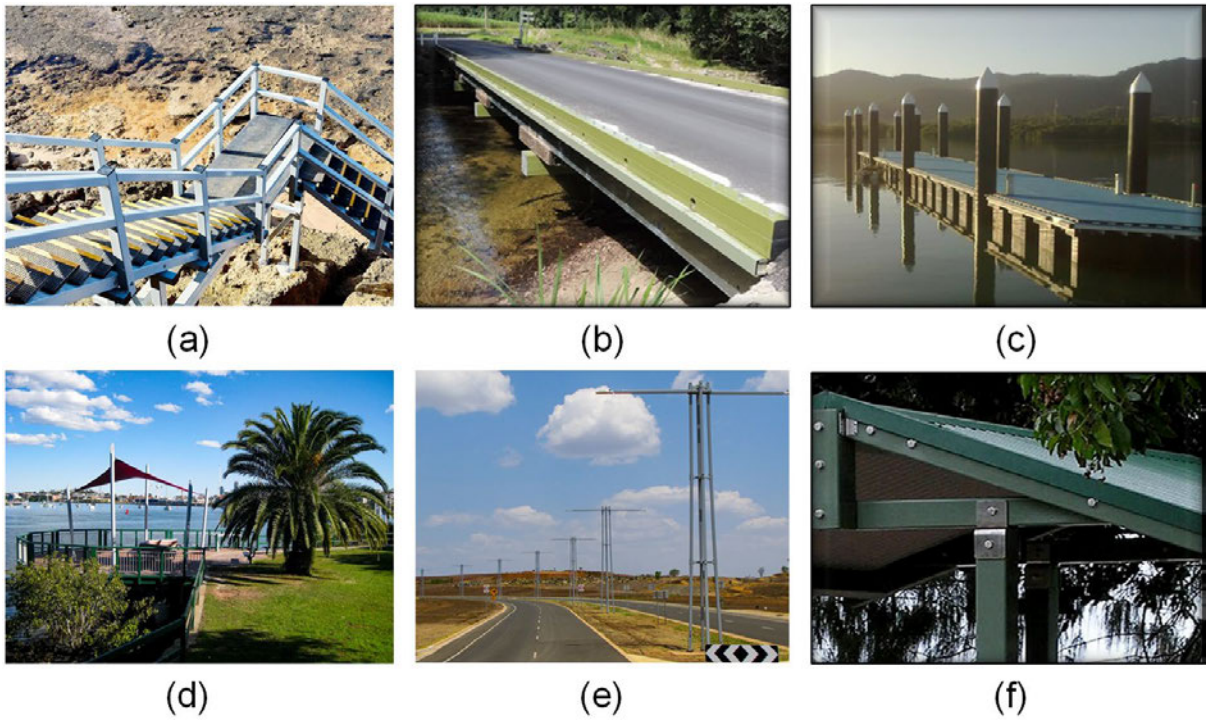

Figure 1.2. Some applications of hollow fibre reinforcement composites are (a) pedestrian infrastructures, (b) traffic, (c) marine infrastructures, (d) viewing platforms, (e) light poles and (f) shelters (Wagners CFT n.d.).

The pultrusion process can however introduce imperfections and defects in the composite products, which may adversely affect their mechanical properties and structural integrity, as shown in Figure 1.3 (Bunsell, 2009; Poulton & Sebastian, 2021; M. Wisnom, 1999). One of the most common imperfections in FRP composites is the non-uniform fibre distribution (NUFD), which can arise from variations in the fibre volume fraction or fibre misalignment during the manufacturing process. NUFD can lead to localised stress concentrations, reduced load-bearing capacity, and premature failure in FRP structures. Other manufacturing-induced defects, such as voids and fibre waviness, can also compromise the structural performance of these materials. Thus, understanding the occurrence, characterisation, and effects of these imperfections is essential for designing and manufacturing reliable, high-performance FRP structures.

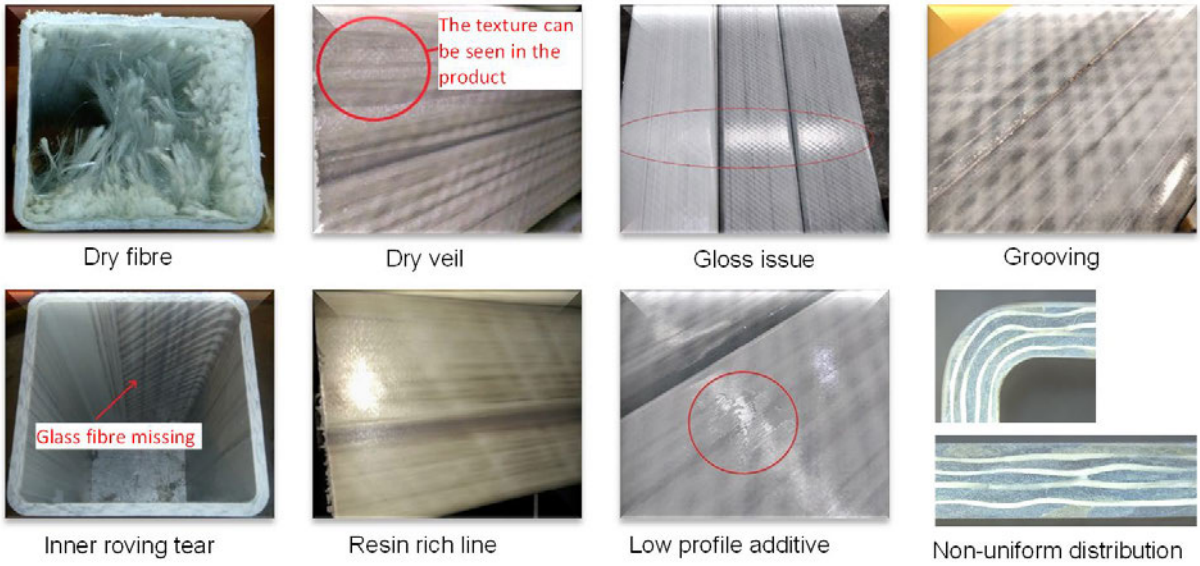

Figure 1.3. Common defects in pultruded composites (Wagners CFT n.d.).

1.2. Problem statement

These hollow FRP profiles are susceptible to buckling due to their slender nature and anisotropic material properties (Reddy, 2003), especially from local buckling. Due to the low stiffness and anisotropic nature of pultruded FRP (PFRP), deformation and buckling instability are commonly observed in structures subjected to axial and flexural loading, particularly in thin-walled structures (Debski, Rozylo, & Teter, 2020; Madenci, Onuralp Özkılıç, & Gemi, 2020). Local buckling, which occurs prior to material failure, is a critical factor in predicting the structural capacity of the PFRP sections (Ascione, Berardi, Giordano, & Spadea, 2015; Cardoso, Harries, & Batista, 2014b; Matthews, Davies, Hitchings, & Soutis, 2000). Figure 1.4 shows the progressive failure mode of local buckling in the hollow FRP profile (Alhawamdeh et al., 2021).

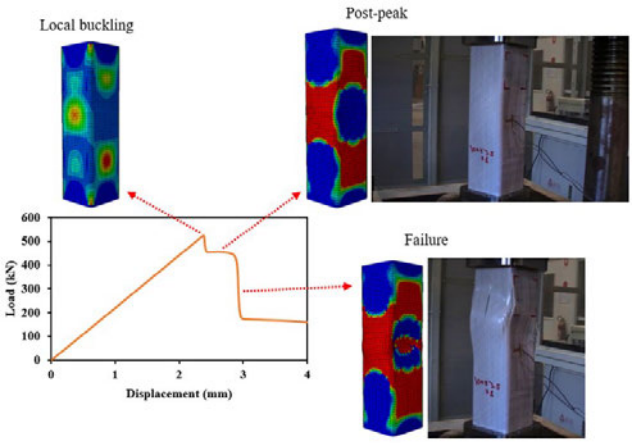

Figure 1.4. Compressive behaviour of hollow box PFRP profile (Alhawamdeh et al., 2021).

Many studies on PFRP composites have assumed that the unidirectional (UD) plies are uniform and defect-free (Barbero, 2010). However, the use of continuous strand mats (CSMs) or wound fibre plies results in NUFD. This phenomenon was noted from the cross-section of profiles and quantified by the variations in the local fibre volume fraction (Feng, Wu, & Liu, 2021; Poulton & Sebastian, 2021; Yuksel, Sandberg, Hattel, Akkerman, & Baran, 2021). The NUFD is always accompanied by resin-rich pockets, mat wrapping errors, cracks, and roving shifts, which affect mechanical properties (Bednarcyk, Aboudi, & Arnold, 2014; Ghayoor, Marsden, Hoa, & Melro, 2019; Li, Stier, Bednarcyk, Simon, & Reese, 2016; Potter, Khan, Wisnom, Bell, & Stevens, 2008; Safonov et al., 2020). While the impact of defects such as NUFD on local buckling has been acknowledged, there is a limited understanding of how fibre distribution imperfections influence the mechanical properties and structural behaviour of these materials, particularly in the context of hollow box structures.

1.3. Research objectives

This thesis aims to investigate the formation of fibre distribution imperfections, such as the NUFD and fibre waviness, in hollow box FRP structures and their impact on the mechanical performance and structural behaviour under various loading conditions. The specific objectives of the thesis are as follows:

- To review the literature on the effect of fibre distribution imperfections on the buckling characteristics of hollow box FRP structures (Chapter 2).
- To develop and evaluate a novel method for characterising and quantifying fibre waviness in continuous fibre-reinforced composites (Chapter 3).
- To investigate the formation of NUFD in the winding-pultrusion process and its effect on axial compressive properties of hollow glass fibre-reinforced polymer (GFRP) profiles (Chapter 4).
- To study the effect of NUFD on the flexural performance of pultruded GFRP box beams (Chapter 5).
- To develop a numerical model and conduct an experimental investigation on the pull-braiding process for manufacturing braided composite profiles (Chapter 6).

1.4. Scope and limitations

This research has been conducted with a focus on the pultrusion manufacturing process, specifically using pull-winding and pull-braiding technologies, and their impact on the mechanical performance and structural behaviour of FRP composites. The structural behaviour investigated in this research focuses on local buckling, which is a critical failure mode for hollow box FRP structures. It is essential to differentiate local buckling from global buckling and lateral-torsional buckling, as each of these failure modes has unique characteristics and implications for the design and performance of the structures. Although the findings of this research are expected to provide valuable insights and guidelines for the design and manufacturing of reliable and high-performance hollow box FRP structures, some limitations should be considered:

- The research focuses on glass-fibre pultruded FRP composites, as they represent a significant portion of the FRP materials used in various industries. The study only considers pultrusion manufacturing processes using pull-winding and pull-braiding technologies. Other manufacturing techniques, such as filament winding, resin transfer moulding, or vacuum-assisted resin infusion, are not within the scope of this research.
- The study considers axial compression and bending loads as the primary load cases, as these are most relevant to the structural applications of the investigated materials.
- This research involves the development and validation of novel characterisation techniques for non-uniform fibre distribution (NUFD) and fibre waviness, which cannot be used to characterise other defects such as cracks and thickness variations.
- The research primarily focuses on the effects of fibre distribution imperfections on the mechanical performance and structural behaviour of hollow box FRP structures. Other types of imperfections, such as delamination and matrix cracking, are not the primary focus of this thesis.
- The study does not consider the long-term performance of the FRP composites, such as the effects of environmental factors (e.g., temperature, moisture) or fatigue, on the mechanical properties and structural behaviour of the materials.

Despite these limitations, this research is expected to provide valuable insights and guidelines for the design and manufacturing of reliable and high-performance hollow box GFRP structures in various industries. Moreover, the research outcomes may serve as a

foundation for future studies exploring other types of FRP materials, manufacturing techniques, and composite structures.

1.5. Thesis organisation

This research work is presented as a thesis by publication. This thesis is organised into seven chapters, as shown in Figure 1.5.

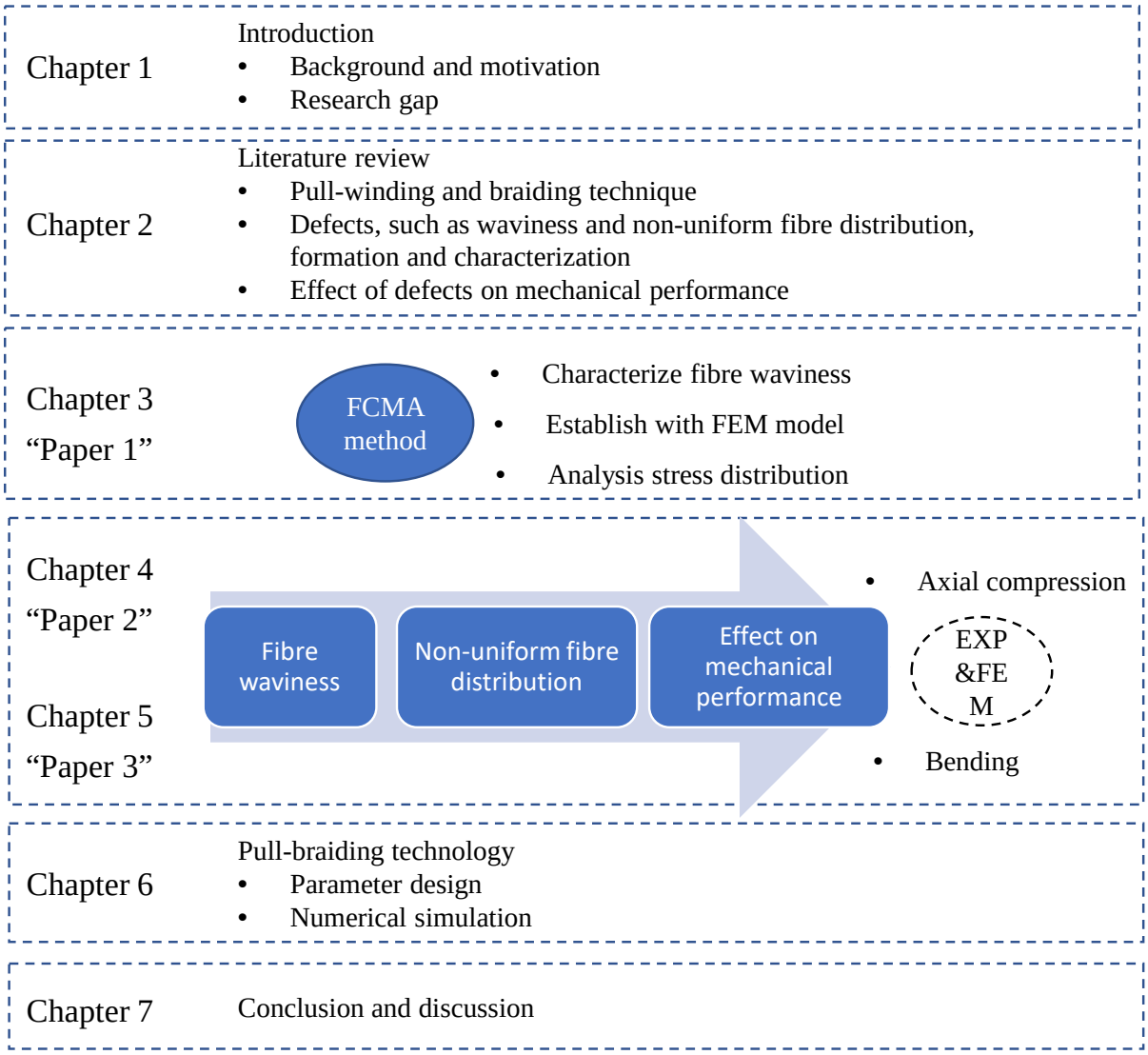

Figure 1.5. Thesis flow chart.

The introduction provides the background, objectives, and outline of the thesis in Chapter 1. Chapter 2 presents a comprehensive literature review of the factors influencing the formation of fibre distribution imperfections and their impact on the buckling behaviour of hollow box FRP structures. Chapter 3 proposes a novel approach for characterising fibre waviness in continuous fibre-reinforced composites and compares it with existing methods.

Chapter 4 investigates the formation and impact of NUFD in PFRP composite profiles and their effect on the compressive behaviour at material and structure levels. Chapter 5 explores the influence of NUFD on the mechanical properties of hollow pultruded GFRP profiles under bending. Chapter 6 presents a comprehensive investigation into the pull-braiding process for manufacturing braided composite profiles and develops a numerical model to predict the geometrical features of the braided structures. Chapter 7 provides a summary of the research findings, conclusions, and recommendations for future research.

CHAPTER 2: REVIEW OF THE EFFECT OF FIBRE DISTRIBUTION IMPERFECTIONS ON THE STRUCTURAL BEHAVIOUR OF OF HOLLOW BOX FRP STRUCTURES

2.1. Introduction

2.1.1. Background and motivation

Fibre-reinforced polymer (FRP) composites have gained widespread recognition in various industries due to their remarkable properties, including a high strength-to-weight ratio, superior corrosion resistance, and design versatility (Guades, Aravinthan, Islam, & Manalo, 2012; L. Hollaway, 2010; A P Mouritz, Bannister, Falzon, & Leong, 1999). In particular, hollow box FRP structures have become increasingly popular in civil, aerospace, automotive, and marine sectors as load-bearing components, providing lightweight and efficient structural solutions (Bank, 2006; Uddin, 2013).

The growing popularity of hollow box FRP structures can be attributed to their exceptional performance characteristics, such as high strength-to-weight ratio, and design flexibility (Gibson, 2016; L. Hollaway, 2010). These structures have been extensively employed across civil, aerospace, automotive, and marine applications for a variety of structural components, including beams, columns, bridge decks, and ship hulls (Bank, 2006; Vasiliev & Morozov, 2001). The lightweight and efficient nature of hollow box FRP structures delivers significant advantages, including reduced material consumption, decreased installation time, enhanced fatigue resistance, and lower maintenance costs in comparison to traditional materials like steel and concrete (Bakis et al., 2002; Ramôa Correia, 2013).

Despite their numerous advantages, FRP structures can exhibit various fibre distribution imperfections, such as non-uniform fibre distribution (NUFD), fibre waviness, and misalignment, which can arise during manufacturing processes (Hassan, Othman, & Kamaruddin, 2017; Jeong, 1997). These imperfections may lead to reduced mechanical performance, including buckling behaviour (Barati & Zenkour, 2017; Barbero, 2010; Mahadik & Hallett, 2011; Mukhopadhyay, Jones, & Hallett, 2015). Buckling is a critical failure mode for hollow box FRP structures under compressive or bending loads, and understanding the impact of fibre distribution imperfections on buckling is essential for ensuring structural stability and performance (Bayat & EkhteraeiToussi, 2017; Kubiak, Kolakowski, Swiniarski, Urbaniak, & Gliszczynski, 2016; P. Liu et al., 2011; Madenci et al., 2020).

2.1.2. Scope and objectives of the review

The primary objective of this review chapter is to provide a comprehensive analysis of the existing literature on the effect of fibre distribution imperfections on the buckling behaviour of hollow box FRP structures. This review will cover the following aspects:

- Overview of hollow box FRP structures, their applications, and manufacturing techniques.
- Types of fibre distribution imperfections and their characterisation.
- Theoretical models, experimental investigations, and numerical simulations of buckling behaviour of hollow box FRP structures.
- The effect of fibre distribution imperfections on the buckling, and future research directions.

This chapter is organised into the following sections: Section 2.2 provides an overview of hollow box FRP structures, including their applications and manufacturing techniques. Section 2.3 discusses the types of fibre distribution imperfections and their characterisation. Section 2.4 covers the buckling behaviour of hollow box FRP structures and the impact of fibre distribution imperfections on the buckling, including theoretical models and numerical simulations. Section 2.5 presents future research directions and conclusions derived from this review.

2.2. Manufacturing of hollow box FRP structures

2.2.1. Development of FRP composites

Polymer composites, known for their high strength-to-weight ratio, first gained attention in the military and aerospace industries during the 1940s (Gand, Chan, & Mottram, 2013). Composites gained more widespread use in the aerospace industry, with the introduction of carbon fibres in the 1960s leading to further improvements in strength and stiffness (Callister & Rethwisch, 2007). As materials technology advanced, these composites found their way into the building industry in the 1970s, primarily for non-load bearing and semi-load bearing applications. The use of composites for semi-structural applications, like bridge decks and building facades, began in the 1980s (L. C. Hollaway, 2001). With ongoing research and development, FRP composites started to be used in primary structural components in civil applications, such as beams, columns, and slabs, in the 1990s. Over the last 20 years, significant advancements in composite materials have been made in terms of improved manufacturing

techniques, enhanced material properties, and broader applications, particularly in the civil engineering and infrastructure sectors (Bank, 2006).

FRP composites used in hollow box structures typically consist of reinforcing fibres, such as glass, carbon, or aramid fibres, embedded in a polymer matrix, such as epoxy, polyester, or vinyl ester (Clyne & Hull, 2019). The combination of reinforcing fibres and matrix materials determines the overall mechanical properties, durability, and thermal performance of the FRP structures (Cantwell & Morton, 1991; Karbhari, 2007; Rajak, Pagar, Kumar, & Pruncu, 2019). Hybrid FRP composites, which incorporate two or more types of fibres or matrices, can provide tailored properties and improved performance for specific applications (Zweben, 1998).

Various manufacturing techniques have been developed to produce FRP structures, each with its advantages and limitations in terms of cost, quality, and production rate (Gibson, 2010; Vaidya & Chawla, 2008). Some of the most common manufacturing methods include hand lay-up (Advani & Sozer, 2002; Avila & Morais, 2005), vacuum bagging (Mujahid, Sallih, Mustapha, Abdullah, & Mustapha, 2020; Muralidhara, Babu, & Suresha, 2020), filament winding (Azeem et al., 2022; Zu, 2012), resin transfer moulding (RTM) (Cheng et al., 2010; Shojaei, Ghaffarian, & Karimian, 2003) and pultrusion (Correia, 2023). Each manufacturing method can introduce specific fibre distribution imperfections, which can affect the mechanical performance and buckling behaviour of the resulting hollow box FRP structures. Understanding and addressing these imperfections are crucial for optimising the design and performance of these structures (Abdurohman, Satrio, & Muzayadah, 2018; Potter et al., 2008).

2.2.2. Pull-winding and pull-braiding techniques

Pultrusion is a continuous, automated manufacturing process that offers numerous advantages for producing fibre-reinforced polymer (FRP) composites, including hollow composite profiles, with consistent cross-sectional shapes, as shown in Figure 2.1. This method is characterised by its high production rate, uniform quality, better fibre alignment, reduced waste, and lower production costs compared to other manufacturing techniques such as hand lay-up, resin infusion, and filament winding (Baran, 2015; Fairuz, Sapuan, Zainudin, & Jaafar, 2014; Ramôa Correia, 2013). Furthermore, pultrusion accommodates a wide range of fibre and resin combinations, enabling the creation of tailored composite profiles for specific applications across various industries, such as civil, aerospace, automotive, and marine sectors (Philippe Boisse, 2015).

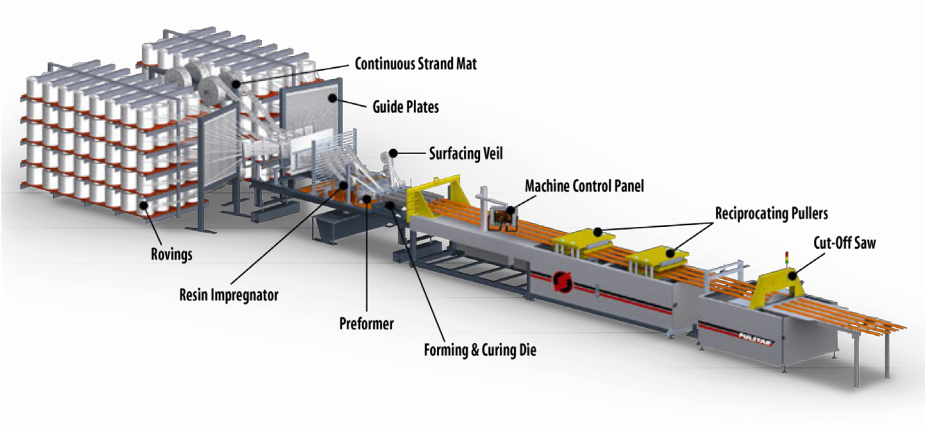

Figure 2.1. Schematic image of the pultrusion process (Strongwell).

The integration of pull-winding or pull-braiding technology has been a notable advancement in pultrusion, enhancing the lateral properties of FRP composites through the continuous winding of fibres (Al-saadi et al., 2019; Alajarmeh et al., 2021; Hoa, 2009). Figure 2.2 illustrates a typical pull-winding production line, consisting of pull-winding fibre delivery and pultrusion systems. The manufacturing process can be divided into two primary stages. In the first stage, dry fibre preforms are produced by winding fibres around a mandrel. The circular mandrel shape in the preform section is often utilized to enhance winding stability and achieve uniform tension distribution. During the second stage, the dry fibre preforms undergo resin infusion, where they are impregnated with a resin matrix to create a composite material. After the resin infusion, the thermoset polymer undergoes a curing process to harden the material, followed by cutting it into the desired lengths[1].

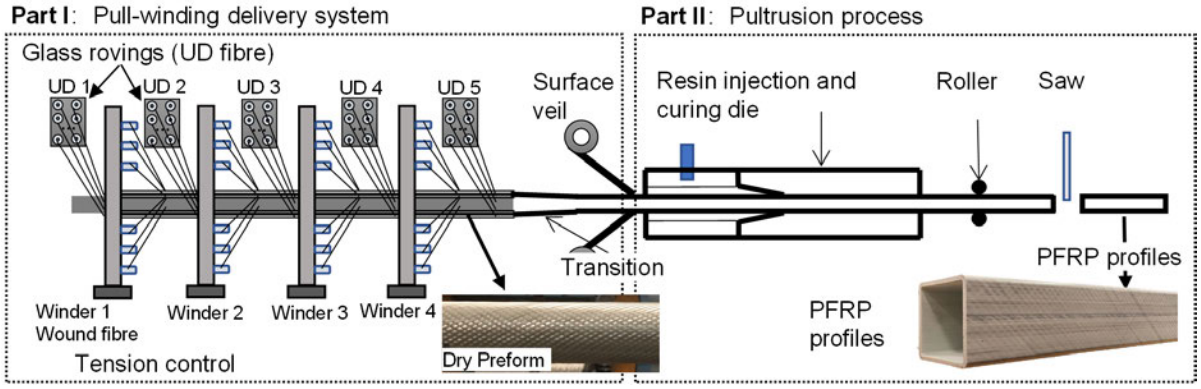

Figure 2.2. Illustration of pull-winding pultrusion process with a die-injection

A transition section can be implemented in the production line to convert the circular cross-section of the preform into a square or rectangular cross-section, while maintaining equal

[1] The process is slightly modified for thermoplastic pultrusion – however due to the scope of this thesis it will not be described or explored in any detail.

circumferential perimeters. This transition is crucial for creating hollow box FRP structures with the desired geometries that are not circular.

In the final products, it is common to observe the presence of wrinkles in the wound fibres, particularly at the corners of square or rectangular profiles. These wrinkles can arise due to various factors, such as uneven tension during winding, resin shrinkage during curing, and fibre misalignment. These imperfections can lead to non-uniform fibre distributions in the composite, potentially affecting its mechanical performance and buckling behaviour. Researchers and manufacturers are continually exploring ways to minimise these defects and improve the overall quality of the composite profiles.

2.3. Fibre Distribution Imperfections

2.3.1. Types of fibre distribution imperfections

Fibre distribution imperfections in FRP composites can be classified into several types, including non-uniform fibre distribution, fibre waviness, fibre misalignment, fibre volume fraction variation, void content, and resin-rich or resin-starved areas (Potter et al., 2008). These imperfections can adversely affect the mechanical properties and overall performance of FRP structures, including their buckling behaviour (Heinecke & Willberg, 2019; Rouf, Worswick, & Montesano, 2021; Trask, Hallett, Helenon, & Wisnom, 2012).

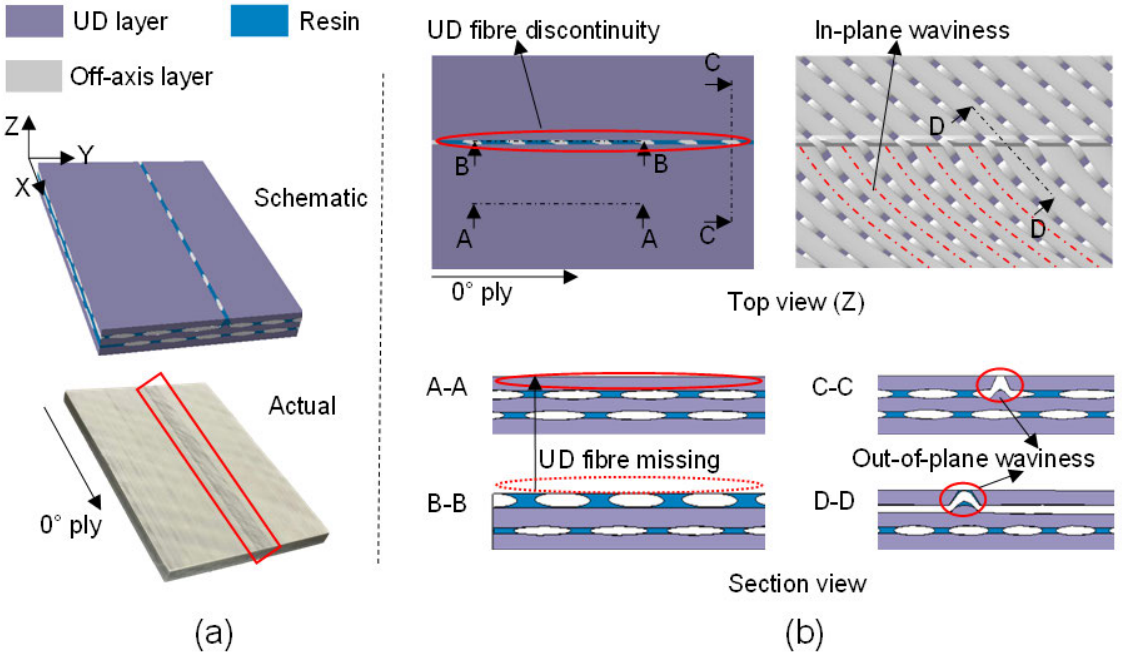

Figure 2.3. Schematic of the UD fibre discontinuity; (a) samples of the FRP profile and (b) defects description from the different cutting sections.

A typical NUFD induced during the pull-winding process is shown in Figure 2.3. There is an apparent fibre discontinuity of the outermost unidirectional ply on the surface of the FRP

profile in Figure 2.3(a), which manufacturers usually reject due to cosmetic and strength concerns. The cross-sections in Figure 2.3(b) show various defects, including in-plane waviness, missing unidirectional fibres and out-of-plane waviness. The NUFD is frequently accompanied by in-plane and out-of-plane waviness of the off-axis ply.

2.3.2. Mechanism of fibre distribution imperfection formation

Previous research has investigated the mechanisms underlying waviness formation in FRP composites using experimental approaches (Hallander, Akermo, Mattei, Petersson, & Nyman, 2013; Lightfoot, Wisnom, & Potter, 2013b; Nosrat Nezami, Gereke, & Cherif, 2016) and numerical methods (Naouar, Vidal-Salle, Schneider, Maire, & Boisse, 2014; Sjölander, Hallander, & Åkermo, 2016; Adam J. Thompson, Belnoue, & Hallett, 2020). Fibre distribution imperfection has been found to negatively impact the mechanical performance of composites, particularly in terms of compressive and tensile strength (Alves, Cimini Junior, & Ha, 2021; Kulkarni, Mali, & Singh, 2020), and it also affects the initiation and propagation of damage (Carraro, Maragoni, & Quaresimin, 2015). In the context of pull-wound hollow FRP profiles, fibre waviness in the off-axis ply interacts with unidirectional plies, leading to fibre disturbances manifested as NUFD. To avoid and reduce the occurrence of these defects, the mechanism and influence factors should be investigated and understood (Gupta, 2007).

The shear force resulting from slippage between yarns causes the yarn to turn over, as illustrated in Figure 2.4. The shear deformation of the yarn is assumed to be dominated by individual fibres sliding against each other, which affects the section deformation. When the yarn is subjected to compression, its cross-sectional shape changes, leading to alterations in the overall thickness and width of the ply. Consequently, the contact ply forms wrinkling (Lightfoot, Wisnom, & Potter, 2013a).

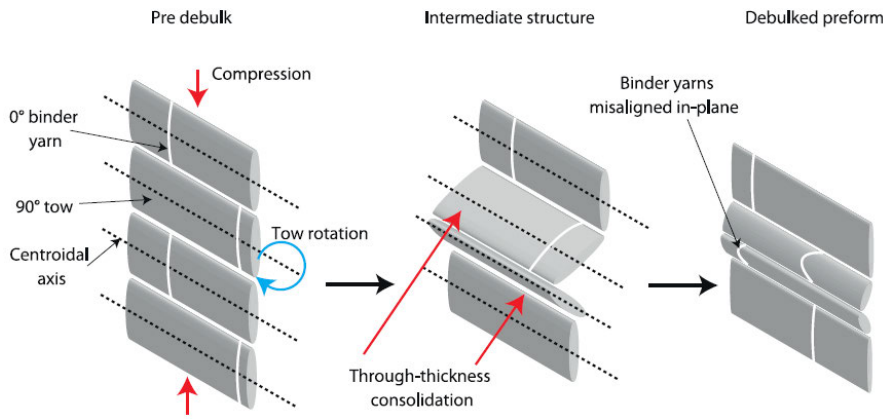

Figure 2.4. Tow wrinkling of 90 ^{o} tows and in-plane waviness of 0^{o} binder yarns is a result of compressive forces and subsequent tow rotation (Lightfoot et al., 2013a).

In thick composite parts, wrinkles form during consolidation due to excess material length. This phenomenon becomes more severe as compaction increases. As illustrated in Figure 2.5, if the ply ends are unconstrained and free, the laminate can slip between layers, creating a 'book end effect' as shown in Figure 2.5(a). However, in real manufacturing processes, friction is not zero, and yarns are prevented from slipping over one another. Consequently, excess length forms wrinkles and buckling, which reduce the mechanical performance, as shown in Figure 2.5(b) (J. P. H. Belnoue et al., 2018). For compaction over male radii, the excess length, resulting from the change in thickness, can be calculated using Eq. 2.1.

$$L_{\mathrm{ex}} = 2\pi\Delta t/4 \tag{2.1}$$

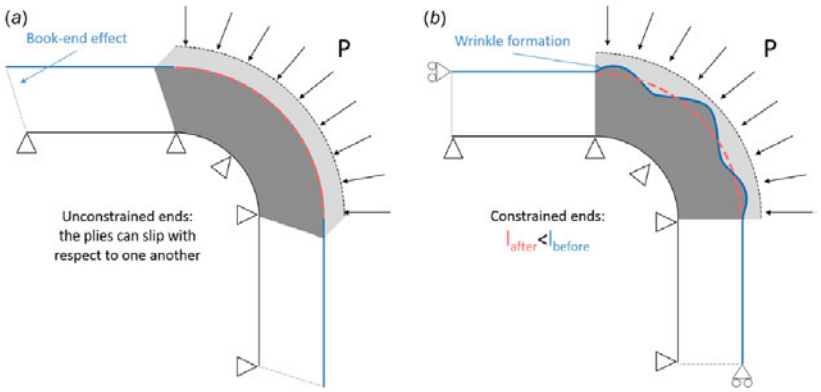

Figure 2.5. A schematic of the consolidation of prepreg stacks over curved tools (J. P. H. Belnoue et al., 2018).

The mechanisms behind this phenomenon have been investigated through analytical and numerical models to eliminate such defects. An analytical model describing out-of-plane wrinkling was developed by (Dodwell, Butler, & Hunt, 2014). Wrinkles occur if the limb length exceeds the critical limb length derived from the model. The critical length is primarily determined by layer thickness and shear properties. The mechanisms for fibre path defects during the processing of thick composite prepreg materials have been investigated using numerical models (Jonathan P. H. Belnoue & Hallett, 2020; J. P. H. Belnoue et al., 2018; Hallander et al., 2013; Nosrat Nezami et al., 2016; Adam J. Thompson, McFarlane, Belnoue, & Hallett, 2020). These models examined the influence of resin viscosity, interplay friction coefficient, and bending stiffness on the formation of defects.

2.3.3. Common factors affecting fibre distribution imperfections

Various factors can contribute to the formation of fibre distribution imperfections in FRP composites, including manufacturing techniques, material properties, processing parameters, tooling and equipment and human factors.

Different manufacturing processes, such as hand lay-up, vacuum bagging, filament winding, resin transfer moulding, and pultrusion, can introduce specific types of fibre distribution imperfections due to the inherent limitations and challenges associated with each method (Mazumdar, 2001; Vaidya & Chawla, 2008). Material properties, such as fibre stiffness, matrix viscosity, and curing behaviour, can influence the formation of fibre distribution imperfections during manufacturing (Adrian P Mouritz & Gibson, 2007). Processing parameters, including temperature, pressure, and curing time can affect the consolidation and curing of the composite material, leading to the formation of voids, resin-rich or resin-starved areas, and non-uniform fibre distribution (Baran, Tutum, Nielsen, & Hattel, 2013). The design and condition of moulds, mandrels, and other tooling used in the manufacturing process can influence fibre orientation and distribution, potentially leading to imperfections like fibre misalignment or waviness (Correia, 2023). In manual processes like hand lay-up, the skill and experience of the operator play a critical role in determining the quality of the final composite structure, including the occurrence of fibre distribution imperfections (Advani & Hsiao, 2012).

Composite parts with curvatures can induce in-plane waviness, out-of-plane waviness and wrinkling, depending on the tow constraint. The mechanisms behind these defects have been investigated in several studies (Dodwell et al., 2014; Lightfoot et al., 2013a; Mizukami et al., 2016). Figure 2.6 shows that the friction shear force caused by the consolidation of the plies will result in two defects: in-plane tow waviness and tow crushing (Lightfoot et al., 2013b). Depending on the constraint in the Z direction, out-of-plane deformation or in-plane waviness may occur due to the compression of a tow, as shown in Figure 2.7 (Lightfoot et al., 2013a).

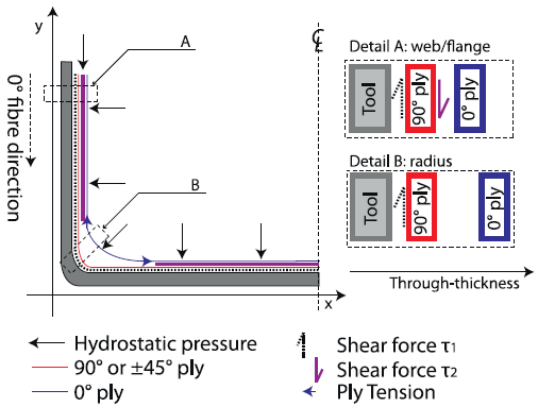

Figure 2.6. Free body diagram showing the result of a bridged ply over a well-formed ply in one half of a U-shaped tool (Lightfoot et al., 2013b).

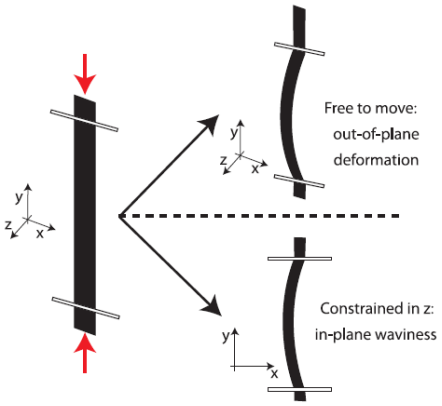

Figure 2.7. ln-plane and out-of-plane tow waviness forms in cloths during compression (Lightfoot et al., 2013a).

Dry fibre materials are anisotropic and can be considered transversely isotropic for a yarn. The longitudinal deformation and bending behaviour of these materials are decoupled, which differs from traditional material theory (Green, Long, El Said, & Hallett, 2014; Long, 2005). To address this issue, a superimposed mesh is often used in FEM simulations (Nishi, 2015; Adam J. Thompson, McFarlane, et al., 2020; Yu et al., 2020). The longitudinal Young's modulus of the fibre is large enough to be treated as quasi-inextensible. However, the bending stiffness of dry fibre is significantly lower. These properties indicate that standard shell theory is not suitable for simulations, and the slippage between fibres leading to bending behaviour has a considerable impact on wrinkling formation (P. Boisse, Colmars, Hamila, Naouar, & Steer, 2018; P. Boisse, Hamila, & Madeo, 2016; Liang, Hamila, Peillon, & Boisse, 2014). Under longitudinal compression, different bending stiffnesses will exhibit varying behaviour, as demonstrated by the sensitivity analysis of forming simulations on bending stiffness in Figure 2.8. The proper constitutive law of the material and model elements are crucial for accurately describing fibre material behaviour in simulations.

Figure 2.8. (a) Wrinkling in compression of a woven reinforcement strip with different bending stiffnesses, (b) bending stiffness multiplied by 0.5, and (c) 10 (P. Boisse et al., 2018).

Yarn tension, controlled by the winding or braiding machine, plays an important role in the deformation of the final production (Calius & Springer, 1990; Eduljee & Gillespie, 1996; Kugler & Moon, 2002). The appropriate yarn tension should be determined for different types of products. Lower winding tension can cause fibre paths to become unstable and slip on the mandrel, leading to wrinkles and local buckling when the preform passes through the pultrusion die. Higher tow tension can reduce wrinkle amplitude, but may result in significant dry veil and increased pulling force.

The effects of winding tow tension (Banerjee, Sun, Mantell, & Cohen, 1998; Cai, Gutowski, & Allen, 1992; Hahn, Kempner, & Lee, 1993) and braiding tow tension (Roy, Zou, & Potluri, 2016) on preform consolidation have been investigated. The tension has a similar effect on the preform thickness. The winding fibre state is shown in Figure 2.9 (Cai et al., 1992). The consolidation pressure *p* is balanced by the winding tension *T* and this can be written as

$$Tsin^2\alpha = pr \tag{2.2}$$

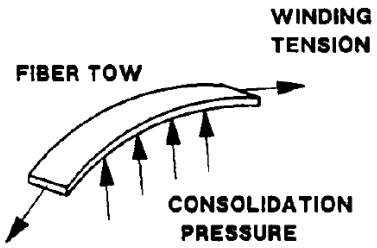

Figure 2.9. Fibre stress state after the winding(Cai et al., 1992)

Where r is the radial position vector of the wound layer, and α is the winding angle. If the braiding angle and tension remain constant, the pressure will decrease as the radius increases. It should be noticed that the yarn tension refers to the tension at the fell point, which varies with the braiding angle. A similar formula for braiding was given in Eq.2.3 (Roy et al., 2016) considering the yarn width w_y. For the multilayer, different yarn tensions and braiding angles can lead to the total thickness change. The two main factors, applied pressure and cover factor, play different roles in the preform and the final composite tube.

$$p = \frac{2Tsin^2\alpha}{w_y * R} \tag{2. 3}$$

2.3.4. Characterisation of Fibre Distribution Imperfections

The characterisation of fibre distribution imperfections (e.g., fibre wrinkle, fibre flip, fibre waviness and resin-rich zone) has been discussed previously, and its influence on the performance of FRP composites has been examined. Figure 2.10 shows typical fibre distribution imperfections and presented a taxonomy of mat misalignment by comparing the actual location to the idealised location using manually plotted points (Poulton & Sebastian, 2021).

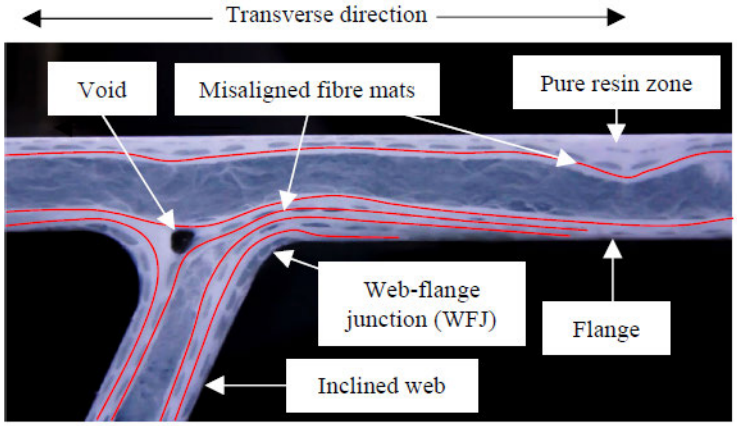

Figure 2.10. Misalignment of fibre mats within a GFRP bridge deck cross-section (Poulton & Sebastian, 2021).

Optical microscopy and scanning electron microscopy (SEM) are widely used to examine the fibre distribution, fibre orientation, and the presence of voids in composite materials. These techniques allow for detailed and direct visualization of the microstructure and can help identify any fibre distribution imperfections (Bunsell, 2009; M. Wisnom, 1999). Image processing techniques can be employed to analyse microscopy or images and quantify fibre distribution imperfections. These methods involve the use of algorithms to extract features related to fibre orientation, fibre waviness, and void content, providing quantitative data on the spatial distribution of fibres and their alignment. Netzel et al. (Netzel et al., 2021) quantified the wrinkling severity and material flow with an optical microscope. This research adopts an image analysis method to measure the UD fibre content along the cross-section, offering more details on the fibre distribution. Wilhelmsson et al. (Wilhelmsson, Gutkin, Edgren, & Asp, 2018) presented a high-resolution misalignment analysis to identify the maximum fibre misalignment to predict the compressive strength of non-crimp fabrics, while Qi et al. (Qi et al., 2023) showed the effect of fibre misalignment on stress distribution using the FE method, as shown in Figure 2.11.

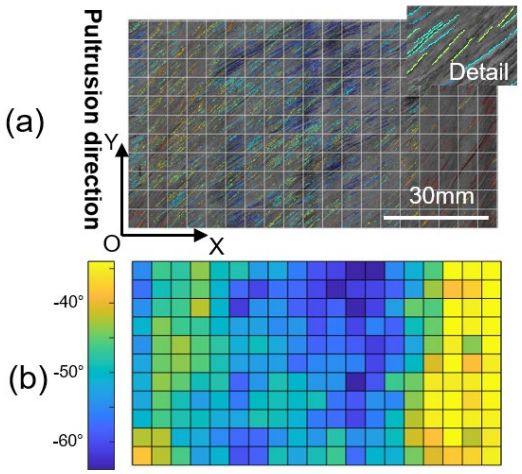

Figure 2.11. In-plane waviness measured based on image analysis: (a) detected fibres and (b) the spatial distribution of fibre misalignment (Qi et al., 2023).

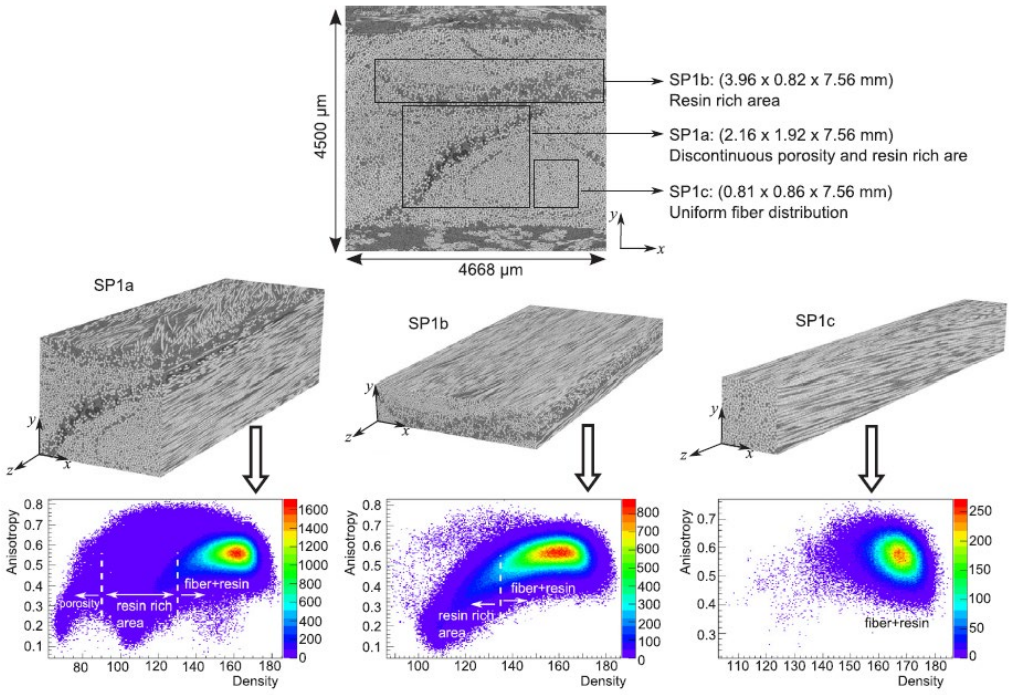

Figure 2.12. Three different volume of interests (VOIs) taken from specimen SP1, i.e. SP1a, SP1b and SP1c, together with a corresponding histogram of the degree of anisotropy versus average grey value (density) computed from the voxel model (Baran, Straumit, Shishkina, & Lomov, 2018).

X-ray CT is a non-destructive technique (NDT) that enables the visualisation and quantification of fibre distribution imperfections in three dimensions (Centea & Hubert, 2011; Emerson, Jespersen, Dahl, Conradsen, & Mikkelsen, 2017; Yousaf et al., 2018). This method

can provide valuable information on fibre orientation, fibre waviness, and void content within the composite material (Garcea, Wang, & Withers, 2018; Wright, Fu, Sinclair, & Spearing, 2008). Figure 2.12 shows the characterisation of the internal geometry of the resin-rich area (Baran et al., 2018).

Ultrasonic techniques, such as phased array ultrasonic testing (PAUT) and guided wave testing (GWT), can be used to detect and characterise fibre distribution imperfections. These methods rely on the propagation of ultrasonic waves through the composite material, with changes in wave velocity and attenuation revealing the presence of imperfections (Smith, Nelson, Mienczakowski, & Challis, 2009; Staszewski, Mahzan, & Traynor, 2009).

2.4. Impact of Fibre distribution imperfection on hollow FRP profile buckling behaviour

2.4.1. Buckling of hollow FRP profiles

These hollow FRP profiles are susceptible to buckling due to their slender nature and anisotropic material properties (Reddy, 2003). Buckling can be broadly classified into two categories: local buckling and global buckling. Local buckling refers to the collapse of individual structural elements or sections, such as the walls of a hollow FRP profile, due to compressive stresses that exceed the material's critical buckling stress (Barbero, 2010). Global buckling, on the other hand, occurs when the entire structure loses stability under compressive loading, resulting in a sudden and catastrophic failure (Ascione, Berardi, Giordano, & Spadea, 2014; De Lorenzis & La Tegola, 2005). To explore the local-to-global buckling transition, a parametric analysis with varying beam lengths was conducted (De Lorenzis & La Tegola, 2005). Three distinct collapse modes, twisting, local buckling, and lateral buckling, were observed as shown in Figure 2.13.

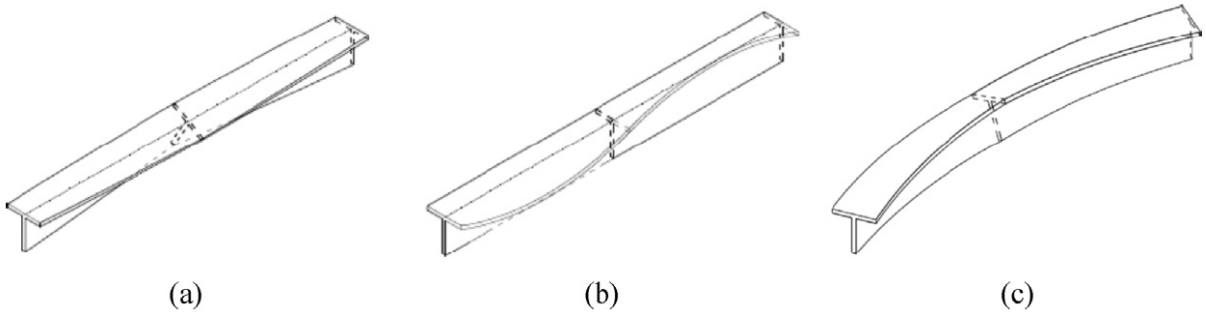

Figure 2.13. Buckling modes; (a) twisting, (b) flange local buckling and (c) lateral buckling (De Lorenzis & La Tegola, 2005).

Several theoretical models and approaches have been developed to study the buckling behaviour of hollow box FRP structures. Classical plate theory, shell theory, and beam-column theory are among the common approaches used to predict buckling behaviour (Jones, 2006). Local buckling analysis of the PFRP profile is typically performed using the plate theory (Arani, Maghamikia, Mohammadimehr, & Arefmanesh, 2011; Cardoso, Harries, & Batista, 2014a; L. Kollár & Springer, 2003; L. P. Kollár, 2003), with separate calculations for the flange and web loading capacities and considering the flexibility of the flange-web connections.

Qiao et al. (Qiao, Davalos, & Wang, 2001) presented an explicit formulation and elastic constraint coefficient to determine the local buckling capacity of a box section under compression loading. Kollár (L. P. Kollár, 2003) proposed a refined equation for the constraint coefficient at the corners. It should be noted that local buckling in PFRP profiles under compression loading differs from that under bending loading, as only the top flange and partial web buckle are under compression (Ascione et al., 2016).

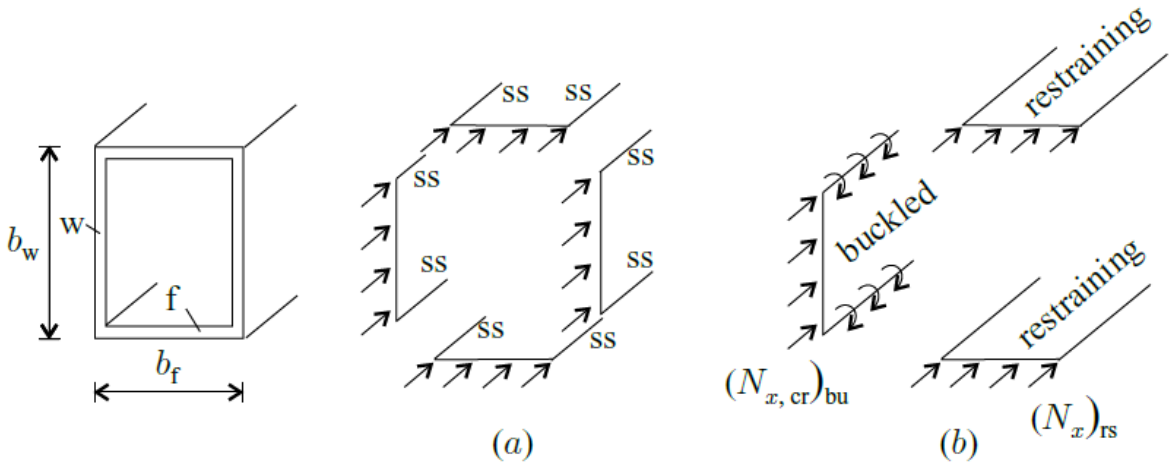

Figure 2.14. Modelling of local buckling of axially loaded member (L. P. Kollár, 2003).

Figure 2.14 shows the box section to demonstrate the flange local buckling (FLB) according to elastic plate theory. The analytic solution for critical buckling stress can be calculated by Eq. (2.4) (Kollar & Springer, 2003).

$$\sigma_{\mathrm{cr}} = \frac{\pi^2}{t_{\mathrm{f}} L_{\mathrm{y}}^2}\left[\alpha\sqrt{D_{11}D_{22}} + \beta(D_{12} + 2D_{66})\right] \tag{2.4}$$

Where D_{ij} is the plate flexural stiffness parameter; t_{f} is the wall thickness; α and β are dependent on the boundary condition of the edge, which accounts for the rotational stiffness of

the flange support. When the long edge of the plate is rotationally restrained, α and β are calculated by Eq. (2.5) and Eq. (2.6), respectively.

$$\alpha = 2\sqrt{1 + 4.139\xi} \tag{2.5}$$

$$\beta = 2 + 0.62\xi^2 \tag{2.6}$$

Then,

$$\sigma_{\text{cr}} = \frac{\pi^2}{t_f L_y^2}\left[2\sqrt{1 + 4.139\xi}\sqrt{D_{11}D_{22}} + (2 + 0.62\xi^2)(D_{12} + 2D_{66})\right] \tag{2.7}$$

ξ is a parameter that reflects the restrain of the unloaded edge. When $\xi = 0$, the unloaded edge is seen as simply supported. When $\xi = 1$, the unloaded edge is fully clamped.

2.4.2. Impact of Fibre Distribution Imperfections on Buckling Behaviour

Fibre distribution imperfections, such as NUFD, fibre waviness, and misalignment, can significantly impact the buckling behaviour of hollow FRP profiles (Feo, Mosallam, & Penna, 2013; T. Liu, Yang, Feng, & Harries, 2020). These imperfections can lead to stress concentrations, reduced stiffness, and altered load distribution within the structure, which can affect the critical buckling load, mode shapes, and overall structural performance (Haselbach, Bitsche, & Branner, 2016; Li et al., 2016; Raouf, 1996). Figure 2.15 demonstrates that web-flange junction failures result in delamination along misaligned mat layers and kinking at the steepest tangent angles, accompanied by transverse cracks occasionally reaching the surface. Surface cracks facilitate water ingress, potentially weakening fibre-to-resin bonds. In conclusion, such failures can compromise the composite's structural integrity and durability due to the combined effects of delamination, kinking, and water-induced bond deterioration (Journoud, Bouvet, Castanié, & Ratsifandrihana, 2022; Poulton & Sebastian, 2021).

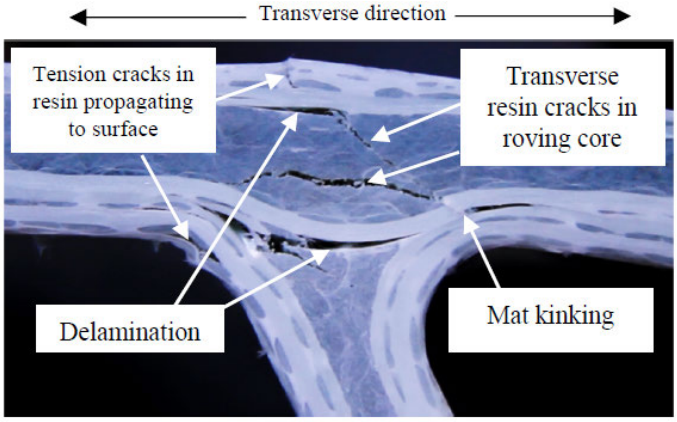

Figure 2.15. Influence of fibre distribution imperfection on failure of web-flange junction (Poulton & Sebastian, 2021).

The effect of fibre distribution imperfections on buckling behaviour has been studied using theoretical models, experimental investigations, and numerical simulations. These studies have demonstrated that fibre distribution imperfections can lead to a reduction in the critical buckling load and an increase in the likelihood of local buckling (Saenz-Castillo, Martín, Calvo, Rodriguez-Lence, & Güemes, 2019). In addition, the presence of imperfections can result in the initiation of damage and failure at lower load levels compared to structures with uniform fibre distribution (Croft et al., 2011; M. R. Wisnom, Gigliotti, Ersoy, Campbell, & Potter, 2006). The impact of non-uniform fibre distribution on buckling behaviour arises from the inhomogeneous distribution of fibres within the composite material. This non-uniformity can result in localised regions of reduced stiffness and strength, causing the structure to buckle at a lower load than anticipated (Asadi, Eynbeygi, & Wang, 2014).

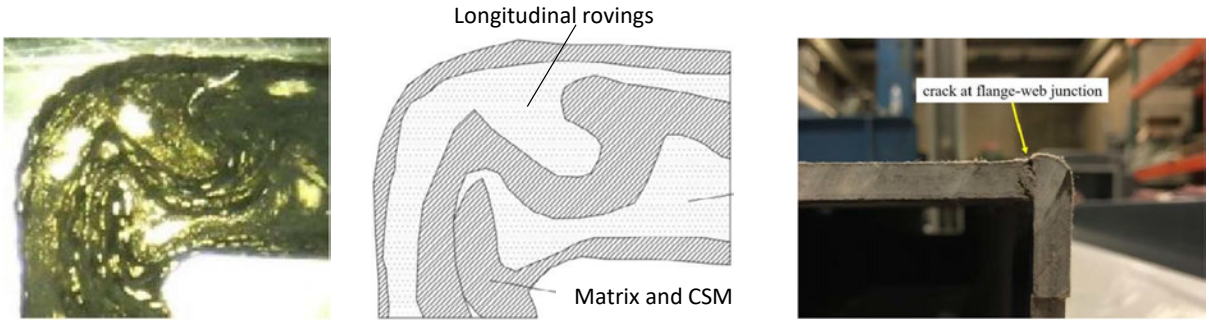

Figure 2.16. Fibre and matrix architecture at flange-web junction of a specimen; (a) image of fibre and matrix architecture, (b) schematic of fibre and matrix architecture and (c) crack at the flange-web junction (T. Liu & Harries, 2018).

The contribution of the rotational stiffness was investigated at the flange-web junction to flange local buckling under bending (T. Liu & Harries, 2018). They found that the fibre-matrix architecture, shown in Fig 2.16 (a) and (b), would affect the stiffness of flange edge support. Results showed that a weak junction could lead to premature failure of the entire profile, as shown in Figure 2.16(c).

Fibre waviness can also adversely affect the buckling behaviour of hollow FRP profiles. Wavy fibres are not aligned in the intended load-carrying direction, leading to reduced axial stiffness and increased susceptibility to buckling. Fibre waviness can also result in the formation of kink bands, which are localised regions of high shear deformation, further reducing the critical buckling load (Elhajjar & Shams, 2014; Pagani & Sanchez-Majano, 2022).

Wu (Wu et al., 2018) studied unidirectional carbon fibre laminates with in-plane and out-of-plane waviness, as illustrated in Figure 2.17. Waviness severity is characterised by the waviness ratio. Results reveal a significant impact on compressive strength, particularly for larger waviness ratios. A 33.0% strength reduction occurs with out-of-plane wrinkling at a 0.037 waviness ratio, while a 25.4% reduction is observed for in-plane buckling at a 0.038 waviness ratio. Reviews on fibre waviness formation and its effect on mechanical performance are reported by (Alves et al., 2021; Kulkarni et al., 2020).

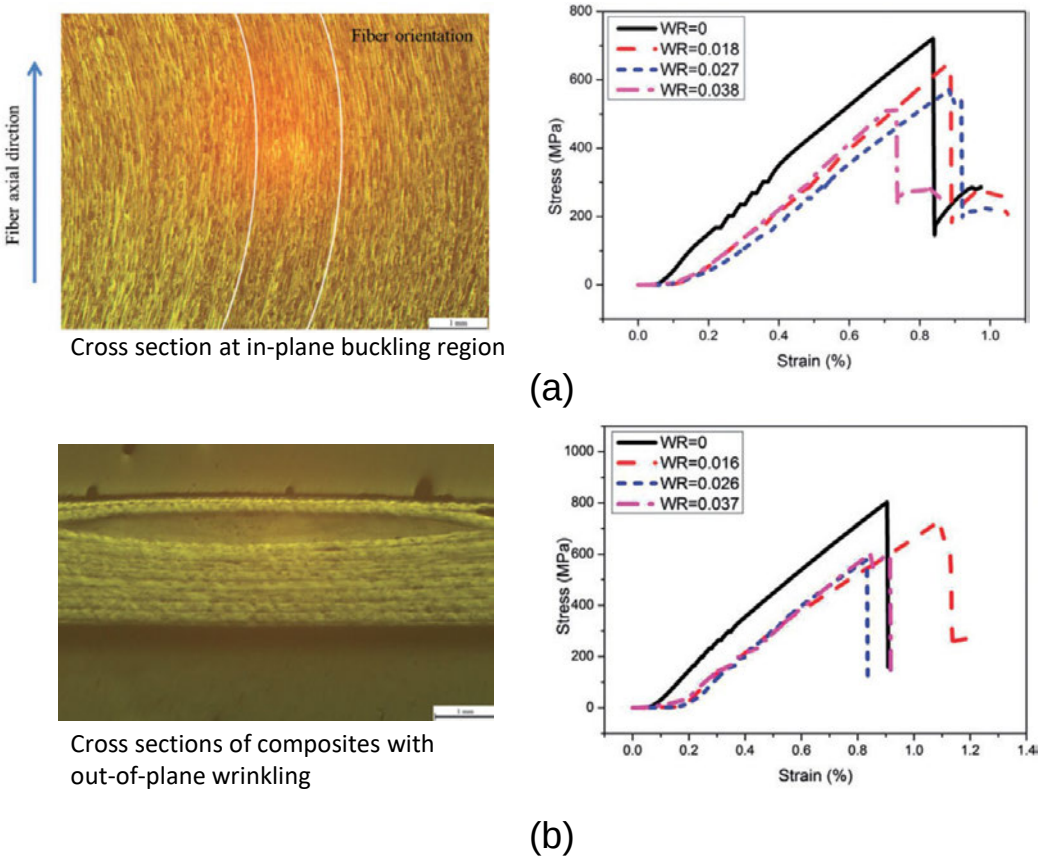

Figure 2.17. Compressive properties of unidirectional laminates at different waviness ratios; (a) containing in-plane buckling, and (b) containing out-of-plane wrinkling (Wu et al., 2018).

2.4.3. Numerical simulations of imperfection and its effect on mechanical performance

Numerical simulations, such as finite element analysis (FEA), have been extensively used to study the buckling behaviour of hollow box FRP structures and the impact of fibre distribution imperfections (Mukhopadhyay et al., 2015; Sjölander et al., 2016). FEA allows for the modelling of complex geometries, boundary conditions, and material properties, providing a versatile tool for analysing buckling behaviour (Hörrmann, Adumitroaie, Viechtbauer, & Schagerl, 2016). Various techniques have been proposed to model fibre distribution

imperfections, including probabilistic approaches and micromechanical models (Naouar et al., 2014; Sutcliffe, 2013).

Defect formation simulation has been extensively researched (El Said, Green, & Hallett, 2014; Isart et al., 2015; Naouar, Vidal-Salle, Schneider, Maire, & Boisse, 2015; A. J. Thompson, El Said, Belnoue, & Hallett, 2018). Belnoue et al. (Jonathan P. H. Belnoue & Hallett, 2020) introduced a modelling approach to predict wrinkles in laminate composite manufacturing, based on the kinematically constitutive law. Enhanced computational efficiency enables larger-scale model application. The compaction process for thick laminated composites employs mutually constrained shell and membrane elements, reflecting ply interaction through-thickness behaviour via compliant penalty contact (Adam J. Thompson, McFarlane, et al., 2020), as shown in Figure 2.18. This model investigates key manufacturing parameters to mitigate fibre path defects. Ei Said et al. (El Said et al., 2014) suggested a multi-scale approach for simulating deformations and defects in larger-scale models. The yarn was modelled using 2D elements, with material properties derived through iteration and meso-scale comparisons. The model was then converted into a macro-scale fabric model via tessellation. This approach significantly reduced computational time compared to traditional methods like 3D and beam elements.

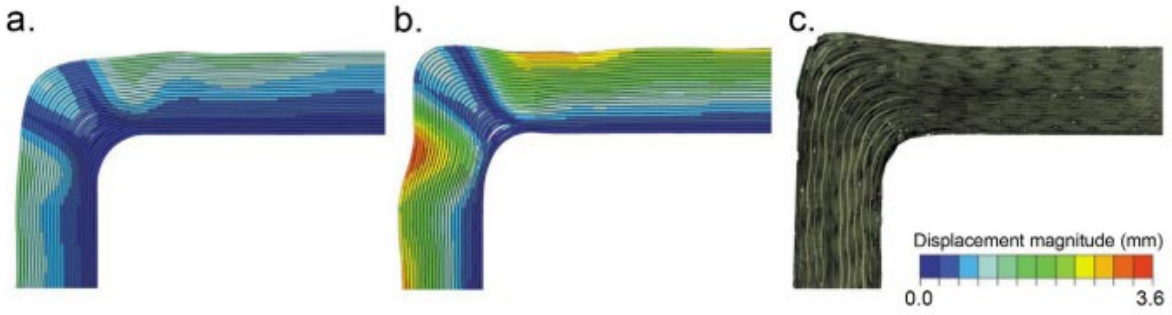

Figure 2.18. Detail of wrinkle in radius (a) simulation with perfect contact between plies (b) simulation with 12.5% extra bulk included in the lay-up (c) experiment (Adam J. Thompson, McFarlane, et al., 2020).

Based on the FEA with the defects input, many studies evaluate the effect of the defect on the mechanical performance. Zhang et al. (Zhang, Zhang, Xu, & Chen, 2019) found that non-uniform fibre packing over a cross-section has a limited effect on compressive strength based on the FE model. However, their study did not consider the individual lamina in the preform and specific locations of defects in full-scale profiles. Feng. et al. (Feng et al., 2021) reported NUFD significantly impacts the global buckling of PFRP profiles. For I-sections with

a slenderness ratio of 70, NUFD resulted in a reduction factor of 0.88. Figure 2.19(a) shows a linear elastic analysis of the laminate FEM, incorporating experimentally measured fibre waviness. Strain fields from both Digital Image Correlation (DIC) experiments and FE analysis reveal inhomogeneity in the waviness region, as shown in Fi.g 2.19(b). Additionally, waviness can significantly affect stress distribution (Sitohang, Grouve, Warnet, & Akkerman, 2021).

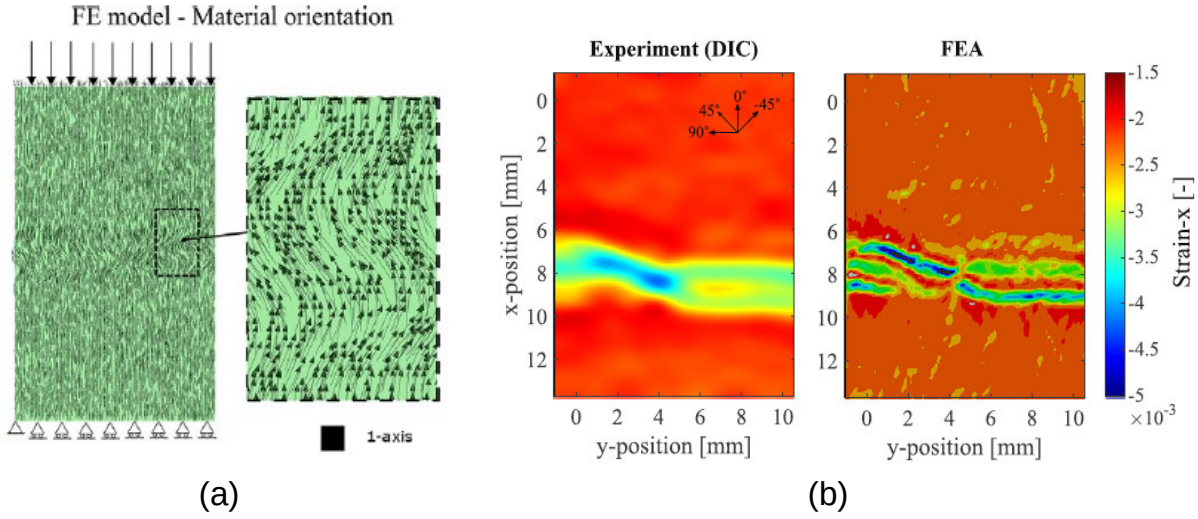

Figure 2.19. (a) a linear elastic analysis of the laminate modelled with fibre waviness, and (b) strain fields from DIC measurements and FEA (Sitohang et al., 2021).

2.5. Conclusions and future research directions

This review highlights the importance of understanding the formation of fibre distribution imperfections and their effect on the buckling behaviour of hollow box FRP structures. The interplay between manufacturing techniques, material properties, and defects such as fibre waviness, misalignment, and volume fraction variations can significantly affect the structural performance of these composite structures. Theoretical models, experimental investigations, and numerical simulations have contributed to a better understanding of buckling behaviour and the influence of fibre distribution imperfections. Nonetheless, additional research is necessary to directly comprehend the defect impact on buckling behaviour, with several areas requiring further investigation:

- Process optimisation: Investigating the factors that contribute to non-uniform fibre distribution during the pull-winding and pull-braiding process and its impact on the axial compressive properties of hollow profiles will help in optimising manufacturing processes and improving the performance of composite structures.

- Advancement of theoretical models: Existing models predicting local buckling force rely on uniform fibre distribution, overlooking defect effects. Defects can reduce maximum load and complicate accurate predictions. More precise and robust theoretical models are needed to effectively capture the complex interplay between fibre distribution imperfections, material properties, and buckling behaviour.
- Improved numerical techniques: Numerical methods predominantly emphasize unit cell compaction models, accounting for yarn compaction and interactions. However, these models don’t capture defects like wrinkles and waviness. To analyse local buckling behaviour in pultruded profiles, a full-scale numerical model with efficient computation time is needed.

CHAPTER 3: PAPER 1 – FIBRE WAVINESS CHARACTERISATION AND MODELLING BY FILTERED CANNY MISALIGNMENT ANALYSIS (FCMA)

3.1. Introduction

In Chapter 3, the Filtered Canny Misalignment Analysis (FCMA) method is introduced as a novel approach for quantifying in-plane and out-of-plane fibre waviness. The FCMA method demonstrates superior accuracy and computational efficiency compared to the existing method, such as high resolution misalignment analysis (HRMA). The results obtained using the FCMA method are used to develop a finite element model (FEM) to simulate the effects of fibre waviness on stress distribution in hollow composite columns under axial compression. Based on the FEM approaches, the more significant the fibre misalignment, the more pronounced the stress concentration. This is because the fibre orientation caused the change in local stiffness, which further affects the stress distribution.

3.2. Links and implications

The FCMA method can be combined with the analysis of Non-Uniform Fibre Distribution (NUFD) discussed in the following chapters of the thesis to provide a comprehensive understanding of the impact of manufacturing-induced defects on the mechanical properties and structural behaviour of hollow box FRP structures. The insights gained from the FCMA method regarding fibre waviness can be further applied to investigate its effects on axial compression and bending performance, contributing to a deeper understanding of the relationship between fibre waviness and other factors that influence the performance of hollow box FRP structures. Furthermore, the FCMA method's outputs, such as in-plane and out-of-plane fibre waviness, can be incorporated into the finite element models developed in this thesis, improving the accuracy of predictions for stress distribution and structural performance under various loading conditions.

3.3. Published paper

Composite Structures 307 (2023) 116666

Contents lists available at ScienceDirect

Composite Structures

journal homepage: www.elsevier.com/locate/compstruct

Fibre waviness characterisation and modelling by Filtered Canny Misalignment Analysis (FCMA)

Songming Qi [a], Omar Alajarmeh [a], Tristan Shelley [a], Peter Schubel [a], Kendric Rendle-Short [b], Xuesen Zeng [a,*]

[a] University of Southern Queensland, Centre for Future Materials, Toowoomba, Queensland 4350, Australia
[b] Wagners Composite Fibre Technologies, Wellcamp, Queensland 4350, Australia

ARTICLE INFO

Keywords:
A. Fibres
B. Defects
D. Optical microscopy
E. Pultrusion
Fibre orientation

ABSTRACT

Accurate and cost-effective full-scale measurement of fibre waviness and misalignment in continuous fibre-reinforced composite structures remains a challenge. This study proposes a novel approach of Filtered Canny Misalignment Analysis (FCMA) to capture and quantify in-plane and out-of-plane fibre waviness. The FCMA method measures fibre misalignment from the microscope and Charge Couple Device scan images by a Canny edge detector and a Canny edge filter to effectively identify the true fibre path. The method is systematically evaluated and benchmarked with the existing High Resolution Misalignment Analysis (HRMA) method. The results show that the FCMA method is more robust, efficient, and precise for fibre waviness measurements. The fibre misalignment in selected hollow composite columns is quantified by the FCMA method. The in-plane waviness distribution is used as a material orientation input to a verified finite element model. This simulation demonstrates the effect of fibre waviness on stress distribution for a hollow composite column under axial compression. The FCMA method code is supplied as supplementary material to this paper.

1. Introduction

Composite materials made of Fibre-Reinforced Polymer (FRP) have been more popular in the aerospace, defence, infrastructure, and marine industries during the last few decades [1–5]. The performance of these materials is highly sensitive to defects, such as voids, cracking and delamination [6]. This paper will focus on characterising fibre waviness and misalignment, aiming to assess the effect of manufacturing defects. The formation of fibre waviness and its effects on mechanical performance has already been thoroughly reviewed [7–9].

The fibre misalignment, usually evaluated in a sinusoidal or Gaussian function [10,11], is a problem of great interest being responsible for the strength of the profile along the fibre direction. The maximum misalignment angle is a crucial parameter to define waviness. For instance, from an industrial perspective, the permissible misalignment of unidirectional fibres is no more than 5° [12,13]. In the actual manufacturing process, fibre waviness is always complex, where some of the fibres are randomly distributed. Statistical knowledge is always used to characterise fibre waviness, such as a standard deviation [14]. Different characterisation techniques have been explored previously based on microscopic, ultrasonic and micro-CT to get an accurate fibre angle [15–17].

Nguyen et al. [18] have estimated the typical fibre orientation precision level in carbon fibre-reinforced laminates manufactured in the autoclave and vacuum-assisted resin transfer moulding. The measurement methodology of in and out-of-plane fibre misalignment is based on micro-CT images. The application of Digital Image Correlation (DIC) to micro-CT slices for measuring fibre orientation has been investigated in continuous fibre [19,20] and short fibre [21]. Krumenacker et al. [22] provided two automated techniques for characterising fibre waviness in vacuum-bagged corner laminate, based on micro-CT and optical microscopy, respectively. Although X-ray computed tomography has been widely used to characterise fibre waviness, there are still some limitations due to material volumes, time, cost and accessibility for quick industry assessment.

The accuracy of the measured fibre angle is heavily dependent on the algorithm used to identify the fibres. Creighton et al. [23] used the Multiple Field Image Analysis (MFIA) method to analyse fibre misalignment in low-resolution micrographs. This method has been expanded to X-ray images and shows agreement with polished images

* Corresponding author.
E-mail address: xuesen.zeng@usq.edu.au (X. Zeng).

https://doi.org/10.1016/j.compstruct.2023.116666
Received 14 July 2022; Received in revised form 29 November 2022; Accepted 2 January 2023
Available online 5 January 2023

[24]. Kratmann et al. [25] presented an analysis procedure named Fourier Transform Misalignment Analysis (FTMA) in unidirectional fibre composites. Wilhelmsson et al. [26] proposed a High Resolution Misalignment Analysis (HRMA) method to measure misalignment angles by tracing individual fibres. A comparison was made with both MFIA and FTMA based on the software-generated images which had known statistics. The results show that the HRMA method outperformed both of these current methods to reduce computational time and obtain accurate measurements on composites with significant fibre waviness.

In a novel technique, the Image Processing Toolbox of MATLAB is used to inspect the braiding angle of a carbon flat braid [27]. The 'Canny' method is used to find edges, and the 'Hough' transformation is applied to detect straight lines among the edges [28,29]. The Canny method is a technique that can detect strong and weak edges by adjusting the threshold [30,31]. However, the fibre path detected by the Canny method cannot be directly used to calculate the fibre angle due to the misidentification of fibres. Additional algorithms need to be added as a filter to find the satisfied edges representing the fibre orientation.

The benefit of measuring fibre misalignment is that mechanical strength and quality control can be quickly estimated. Furthermore, it can give the Finite Element (FE) model a more precise input. An efficient algorithm is a significant advancement in the process monitoring for Automated Fibre Placement (AFP) to identify deviation of fibre location, fibre angle and gap size [32]. Wilhelmsson et al. [33] accurately predict the compressive strength of non-crimp fabrics using the maximum fibre misalignment identified by the HRMA method. Sitohang et al. [34] explore shear stress distribution so as to map the experimentally measured fibre angles to each element of the wavy ply. In addition, an engineering model was proposed to predict the compressive strength of unidirectional long fibre composites for random distribution of fibre waviness [35].

This study proposes a novel image analysis method described as the Filtered Canny Misalignment Analysis (FCMA) to characterise and quantify fibre waviness. This was examined and validated using pultruded hollow-box FRP profiles as a case study. Two approaches are employed to create the images. Optical microscopy is used for out-of-plane waviness, while a Charge-Coupled Device (CCD) flatbed scanner is used for in-plane waviness. Combining these two solutions can characterise large-scale samples with higher computational efficiency and precision.

The FCMA method uses a grid-based statistical analysis of the local fibre orientation with higher robustness to reflect the actual fibre waviness. Moreover, the image analysis result was used as input to Finite Element (FE) modelling to quantify the effect of fibre waviness on the compressive strength of the full-scale columns.

2. Materials and specimen preparation

2.1. Selected specimens

The hollow-box FRP profiles investigated in this research were manufactured by Wagners CFT using the pull-winding technique. These profiles were made from unidirectional and off-axis E-glass fibre layers impregnated via an injection die using vinyl ester polymer resin [36–38]. Table 1 lists the characteristics of the experiment samples. During the pull-winding manufacturing process, the compaction through the thickness direction generates the out-of-plane waviness of unidirectional fibre and in-plane waviness of the wound fibre [39–43]. These defects will be quantified by optical microscopy for out-of-plane waviness and the CCD flatbed scanner for in-plane waviness, respectively, as shown in Fig. 1.

Table 1
Composite layup properties of the hollow pultruded FRP profiles.

Dimensions (mm × mm)	Wall thickness (mm)	No. of plies	Fibre orientation (°)	Fibre content (%)
125 × 125	6.4	9	[0/+50/0/-50/0/-50/0/+50/0]	0°: 78.1 50°: 21.9

2.2. Specimen preparation for out-of-plane waviness

Optical microscopy was used to trace the unidirectional fibre along the pultrusion direction in polished samples. Struers LaboPol equipment was used to grind and polish the samples. For grinding, 1200 and 320 grit papers were used. DiaPro for 9 μm on the MD-largo plate, DiaPro for 3 μm on MD-DAC cloth, and OP-U Nondry on Neoprene cloth were used for polishing. Leica DMS300 was used to capture the digital image with a pixel resolution of 6 μm/pixel. ImageJ software is used to stitch the images using the plugin of ImageJ stitching. The overlapped area used linear interpolation.

2.3. Specimen preparation for in-pane waviness

A CCD scanner was used to scan the off-axis layer for a large-scale assessment of the in-plane waviness of the wound fibre. The CCD is the most common high-performance imaging detector used in many applications where high-quality image data are required [44]. This study selected a Canon LIDE 400 colour CCD scanner with a high resolution 1600 × 1600 Dot Per Inch (DPI) to perform the scanning. The samples with an area of approximately 100 cm^2 were scanned layer by layer. This method can be more feasible to assess the defects instead of X-ray CT, especially for larger samples.

Samples for scanning were conducted by partially burning out a hollow composite profile. Most of the resin evaporated by controlling the furnace temperature and burning time, leaving a small residual resin for fixing the fibre shape. In this research, the furnace temperature was maintained at 600°C for 15 min to obtain the required partial burn-out sample. Masking tape was used to maintain the relative position of the tows by fixing their edges when the samples were peeled out layer by layer. As a result, each off-axis layer could be scanned. The example image of fibre misalignment is shown in Fig. 2a.

3. Methodology and parametric assessment

This section describes the Filtered Canny Misalignment Analysis (FCMA) method and the influencing factors on the accuracy of measurements.

3.1. FCMA procedures

The proposed image analysis methodology follows five steps, which were implemented in MATLAB 2019b. The input parameters for the application are provided in Table 2, while Fig. 2 illustrates the process of

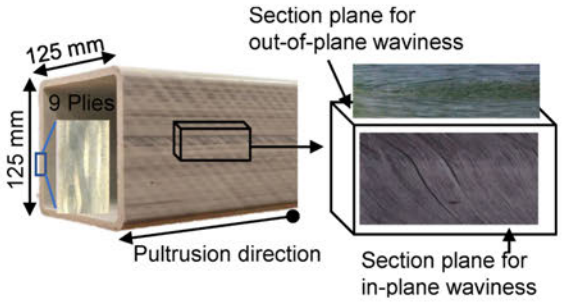

Fig. 1. In-plane and out-of-plane waviness defects in pultruded composite profile.

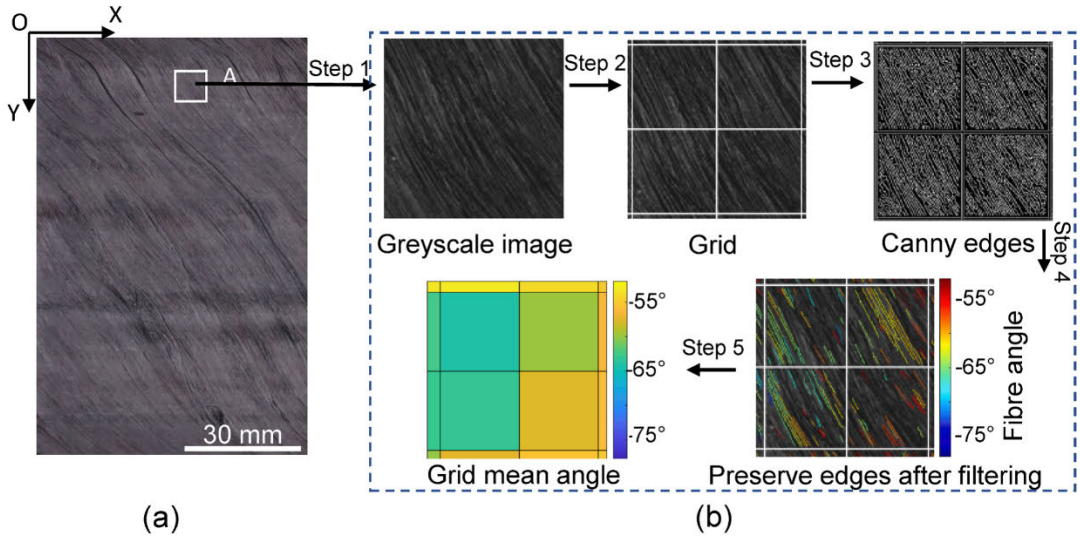

Fig. 2. (a) Scanned image of in-plane glass fibre layer after partial burn-out; (b) the proposed procedures of FCMA method.

Table 2
Parameters used in the Matlab script for the different FCMA analyses.

Parameter	Value		
	Artificial image	Scanned image	Micrograph
Background	1 (Black)	0 (White)	1
Edge_diam (Pixel)	7	9	3
Cell_Size (Pixel)	30–200	100	64
α	1.1	1.2	1.1
β	0.5	0.35	0.5

the FCMA method. The key output of this method is grid-based statistical fibre angles. The statistical results and parameters of the sample, such as misalignment and standard deviation, can be calculated based on the grid mean angle.

(1) Greyscale conversion: The scanned image is a true colour image. When imported into MATLAB, the image consists of an m-by-n-by-3 numeric array. The image is converted to the greyscale for edge recognition, and each pixel is stored into one single number in the m-by-n array. The origin of the coordinate is set in the upper left of the image, as shown in Fig. 2(a). The array can be transformed into a Cartesian coordinate system according to the resolution of the scanned image.
(2) Gridding: A grid is added to the image, which divides the original image into smaller pieces. The grid lines are realised by changing the greyscale value of the corresponding position of the image. The gridlines in the image have two purposes. Firstly, the grids cut the fibres into small pieces to calculate the local fibre angle. Secondly, the gridlines are used to analyse the statistical distribution based on the grid unit.
(3) Fibre path identification: MATLAB has several built-in methods to detect the edge. The Canny edge detector is a method to detect edges according to the gradient using the derivative of a Gaussian filter. A double threshold is applied to determine the potential edges by calculating gradient magnitude: a high threshold for low edge sensitivity and a low threshold for high edge sensitivity, making the Canny method more likely to detect true weak edges than other methods. In MATLAB, the return value of the Canny method is a binary image in the form of a logical array. Taking a grid unit as an example in Fig. 3(a), the detected edges include the individual fibres, interconnected fibres and resin-rich space. The number of detected edges can be adjusted by the sensitivity threshold of the built-in function.
(4) Fibre path filter: Most of the edges detected by the Canny method are not from individual fibres and cannot be used directly to calculate the fibre angle. The issue is mainly due to the interconnection between adjacent fibres and short edges (dots). A Canny edge filter is applied to the detected edges to preserve the valid edges representing the true fibre path. Fig. 3(b) shows examples of the Canny edge filter. The accepted and unaccepted edges depend on the minor and major axis lengths of ellipses that envelop the Canny edges. The Canny edge filter is described as.

$$Filter: \begin{cases} L_{minor} \le \alpha \times D_{fibre} (1 < \alpha < 2) \\ L_{major} \ge \beta \times L_{grid} (0.3 < \beta < 0.6) \end{cases} \quad (1)$$

Where L_{minor} and L_{major} are the length of the minor and major axis in pixels of a Canny edge ellipse. The coefficients α and β are the thresholds of the acceptable Canny edges that can represent the real individual fibre path. Limiting the minor axis length (L_{minor}) will eliminate the interconnection edges, while increasing the major axis length (L_{major}) will delete the dot and short edge.

The ellipse that envelopes a Canny edge has the same normalised second central moments as the region of the detected edges. The central moment is the expected value of a specified integer power of the deviation of the random variable from the mean [45]. The property of the ellipse can be obtained by the built-in function 'regionprops' in MATLAB. Moreover, the ellipse can also return the orientation measurement between the global x-axis and the local major axis, which corresponds to the orientation of the fibre.

Fig. 4(a) shows the trend of individual fibre identification in one gird as the coefficient α increases while the β value is fixed. The detected edge is perfectly straight when the coefficient α is close to 1. When α is larger than 1.8, the interconnected edges will be introduced, marked with red circles. On the other hand, the coefficient β governs the elimination of spots and short edges in proportion to the size of the grid. Fig. 4(b) shows that the higher β value will narrow the scatter of the calculated fibre angle within the grid. The unaccepted short edges are marked with the red circle in Fig. 4(b). The value of the coefficient β is determined within the range between 0.3 and 0.6, based on the extensive image

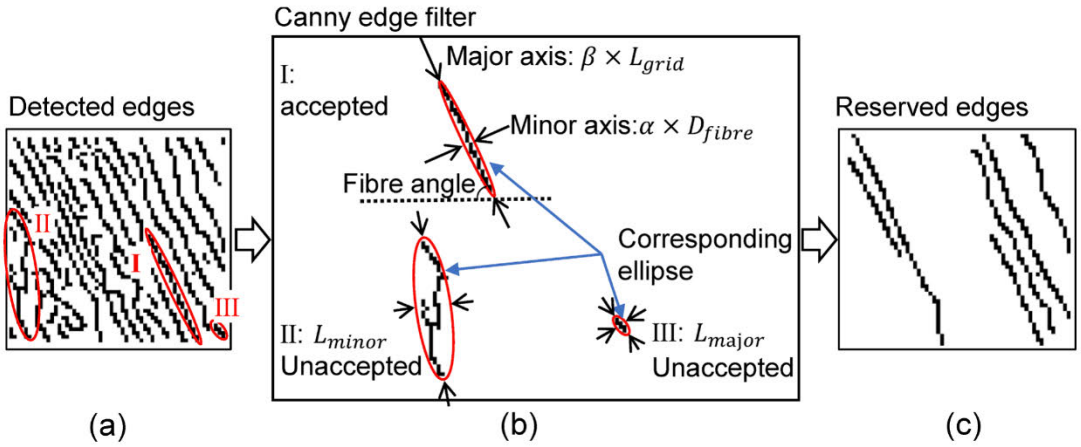

Fig. 3. Canny edges filter by the corresponding ellipse: (a) detected edges by the Canny method, (b) accepted and unaccepted examples of the proposed Canny edge filter, and (c) preserved edges.

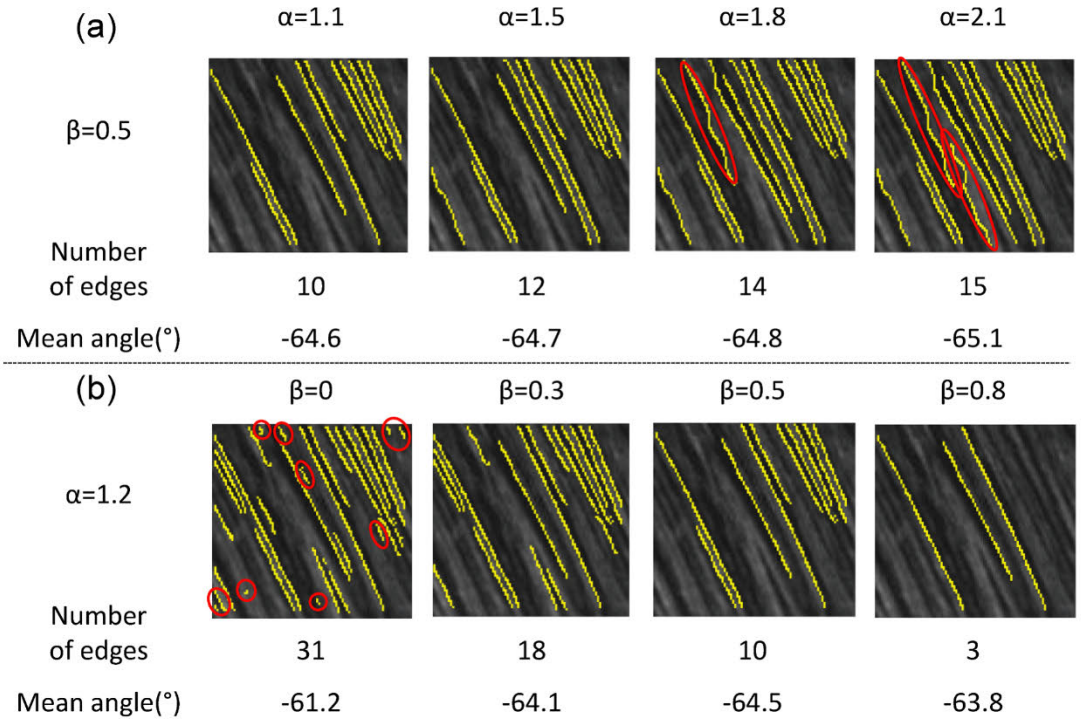

Fig. 4. Canny edge filter coefficient sensitivity: (a) the effects of α and (b) the effects of β.

analysis. The coefficient depends on the image quality and the size of the grid. After the Canny edge filter applies, the retained edges can be used to determine the local fibre orientations, as shown in Fig. 3(c). In most cases, assigning α to 1.2 and β to 0.5 is sufficient to achieve converged measurements.

(5) Grid mean: The single grid angle $\overline{\theta}_i$ is defined by the mean value of M number of detected fibres within the grid unit as.

$$\overline{\theta}_i = \frac{1}{M}\sum_{j=1}^{M}\theta_j \tag{2}$$

The centre of the grid will represent the spatial position with the mean angle in the following analysis. Furthermore, the N number of grid plots reflects the spatial distribution. The fibre misalignment $\overline{\theta}$ and the standard deviation σ for the statistics of the image are based on the single grid mean angle, as.

$$\overline{\theta} = \frac{1}{N}\sum_{i=1}^{N}|\overline{\theta}_i| \tag{3}$$

$$\sigma = \sqrt{\frac{1}{N}\sum_{i=1}^{N}\left|\overline{\theta}_i - \frac{1}{N}\sum_{i=1}^{N}\overline{\theta}_i\right|^2} \tag{4}$$

3.2. Accuracy assessment of Filtered Canny misalignment analysis

The proposed FCMA method was compared with the existing HRMA method by using computer-generated images with known statistics, as shown in Fig. 5(a). The known statistics, including the mean orientation and the standard deviation of the fibre segments, are defined as the true statistic value. The accuracy of the two methods was evaluated by [26].

$$Error(\%) = 100 \times |(Truestat.value - Measuredvalue)/Truestat.value| \tag{5}$$

Two types of computer-generated images were used in this study to assess the accuracy of the FCMA method. The first set of images has different mean orientations with zero standard deviation, representing fibre angle change with no fibre waviness. The second set of images has different standard deviations with zero mean orientation, representing varying fibre waviness. The former is intended to examine the ability of the algorithm to identify fibre orientation, while the latter is to check the ability to capture fibre waviness.

Fig. 5(b) shows the effect of the grid size on the accuracy. The standard deviation of 2.5° associated with moderate fibre waviness is more sensitive to the grid size than the fibre orientation of 10° without fibre waviness. In general, a smaller grid size can reduce the error for the standard deviation of 2.5°. Reducing the grid size can increase the spatial resolution to improve the accuracy of the results. However, a tiny grid size should be avoided as it will introduce edge detection errors, especially when using the HRMA method. The results show that a 50 μm grid size is sufficient to characterise the real continuous fibre laminates [26].

The comparison between the proposed FCMA method and the existing HRMA method is shown in Fig. 5(c) for varying mean orientation without fibre waviness. Both methods are based on the grid size of 30 μm and 50 μm (a pixel resolution of 1.0 μm/pixel), according to Fig. 5 (b). The HRMA method can measure fibre misalignment up to 45° with an error between 2% and 6%. Reducing the grid size can improve precision. In contrast, there is no limitation to the individual fibre angle for the FCMA method, and the error can be achieved below 1%.

Fig. 5(d) shows the comparison of varying standard deviations with zero mean orientation. It found that changing the grid size from 50 to 30 μm significantly improves the accuracy of the waviness measurements for both methods. The HRMA method performs well for the standard deviation above 2°. However, the error increased to approximately 20% for the standard deviation below 2°. The current FCMA method shows consistently better performance over the entire standard deviations. The errors are below 6% when the gird size is 30 μm. The robustness and accuracy of the FCMA method will enable the application to characterise

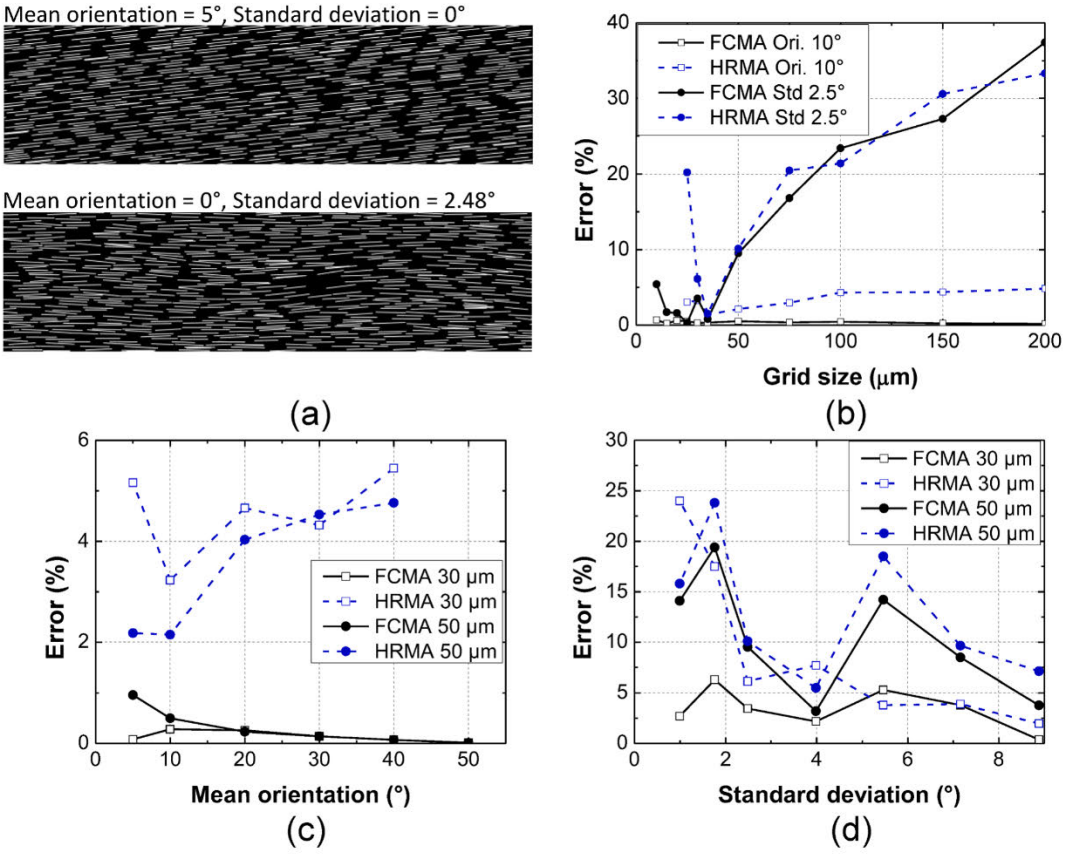

Fig. 5. Error comparison between the proposed FCMA and the existing HRMA in literature: (a) software-generated images with known mean orientation and standard deviation, (b) the effects of grid size on analysis accuracy, (c) analysis accuracy of mean orientation, and (d) analysis accuracy of standard deviation.

severe fibre waviness.

Compared with the HRMA methods, the proposed FCMA method has better stability to minimise the error percentage. Fig. 6 shows the different strategies for calculating fibre path angles with the identified sources of error. For the HRMA method, the regression line (red line in Fig. 6(a)) for calculating the angle of the fibre has a rotation, which is more evident for the connected edges. The FCMA method calculates the fibre angle by the envelope of the edge with less error than HRMA. Fig. 6 (b) shows that the HRMA method identifies the edge in each grid, generating different fibre angles for the same straight edge. The FCMA continuous mode identifies the edge as a whole within the grid.

3.3. Effects of grid size on fibre angle detection

For fibre waviness following a sinusoidal wave, the statistical measurement of the maximum misalignment angle (θ_{max}) is sensitive to the grid size. Fig. 7(a) shows one wavelength of fibre waviness assumed to be planar sinusoidal [10], where the wavelength is divided by ten grids. Fig. 7(b) shows the influence of different grid sizes on the mean angle of the grid in one wavelength. The smaller the grid, the more accurate the measured angle of the waviness.

The FCMA method calculates the angle of the fibre segment as a straight line from the start point to the endpoint, ignoring the path of the curve. For an extreme case, if only one grid is used in one wavelength, the grid angle calculated by the FCMA method is approximately zero, which means a straight line instead of the detected curve line. A larger grid size means the number of sampling points will decrease, as shown in Fig. 7(c). This sinusoidal curve with different amplitudes investigates the required grids in a wavelength to get the maximum misalignment. The error percentage is shown in Fig. 7(d). When the number of grids is selected to be five per wavelength, the error percentage of θ_{max} is practically controlled below 8%. This means that the wavelength of the waviness that the FCMA can measure is five times the grid size.

3.4. Effects of image resolution

The scanned images by a CCD document scanner make the FCMA method useful. Nevertheless, the image DPI affects the number and quality of the detected fibres. Localised details, shown in Fig. 8(a), illustrate the effect of the image resolution from 100 to 1200 DPI based on a grid size of 6.3 mm. The line width of grid division is determined by pixel in the script, resulting in the width of grid lines changing with image resolutions. The result shows that the FCMA method identifies more valid fibre segments with increasing resolution.

Table 3 shows the image analysis results of Fig. 8(a) at different image DPI. No fibres can be detected at the 100 DPI resolution. Canny edges can be found starting at 200 DPI. However, only a small number of fibres are retained after filtering, approximately 0.7 edges per grid unit. Above 600 DPI, the statistics of the image, such as θ_{max} and σ, start to converge. It can be observed that the difference in the maximum misalignment angle between 600 and 1200 DPI is no more than 0.4°.

Moreover, Fig. 8(b) shows that the mean angle of detected fibres at 600 DPI is highly correlated with the angle at 1200 DPI (0.95) along the pultrusion direction. The difference between 600 DPI and 1200 DPI is insignificant, meaning 600 DPI is sufficient to characterise the fibre waviness. This value of DPI suits the investigated image in this study, whereas it might be required to increase the DPI on other scanned images.

The computational time of the FCMA method is influenced by grid size and image resolution, as shown in Fig. 9. Images which were 70 mm

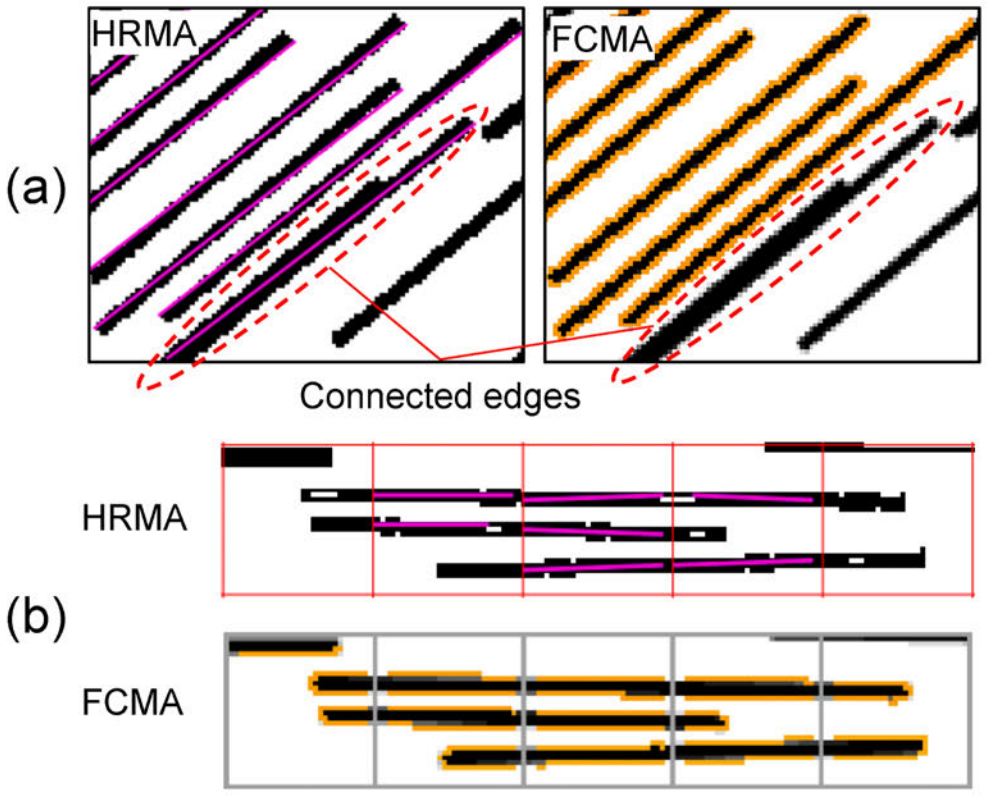

Fig. 6. Different strategies between HRMA and FCMA for (a) calculating edge angles and (b) identifying edges.

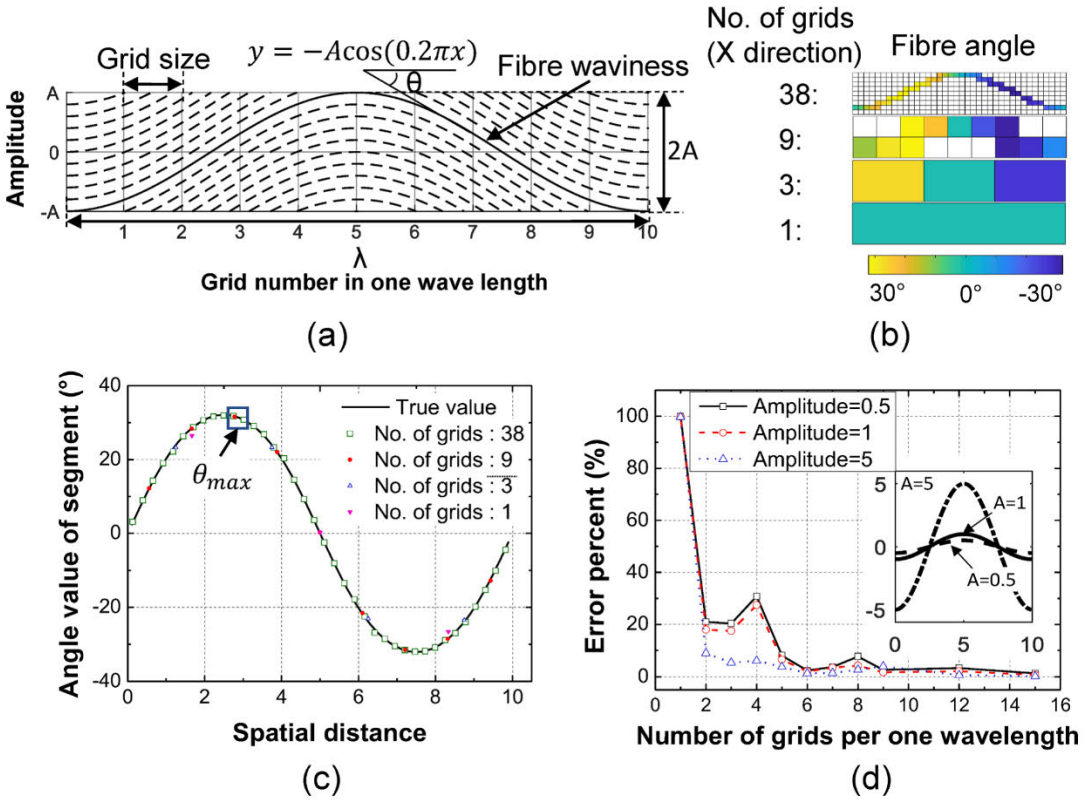

Fig. 7. Effects of grid size on the FCMA accuracy of fibre waviness: (a) idealised fibre waviness model in cosine curve, (b) measurement resolution as a function of grid size, (c) effects of grid size on the maximum fibre angles, and (d) analysis error of the maximum fibre angle at different amplitudes in one wavelength.

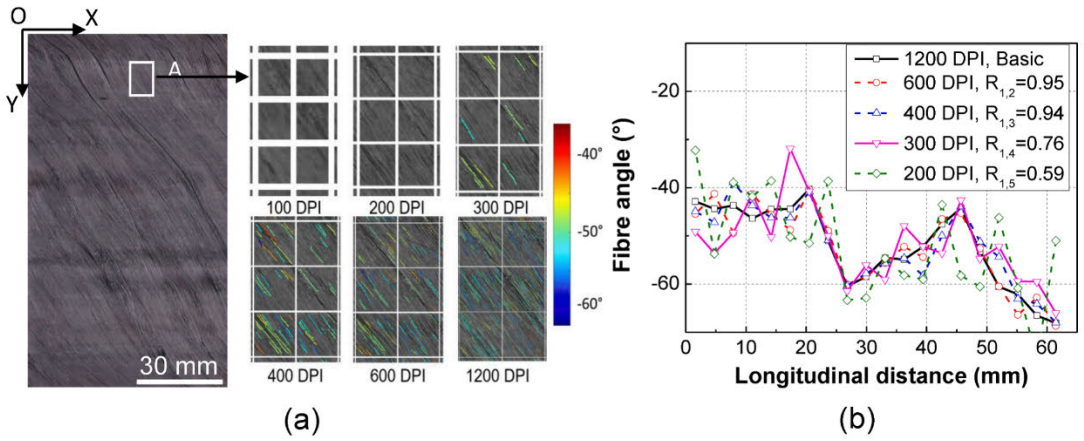

Fig. 8. (a) Effects of image resolution on FCMA preserved edges; (b) comparison of measured in-plane fibre waviness from different DPI.

× 83 mm, with off-axis wound ply and single tow, were analysed and compared. The computational time of the FCMA method will increase with the increased DPI and reduced grid size. The computational time increases 2.5 times from 600 DPI to 1200 DPI due to the increased number of detected fibres. According to the computational time and outputs analysis, the image resolution of 600 DPI effectively balances the computation time and accuracy. In contrast with the HRMA method, the computation time improved from 8.6 s to 5.4 s to process the polished image discussed in Section 4.1. This study runs on a computer with an Intel Core i7-9750H processor and 16 GB RAM.

4. FCMA application on hollow composites columns

This section will apply the FCMA method to characterise the fibre

Table 3
The effect of the image resolution on the FCMA output.

DPI		Number of edges			θ_{max}(°)	$\bar{\theta}$(°)	σ(°)
	Canny method	Valid edge	Separation ratio	Per cell			
100	–	–	–	–	–	–	–
200	1075	181	17%	0.7	69.04	−53.78	6.15
300	2957	698	24%	2.7	67.44	−53.24	5.78
400	6267	1460	23%	5.6	67.56	−53.27	6.19
600	14,554	2642	18%	10.2	66.01	−53.44	5.34
1200	52,562	5627	11%	21.6	65.66	−53.46	5.34

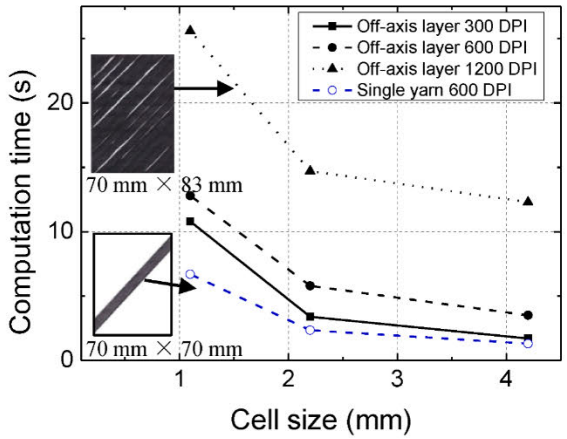

Fig. 9. The computational time at different image DPI and grid sizes.

misalignment of pultruded hollow composite columns. The out-of-plane waviness of the unidirectional fibre is analysed from the microscopic images of polished cross-sections. The in-plane waviness of wound fibre is analysed from the scanned images of fibre laminates with partial resin burn-off. The distribution of the fibre misalignment is incorporated in a verified FEM model to illustrate the usefulness of realistic fibre waviness modelling in composite structural simulation. For clarity, the proposed method is only applicable to 2D waviness measurement, not suitable for complex 3D fibre waviness.

4.1. Out-of-plane waviness measurements

When the dry preform passed through the pultrusion die, the unidirectional fibres generated the crimp due to the gap between the wound fibre, forming the out-of-plane waviness. Fig. 10(a) shows the spatial distribution of fibre misalignment characterised by the FCMA methods. Blank cells indicate there are no fibre paths identified in the cell corresponding to the cross-sections of wound fibre tows. The local details are shown in Fig. 10(b).

Table 4 compares the statistics of FCMA and HRMA in the out-of-plane waviness measurements. The FCMA method detects 2.2 times the number of edges in each grid compared to the HRMA method. The more valid fibre edges are detected, the more reliable the waviness measurements become. The measured severity of the waviness is close to each other according to the standard deviation. The difference is mainly in the maximum fibre angle. It is mainly due to some shorter edges identified by the HRMA method as effective fibre paths, which distorts the maximum fibre angle measurements.

4.2. In-plane waviness measurements

The off-axis layer image with significant waviness processed by the FCMA method is shown in Fig. 11. The preserved fibre segments in the grids are overlaid with the original image (Fig. 11(a)). Each discrete fibre is approximated to a straight line from the local details to avoid missing the maximum fibre angle, as discussed in Section 3.3.

The fibre misalignment distribution by grid means in Fig. 11(b) shows the apparent in-plane waviness. The fibre misalignment along the X-direction is more severe than in the Y-direction. Fig. 11(c) shows the fibre waviness distribution average over the X-direction grids. The fibre misalignment can be derived compared to the designed angle. Fig. 12 shows the fibre misalignment results of off-axis layers of the pultruded profile. Only the four faces of ply 8 (the outmost off-axis layer) have significant waviness, especially for the resin injection surfaces B and D. The measured results will be used for the FEM model.

Table 4
The analysis of the out-of-plane waviness by the FCMA and HRMA methods.

Method	Number		θ_{max}(°)	$\bar{\theta}$(°)	σ(°)
	Valid Cells	Edges Per cell			
FCMA	1231	6.1	5.528	1.865	2.309
HRMA	1274	2.7	7.737	2.136	2.805

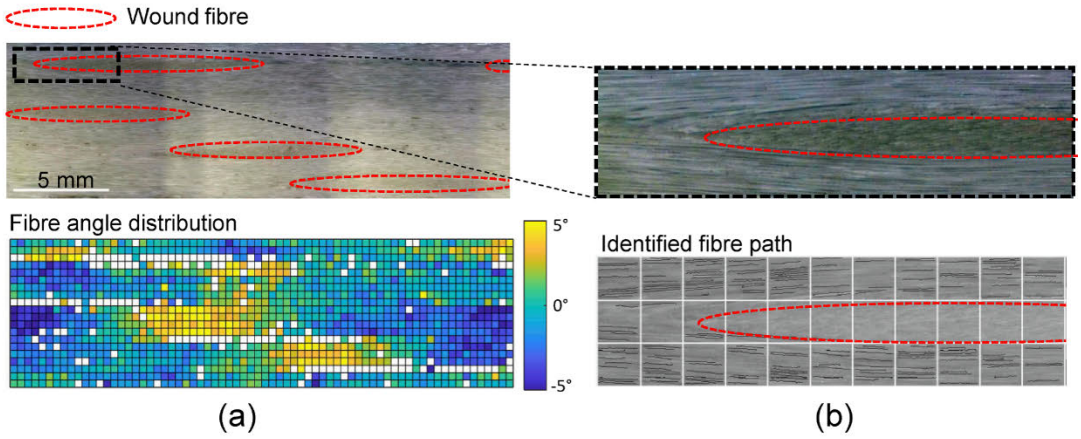

Fig. 10. Out-of-plane waviness measured by the FCMA method: (a) the spatial distribution of fibre misalignment in degrees, and (b) local detail of identified edges.

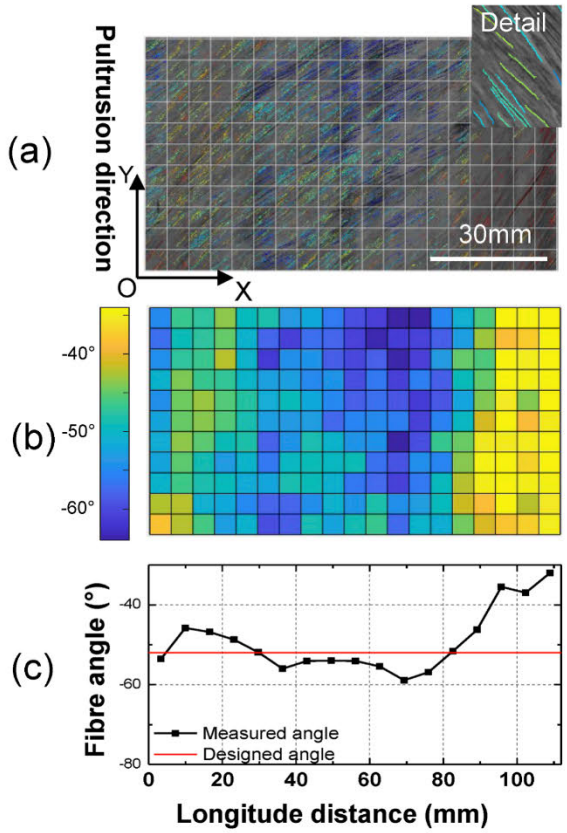

Fig. 11. In-plane waviness measured by the FCMA method: (a) detected fibres, (b) the spatial distribution of fibre misalignment, and (c) fibre angle distribution along the X-direction.

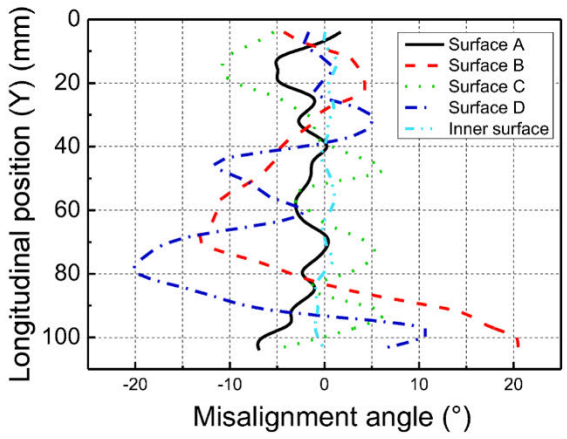

Fig. 12. The fibre misalignment results of pultruded composite hollow profile.

4.3. Finite element modelling with in-plane waviness

Abaqus/CAE 2019 was used to simulate the influence of the fibre misalignments identified by the FCMA method on the composite structural behaviour. The modelling detail can be found in the previous publication [37], where the compression behaviour of similar hollow-box profiles has been simulated with finite element modelling using the Newtonian method along with the adaptive automatic stabilisation and Hashin damage model. However, that published study did not consider fibre misalignment. The current study extended the FEM model by incorporating the measured in-plane fibre misalignment as local material orientations. The lamina mechanical properties and the strength limits of the pultruded FRP profiles are shown in Table 5.

Fig. 13(a) shows the FEM model considering the fibre misalignment by varying the local material orientation of the defective ply. The measured fibre misalignment of the off-axis layer (Ply-8) was mapped onto the elements by defining the discrete field, which was easier to implement than the geometric modelling of waviness. According to the measured results in Section 4.2, the remaining inner off-axis layers were considered defect-free. 8-node quadrilateral in-plane general-purpose continuum shells (SC8R) were used to model the test samples, with 125 mm × 125 mm × 560 mm dimensions. A mesh with a 5 mm element edge length and six elements through thickness was selected. The top and bottom surfaces were assigned a fixed and sliding boundary, respectively. The axial displacement load was applied to the sliding point.

Fig. 13(b) shows that the FEM load–displacement curves matched the experimental results closely, including a post-peak behaviour prior to the final failure. The effect of wound fibre waviness on the peak loading is approximately 1.9%, which is not significant. This is mainly because the buckling load depends mainly on the unidirectional fibre and the corner waviness of wound fibre is neglected. The wound fibre waviness has less effect on the final failure mode, reflected by the output variable (DAMAGESHR). It showed agreement with the experimental failure mode. It was confirmed that this FEM model is capable of predicting compressive behaviour with local buckling and progressive failure modes. During the linear behaviour of the load–displacement, the stress inhomogeneity of in-plane shear (S12) can be seen in the waviness region. The more significant the fibre misalignment, the more pronounced the stress concentration. The main reason is that the fibre orientation caused the change in local stiffness, which further affects the stress distribution [34]. As a comparison, there is no obvious stress concentration in the defect-free layer, illustrated by Ply-2 and Ply-8 without waviness in Fig. 13(b).

Moreover, a parametric analysis, based on the verified FEM model, has been done to show the effect of the waviness effect on the local buckling limit and the post-buckling behaviour of the hollow-box pultruded profiles to be published separately. It shows that defects at corners have a more pronounced effect on structural strength than defects in the face. The waviness has a greater impact on the compression strength at the material level than at the structural level.

5. Conclusions

A novel method for characterising fibre waviness has been proposed. This algorithm adopts a new Canny edge filter suitable for continuous fibre-reinforced composites. The current FCMA method has shown significantly improved accuracy and robustness compared to the existing HRMA method. The grid size is crucial for balancing computational efficiency and spatial resolution. The study found that a minimum of five grids per wavelength can detect the maximum fibre angle with an error below 7%.

This study applied the FCMA method to analyse in-plane and out-of-plane waviness based on the CCD scanner images as well as the optical microscopic. FCMA is capable of analysing fibre waviness in a large composite structure. The specimen area in the current research was around 100 cm^2. The FCMA method saved the computational time by about 60% compared with the HRMA method.

The FCMA results of in-plane waviness are fed as material orientation input into a FEM model of a hollow composite column under axial compression. The simulation was verified by the experiments and used

Table 5
Lamina elastic properties and strength limits of the pultruded FRP profiles.

Elastic properties	V_f(%)	E_1(MPa)	E_2(MPa)	μ_{12}	$G_{12} = G_{13}$(MPa)	G_{23}(MPa)
	60.6	45,700	12,100	0.28	4600	4000
Strength limits	X^T(MPa)	X^C(MPa)	Y^T(MPa)	Y^C(MPa)	S^L(MPa)	S^T(MPa)
	803	548	43	187	64	50

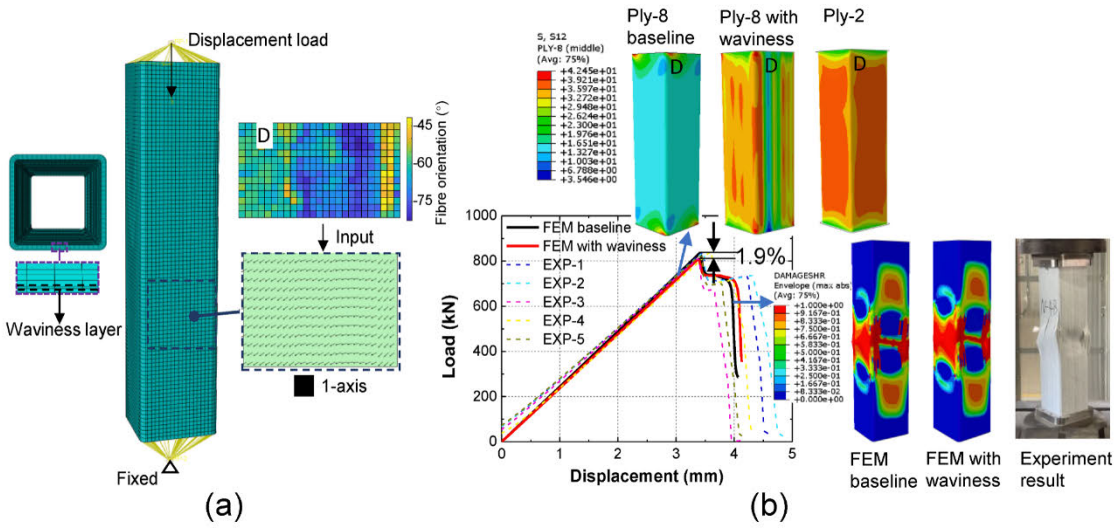

Fig. 13. (a) Finite element modelling of a pultruded hollow column with in-plane waviness under axial compression, and (b) the FE analysis and experiment results.

to show the effects of the in-plane waviness on stress distribution under axial compression. Further statistical studies are underway to correlate the defects identified by the FCMA method and the mechanical performance of composite structures.

CRediT authorship contribution statement

Songming Qi: Conceptualization, Methodology, Software, Investigation, Writing – original draft, Writing – review & editing. **Omar Alajarmeh:** Formal analysis, Methodology, Writing – review & editing. **Tristan Shelley:** Methodology, Writing – review & editing. **Peter Schubel:** Supervision, Review & editing. **Kendric Rendle-Short:** Formal analysis, Investigation, Resources. **Xuesen Zeng:** Supervision, Conceptualization, Methodology, Writing – review & editing.

Declaration of Competing Interest

The authors declare that they have no known competing financial interests or personal relationships that could have appeared to influence the work reported in this paper.

Data availability

Data will be made available on request.

Acknowledgements

The work was funded through a Cooperative Research Centres Projects (CRC-P) Grant (CRCPSIX000117).

Appendix A. Supplementary material

Supplementary data to this article can be found online at https://doi.org/10.1016/j.compstruct.2023.116666.

References

[1] Bank LC. Composites for construction: structural design with FRP materials. John Wiley & Sons; 2006.
[2] Guades E, Aravinthan T, Islam M, Manalo A. A review on the driving performance of FRP composite piles. Compos Struct 2012;94(6):1932–42.
[3] Uddin N. Developments in fiber-reinforced polymer (FRP) composites for civil engineering. Elsevier; 2013.
[4] Ascione F, Granata L, Guadagno L, Naddeo C. Hygrothermal durability of epoxy adhesives used in civil structural applications. Compos Struct 2021;265:113591.
[5] Ascione F, Granata L, Carozzi G. Flexural and shear behaviour of adhesive connections for large scale GFRP frames: Influence of the bonded area and hygrothermal aging. Compos Struct 2022;283:115122.
[6] Wagner Jr JR. Handbook of troubleshooting plastics processes: a practical guide. John Wiley & Sons; 2012.
[7] Kulkarni P, Mali KD, Singh S. An overview of the formation of fibre waviness and its effect on the mechanical performance of fibre reinforced polymer composites. Compos A Appl Sci Manuf 2020;137.
[8] Alves M, Junior CC, Ha S. Fiber waviness and its effect on the mechanical performance of fiber reinforced polymer composites: An enhanced review. Compos A Appl Sci Manuf 2021;149:106526.
[9] Thor M, Sause MGR, Hinterhölzl RM. Mechanisms of origin and classification of out-of-plane fiber waviness in composite materials—a review. J. Compos. Sci. 2020;4(3):130.
[10] Hsiao HM, Daniel IM. Effect of fiber waviness on stiffness and strength reduction of unidirectional composites under compressive loading. Compos Sci Technol 1996; 56(5):581–93.
[11] Dharan CKH, Lin C-L. Longitudinal compressive strength of continuous fiber composites. J. Compos. Mater. 2007;41:1389–405.
[12] Hamidi YK, Altan MC. Process induced defects in liquid molding processes of composites. Intern. Polymer Processing. 2017;32(5):527–44.
[13] Vallons K, Duque I, Lomov SV, Verpoest I. Loading direction dependence of the tensile stiffness, strength and fatigue life of biaxial carbon/epoxy NCF composites. Compos A Appl Sci Manuf 2011;42(1):16–21.
[14] Lemanski SL, Sutcliffe MPF. Compressive failure of finite size unidirectional composite laminates with a region of fibre waviness. Compos A Appl Sci Manuf 2012;43(3):435–44.
[15] Gholizadeh S. A review of non-destructive testing methods of composite materials. Procedia Struct Integrity 2016;1:50–7.

[16] Zardan JP, Gueudré C, Corneloup G. Study of induced ultrasonic deviation for the detection and identification of ply waviness in carbon fibre reinforced polymer. NDT E Int 2013;56:1–9.
[17] Emerson MJ, Jespersen KM, Dahl AB, Conradsen K, Mikkelsen LP. Individual fibre segmentation from 3D X-ray computed tomography for characterising the fibre orientation in unidirectional composite materials. Compos A Appl Sci Manuf 2017; 97:83–92.
[18] Nguyen NQ, Mehdikhani M, Straumit I, Gorbatikh L, Lessard L, Lomov SV. Micro-CT measurement of fibre misalignment: application to carbon/epoxy laminates manufactured in autoclave and by vacuum assisted resin transfer moulding. Compos A Appl Sci Manuf 2018;104:14–23.
[19] Yoshimura A, Hosoya R, Koyanagi J, Ogasawara T. X-ray computed tomography used to measure fiber orientation in CFRP laminates. Adv Compos Mater 2016;25 (1):19–30.
[20] Mehdikhani M, Breite C, Swolfs Y, Wevers M, Lomov SV, Gorbatikh L. Combining digital image correlation with X-ray computed tomography for characterization of fiber orientation in unidirectional composites. Compos A Appl Sci Manuf 2021; 142.
[21] Bernasconi A, Carboni M, Ribani R. On the combined use of digital image correlation and micro computed tomography to measure fibre orientation in short fibre reinforced polymers. Compos Sci Technol 2020;195.
[22] Krumenacker N, Madra A, Hubert P. Image-based characterization of fibre waviness in a representative vacuum-bagged corner laminate. Compos A Appl Sci Manuf 2020;131.
[23] Creighton CJ, Sutcliffe MPF, Clyne TW. A multiple field image analysis procedure for characterisation of fibre alignment in composites. Compos A Appl Sci Manuf 2001;32(2):221–9.
[24] Sutcliffe MPF, Lemanski SL, Scott AE. Measurement of fibre waviness in industrial composite components. Compos Sci Technol 2012;72(16):2016–23.
[25] Kratmann KK, Sutcliffe MPF, Lilleheden LT, Pyrz R, Thomsen OT. A novel image analysis procedure for measuring fibre misalignment in unidirectional fibre composites. Compos Sci Technol 2009;69(2):228–38.
[26] Wilhelmsson D, Asp LE. A high resolution method for characterisation of fibre misalignment angles in composites. Compos Sci Technol 2018;165:214–21.
[27] Kyosev Y, Aurich M. Investigations about the braiding angle and the cover factor of the braided fabrics using Image Processing and Symbolic Math Toolbox of Matlab. Adv Braiding Technol Elsevier 2016:549–69.
[28] Canny J. A computational approach to edge detection. IEEE Trans Pattern Anal Machine Intell 1986;6:679–98.
[29] Hough PV. Method and means for recognizing complex patterns. Google Patents 1962.
[30] Bao P, Lei Z, Xiaolin W. Canny edge detection enhancement by scale multiplication. IEEE Trans Pattern Anal Mach Intell 2005;27(9):1485–90.
[31] Rong W, Li Z, Zhang W, Sun L. An improved Canny edge detection algorithm. IEEE Int Conf Mech Automation 2014;2014:577–82.
[32] Oromiehie E, Prusty BG, Compston P, Rajan G. Automated fibre placement based composite structures: review on the defects, impacts and inspections techniques. Compos Struct 2019;224:110987.
[33] Wilhelmsson D, Gutkin R, Edgren F, Asp LE. An experimental study of fibre waviness and its effects on compressive properties of unidirectional NCF composites. Compos A Appl Sci Manuf 2018;107:665–74.
[34] Sitohang RDR, Grouve WJB, Warnet LL, Akkerman R. Effect of in-plane fiber waviness defects on the compressive properties of quasi-isotropic thermoplastic composites. Compos Struct 2021;272.
[35] Liu D, Fleck NA, Sutcliffe MPF. Compressive strength of fibre composites with random fibre waviness. J Mech Phys Solids 2004;52(7):1481–505.
[36] Al-saadi AU, Aravinthan T, Lokuge W. Effects of fibre orientation and layup on the mechanical properties of the pultruded glass fibre reinforced polymer tubes. Eng Struct 2019;198:109448.
[37] Alhawamdeh M, Alajarmeh O, Aravinthan T, Shelley T, Schubel P, Kemp M, et al. Modelling hollow pultruded FRP profiles under axial compression: Local buckling and progressive failure. Compos Struct 2021;262.
[38] Alajarmeh O, Zeng X, Aravinthan T, Shelley T, Alhawamdeh M, Mohammed A, et al. Compressive behaviour of hollow box pultruded FRP columns with continuous-wound fibres. Thin-Walled Struct 2021;168:108300.
[39] Banerjee A, Sun L, Mantell SC, Cohen D. Model and experimental study of fiber motion in wet filament winding. Compos A Appl Sci Manuf 1998;29(3):251–63.
[40] Roy SS, Zou W, Potluri P. Influence of braid carrier tension on carbon fibre braided preforms. In: Recent developments in braiding and narrow weaving. Springer; 2016. p. 91–102.
[41] Kugler D, Moon TJ. The effects of Mandrel material and tow tension on defects and compressive strength of hoop-wound, on-line consolidated, composite rings. Compos A Appl Sci Manuf 2002;33(6):861–76.
[42] Lightfoot JS, Wisnom MR, Potter K. A new mechanism for the formation of ply wrinkles due to shear between plies. Compos A Appl Sci Manuf 2013;49:139–47.
[43] Lightfoot JS, Wisnom MR, Potter K. Defects in woven preforms: Formation mechanisms and the effects of laminate design and layup protocol. Compos A Appl Sci Manuf 2013;51:99–107.
[44] M. Lesser, Charge coupled device (CCD) image sensors. In: High performance silicon imaging. Elsevier; 2014. p. 78–97.
[45] Grimmett G, Stirzaker D. Probability and random processes. Oxford University Press; 2020.

CHAPTER 4: PAPER 2 – FORMATION OF NON-UNIFORM FIBRE DISTRIBUTIONS IN THE WINDING-PULTRUSION PROCESS AND ITS EFFECT ON AXIAL COMPRESSIVE PROPERTIES OF HOLLOW GFRP PROFILES

4.1. Introduction

Chapter 4 explores the formation and impact of Non-Uniform Fibre Distribution (NUFD) in Pultruded Fibre Reinforced Polymer (PFRP) composite profiles. Image analysis is employed to measure the NUFD, and its effect on compressive behaviour is evaluated at both the material and structure level. The study reveals that material compressive strength decreases proportionally with the fibre volume fraction. A maximum strength reduction of 10% was observed in the tested material coupon. However, in structural applications, the strength reduction is less than 3%.

4.2. Links and implications

The characterisation of NUFD in pultruded fibre-reinforced polymer (PFRP) composite profiles can be integrated with other chapters, providing a comprehensive understanding of manufacturing-induced defects on hollow box FRP structures. By combining the effects of NUFD with fibre waviness from Chapter 3, a complete picture of how these defects interact and influence FRP composite performance can be obtained. The numerical models in Chapter 4 can be enhanced by incorporating findings from other chapters for more accurate predictions of structural performance. The implications of this chapter include the need for advanced manufacturing techniques to minimise NUFD occurrence and optimise fibre distribution. Additionally, considering the effects of NUFD in FRP structure design and analysis can lead to improved design guidelines and standards that account for manufacturing-induced defects.

4.3. Published paper

Composites: Part A 173 (2023) 107659

Contents lists available at ScienceDirect

Composites Part A

journal homepage: www.elsevier.com/locate/compositesa

Formation of non-uniform fibre distributions in winding-pultrusion process and its effect on axial compressive properties of hollow GFRP profiles

Songming Qi [a], Omar Alajarmeh [a], Tristan Shelley [a], Peter Schubel [a], Kendric Rendle-Short [b], Xuesen Zeng [a,*]

[a] University of Southern Queensland, Centre for Future Materials, Toowoomba, Queensland 4350, Australia
[b] Wagners Composite Fibre Technologies, Wellcamp, Queensland 4350, Australia

ARTICLE INFO

Keywords:
B. Defects
B. Fibre deformation
B. Mechanical properties
D. Optical microscopy
E. Pultrusion

ABSTRACT

This study investigated the formation and impact of Non-Uniform Fibre Distribution (NUFD) in pultruded Glass Fibre Reinforced Polymer (GFRP) composite profiles. These profiles, manufactured through a pull-winding process, are low-cost, high-volume structure materials. NUFD, a result of defects such as fibre waviness, wrinkling and voids, lead to differences in fibre volume fraction through the profile cross-section. Image analysis was used to measure the NUFD, and its effect on the axial compressive behaviour was evaluated at both material and structural levels. Results show that material compressive strength has a maximum strength reduction of 11% observed in the tested material coupon. In long-column structural applications governed by local buckling failure mode, the finite element analysis highlights that the corner NUFD can lead up to a 9% reduction in axial compressive peak load due to the rotation stiffness variation when corner fibre content decreases by 30%.

1. Introduction

Fibre Reinforced Polymer (FRP) composites have been widely utilised in the aerospace, defence, infrastructure, and marine sectors due to their remarkable strength-to-weight ratio, resistance to corrosion and low life-cycle maintenance[1,2]. Despite their benefits, challenges remain in manufacturing defects such as fibre misalignment, voids, and fibre waviness, especially for complex shapes [3]. Imperfections in composite materials can significantly affect their compressive properties, making it crucial to quantify their impact on material strength and failure modes for designing and optimising composite structures [4].

Prior research on the Pultruded FRP (PFRP) composites has typically assumed that the unidirectional (UD) plies are uniform and defect-free [5]. However, the use of continuous strand mats (CSMs) or wound fibre plies results in Non-Uniform Fibre Distribution (NUFD). This phenomenon was noted from the cross-section of profiles and quantified by the variations in the local fibre volume fraction (Vf) [6–8]. The NUFD is always accompanied by resin-rich pockets, mat wrapping errors, cracks, and roving shifts, which affect mechanical properties [9–12]. The influence of geometric imperfections on structural performance related to local buckling is investigated through a nonlinear geometry model [13]. The relationship between fibre content and compressive failure strength has been studied using a normalised Vf at the material level [4]. However, no research systematically examines the formation of NUFD and its influence on compressive strength both at the material and structural levels.

Quantitative techniques have been applied to analyse the NUFD in various composite shapes, including manual plotting [6], calcination tests [7], X-ray micro-computed tomography [14–16], and optical microscopes [17]. Among the techniques above, microscopic methods have the advantage of being comparatively more straightforward and cost-effective. This research will focus on an image-based analysis to measure the UD fibre content of the profile cross-sections, quantifying the exact fibre distribution as input for the finite element (FE) analysis.

Pultrusion is a cost-effective method for producing composite profiles with uniform cross-sections that can operate continuously and autonomously [18–21]. The integration of the winding process in pultrusion enhances the lateral properties of PFRP composites through continuous-wound fibres [22,23]. Fig. 1(a) depicts a typical pull-winding production line, including the pull-winding fibre preforming and pultrusion systems. The first stage involves producing the dry fibre preforms, while the second stage is for resin infusion, consolidation/curing and cutting [24]. The mandrel in the preform section is often circular to improve winding stability. A transition section is used to

* Corresponding author.
E-mail address: xuesen.zeng@usq.edu.au (X. Zeng).

https://doi.org/10.1016/j.compositesa.2023.107659
Received 12 March 2023; Received in revised form 10 May 2023; Accepted 12 June 2023
Available online 16 June 2023

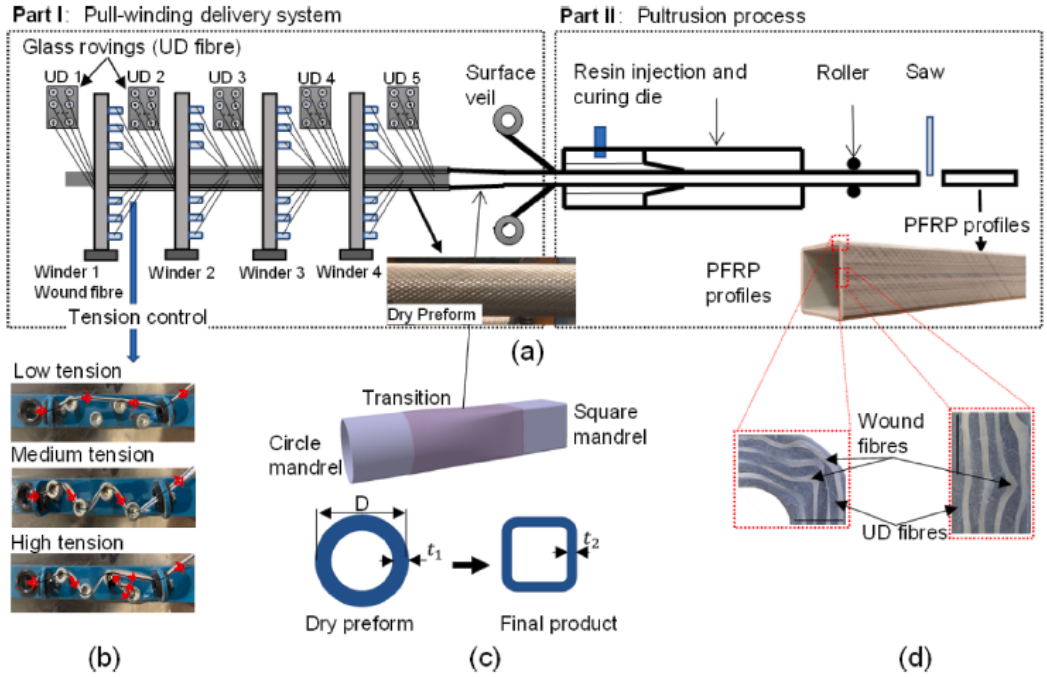

Fig. 1. (a) Illustration of pull-winding pultrusion process with a die-injection, (b) winding tension set up, (c) transition zone and thickness variation, and (d) typical non-uniform fibre distribution.

convert the cross-section based on equal circumferential perimeters for profiles with square or rectangular cross-sections, as shown in Fig. 1(c). In the final products, the wound fibres often exhibit numerous wrinkles, which are especially prevalent at the corners, and contribute to the formation of NUFDs, as shown in Fig. 1(d).

NUFD refers to the combined effects of in-plane waviness and out-of-plane waviness in composite materials. These waviness imperfections can cause the fibres to deviate from their intended alignment, leading to variations in fibre Vf and orientation within the material. Previous studies have described the mechanism of the waviness formation in the FRP composites through experiments [25–27] and numerical methods [28–30]. Waviness adversely affects mechanical performance, particularly compressive and tensile strength [31,32]. In addition, it can influence the initiation and propagation of damage [33]. In the case of pull-wound hollow FRP profiles, fibre waviness of the off-axis ply will interact with UD plies, resulting in fibre disturbance in the form of NUFD. The inter-ply interaction between fibre waviness and NUFD has not received much attention in prior publications. This research, therefore, will focus on the formation and influence of NUFD caused by waviness on the compressive strength of PFRP composite profiles.

In this research, NUFDs of varying levels were manufactured through pull-winding technology to examine the inter-ply relationship between fibre waviness and the NUFD. An image analysis-based method was employed to quantify changes in fibre Vf, providing insight into the NUFD across the cross-section. The effect of NUFD on compressive strength will be evaluated at both the material and structural levels.

2. Experimental methodology

2.1. Controlled sample manufacturing

The FRP pultruded hollow box profile in this study was manufactured by Wagners Composite Fibre Technology (WCFT) using pull-winding technology [34,35]. The specimens consist of a series of UD and off-axis E-glass fibre plies with a density of 2.54 g/cm^3. These fibres were impregnated with vinyl ester resin through an injection die. The geometric and cross-sectional details of the profile are provided in Table 1. The 0° direction aligns with the specimen's longitudinal axis (pulling direction), and the fibre content in the 0° direction constitutes 78.1% of the total fibre content.

The winding tensions were varied by controlling the yarn path with the steel pins, resulting in different initial thicknesses of the dry preform and NUFDs of the profiles. Fig. 1(b) shows three different yarn paths, representing low, medium and high winding tensions of 2.2 N, 15.3 N and 48.3 N, respectively. The fibre tension values were measured using a

Table 1
Specifications of the hollow box PFRP profiles.

Geometry			Properties		
Wall width (mm)	Wall thickness (mm)	Length (mm)	Fibre content (%)	Fibre volume fraction (%)	Stacking sequence
125	6.4	90/540	0°: 78.1 50°: 21.9	62.5	0/+50/0/-50/0/-50/0/+50/0

Table 2
Winding tension setups as illustrated in Fig. 1(b).

Samples Label	Winder 1	Winder 2	Winder 3	Winder 4
	2nd ply/+50°	4th ply/-50°	6th Layer/-50°	8th Layer/+50°
Low	Low	Low	Low	Low
Medium	Medium	Medium	Medium	Medium
High	High	High	High	High
Mixed	Medium	Medium	Medium	High

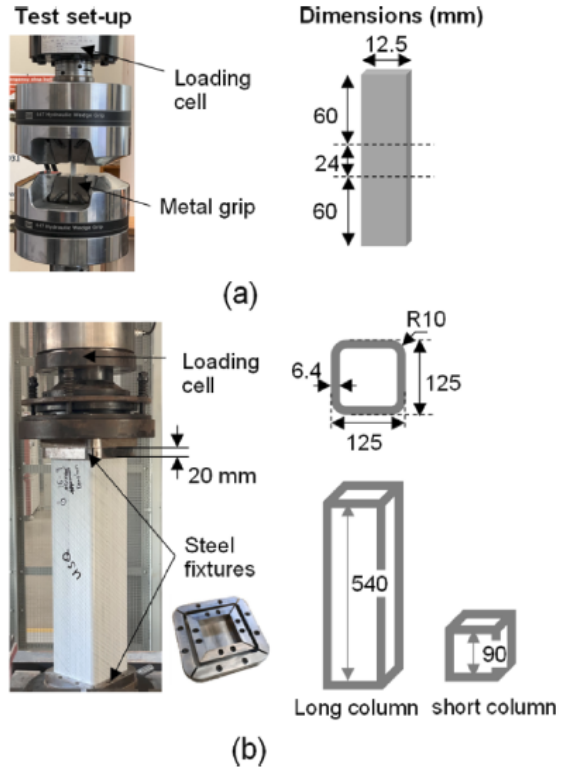

Fig. 2. Schematic of the axis compression test; (a) coupon and (b) PFRP hollow profile.

digital force gauge with a resolution of 0.1 N. Table 2 illustrates the configuration of four winders for four different specimens. Winder 1 lays out the inner off-axis ply, while Winder 4 plies out the outermost off-axis ply in the sequence illustrated in Fig. 1(a).

2.2. Specimen preparation

PFRP profiles were manufactured with four different levels of winding tension: low, medium, high and mixed tension, as shown in Table 2. Coupons and full-scale columns were prepared from the profiles for compression testing. Two groups of coupons were cut using a water-jet machine. One group contained significant NUFD, while the other did not. The columns were categorised into short columns (L90) and long columns (L540), with slenderness ratios of 0.7 and 4.3, respectively. The use of different slenderness ratios for columns allowed for the examination of compressive material failure and buckling failure. The dimensions of these samples are shown in Fig. 2.

A Struers LaboPol equipment was used to grind and polish the specimens for microscopic imaging. The grinding process utilised 1200 and 320 grit papers, followed by a three-step polishing process using DiaPro for 9 µm on an MD-largo plate, DiaPro for 3 µm on an MD-DAC cloth, and OP-U Nondry on a Neoprene cloth. The cross-sections of the samples were then imaged using a Leica DMS300.

2.3. Compression tests

Fig. 2(a) shows the coupon compression test setup using an MTS machine with a 100 kN load cell. The test was conducted at a constant displacement rate of 1 mm/min. Fig. 2(b) depicts the compression test of full-scale PFRP profiles for short and long columns using the SANS machine (SHT4206 – 2000 kN capacity). Steel fixtures were designed to reduce stress concentration and prevent premature failure at the ends. Five specimens were tested in each group to validate the test result and ensure repeatability.

3. Non-uniform fibre distribution formation and characterisation

3.1. Formation of material imperfections

The formation of the NUFD in hollow profiles occurs during the pultrusion process, as shown in Fig. 3(a). During this process, the preform (dry stack) passes through the entry bush into the pultrusion die, where compaction from the die reduces the laminate thickness (Δt). This reduction in thickness leads to excess length in the off-axis plies, resulting in fibre misalignment, in-plane waviness and out-of-plane waviness [25]. The waviness of the off-axis ply occupies the area intended for the UD ply, causing the UD fibres to move laterally and towards low-pressure zones, which results in the formation of NUFD. In extreme cases, the UD ply could be discontinuous and visible on the surface.

The imperfections representing the excess length within the off-axis ply are the in-plane waviness and misalignment, which can be evaluated by the Filtered Canny Misalignment Analysis (FCMA) method [22] based on the image process, as shown in Fig. 3(b). This method calculates the average local fibre angle in relation to the Z-axis and the fibre angle distribution along the X-axis. This ply is divided into three regions, namely zones A, B, and C. The angle distribution forms indicate the presence of fibre waviness in zone A and C and misalignment in zone B. The interface between these zones is always accompanied by significant out-of-plane waviness, as indicated by the red square in Fig. 3(b).

The out-of-plane waviness observed from the cross-section is shown in Fig. 3(c). It has been observed that the severity of out-of-plane waviness in the outer off-axis plies is more significant, as these plies have more excess length compared to the inner plies. As a result, NUFD is mainly observed in the outer UD ply of the composite material.

3.2. Excess length at different winding tension

The excess length in the off-axis plies can be evaluated by measuring the thickness change between the dry preform (t_1) and the final product (t_2), as shown in Fig. 1(c). When the winding angle is 90°, the excess length (L_{ex}) can be calculated by [36]

$$L_{ex} = \frac{2\pi(t_1 - t_2)}{4} \tag{1}$$

It should be highlighted that the final geometry of the PFRP profiles is consistent. Therefore, the excess length of the off-axis ply mainly depends on the initial thickness, which varies with different winding tensions. The initial thickness t_1 can be calculated by the measured diameter of every off-axis ply, and t_2 is measured in the final product.

Fig. 4(a) illustrates the relationship between winding tension and the diameter of each off-axis ply in the composite material. The diameter decreases as the winding tension increases. The outermost wound ply (8th ply) at mixed tension has the same thickness as the high-tension ply, even though the former off-axis layer is different. Fig. 4(b) shows the thickness change of each off-axis ply at different winding tension before and after curing. A lower winding tension leads to greater thickness variation and increased excess length in the off-axis plies. The thickness variability of the outer plies is higher than that of the inner plies, even for off-axis plies with the same winding tension, which is consistent with the observed result in Fig. 3(c).

These thickness variations can contribute to the formation of NUFD in the composite material. Different winding tensions can lead to different NUFDs in the material, highlighting the importance of process optimisation in industrial manufacturing. Furthermore, although the

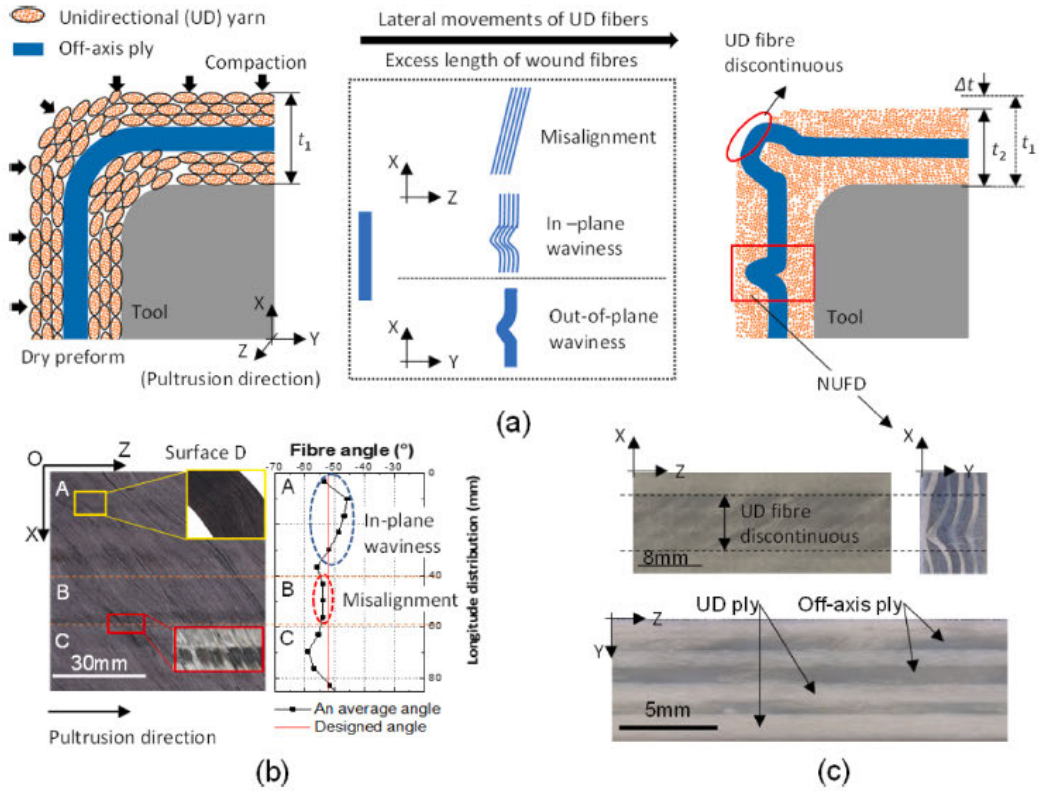

Fig. 3. The formation of the NUFD; (a) compaction of the preform, (b) defects in the off-axis ply and (c) visible discontinuity on the surface and NUFD of the cross-section.

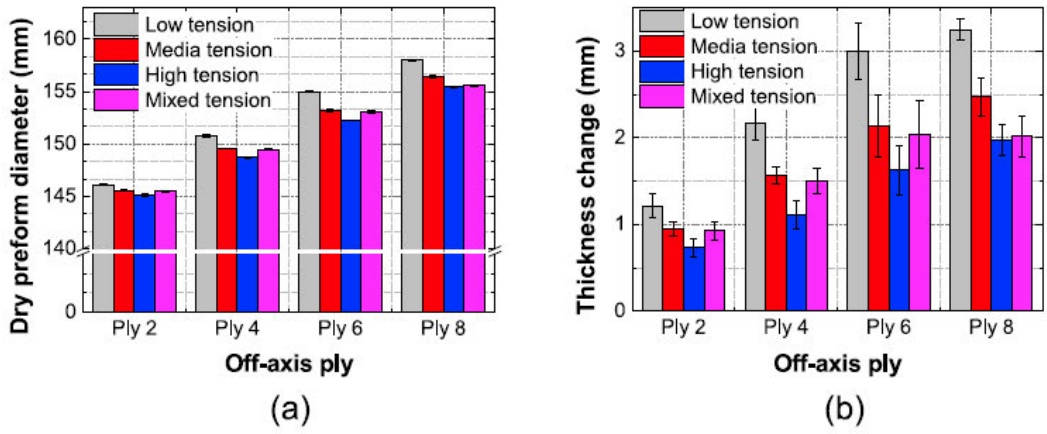

Fig. 4. Thickness change of the off-axis ply; (a) initial outer diameter of each ply and (b) final thickness change for each ply.

high-tension samples have the smallest thickness change, they can increase the pulling force and resin injection pressure during manufacturing. These factors should be considered comprehensively to achieve optimal performance and production efficiency in composite structures. Mixed tension is a balanced approach that can help to mitigate material imperfections and reduce the risk of increasing the pulling force excessively during manufacturing.

3.3. Measured volume fraction of unidirectional ply

In this study, NUFD in composite material was quantified using the change in an area of the UD ply. The content ratio of UD and wound fibre is 3.6, and each UD ply consists of three layers of UD yarn in the fibre delivery process, while the off-axis ply only has one layer. This means the thickness change of the off-axis ply can be negligible compared to

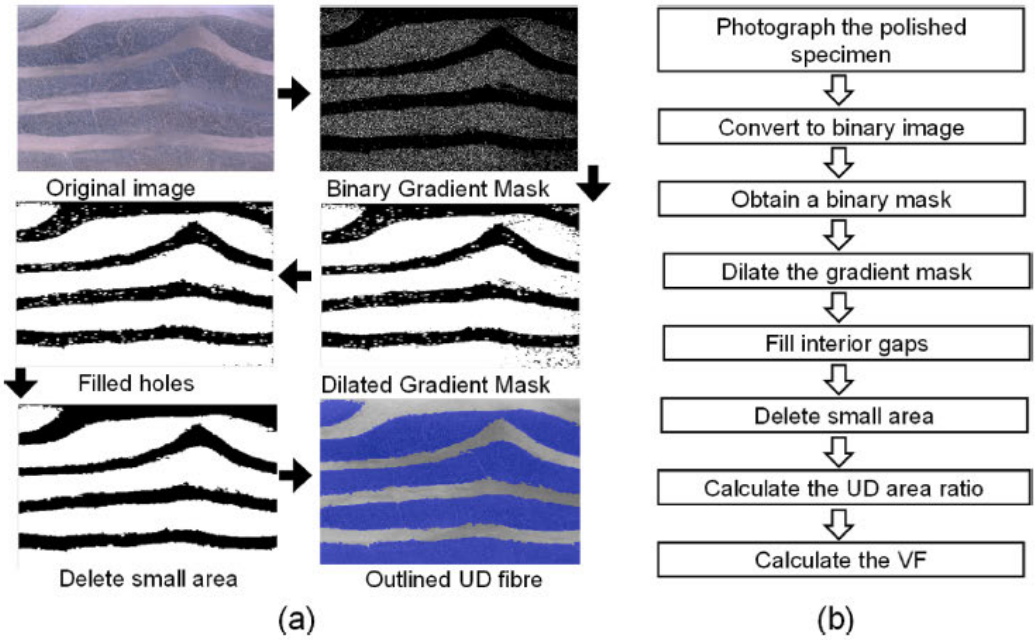

Fig. 5. Segment of UD ply; (a) image analysis and (b) process to calculate the Vf. (For interpretation of the references to colour in this figure legend, the reader is referred to the web version of this article.)

that of the UD ply. When the preform is compacted, the fibres fill the gap between the UD yarn. The UD fibres in the UD ply are assumed to be uniformly distributed for the high Vf. Due to the low volume fibre fraction in the off-axis ply, the residual resin is primarily maintained in the off-axis ply, as shown in the XZ plane of Fig. 3(c). The resin in the UD ply can be neglected compared to the off-axis ply. Therefore, the area of

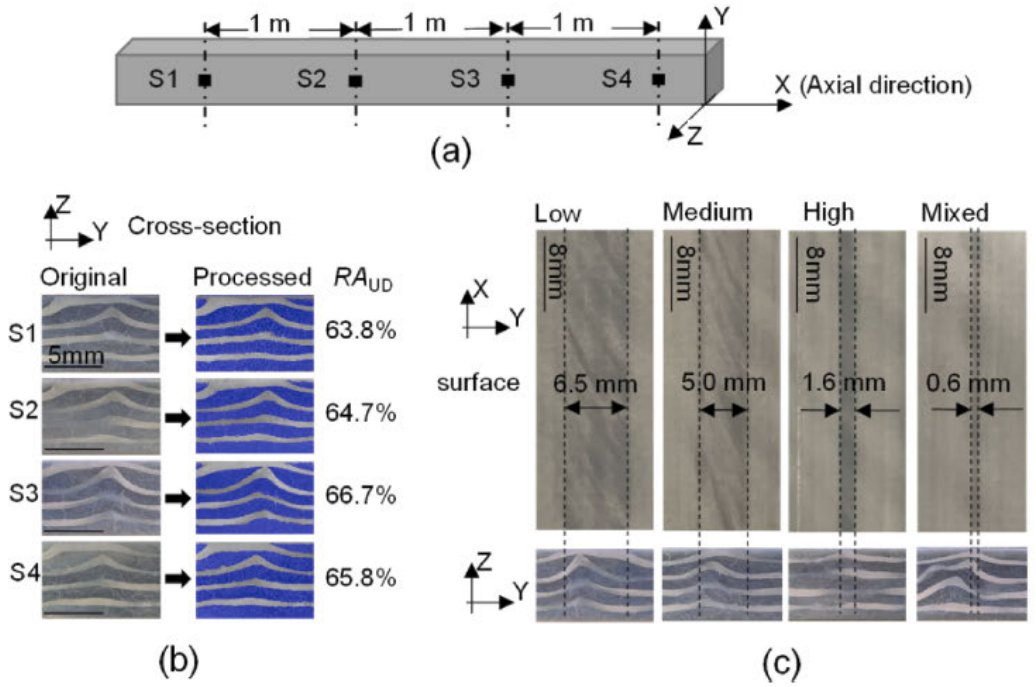

Fig. 6. The defect consistency along the profile axial direction; (a) cutting planes and (b) identified UD ply and the area ratio and (c) effect of winding tension on the top surface and cross-section of the defective coupon.

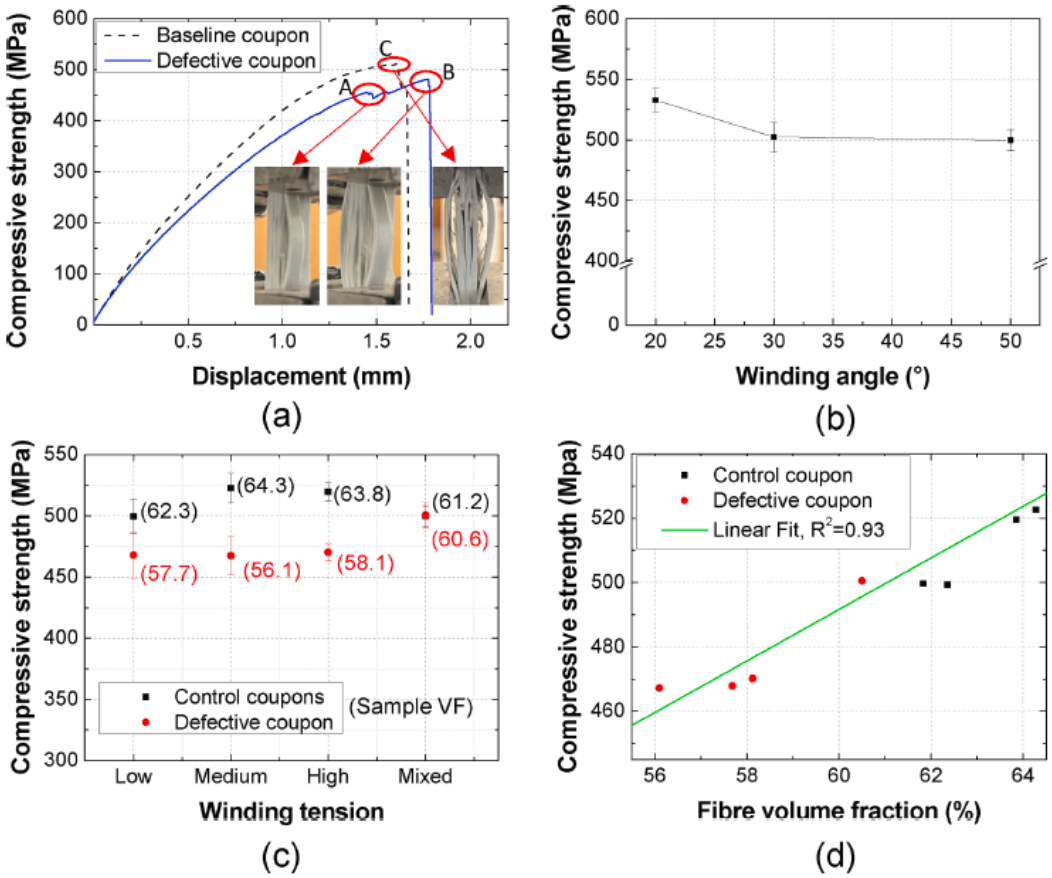

Fig. 7. Material compressive strength of coupons; (a) A typical stress-displacement curve and failure mode of the coupon with and without defects, (b) effect of winding angles, (c) effect of winding tension and (d) effect of fibre Vf.

the UD ply serves the same purpose as the UD fibre Vf in describing the NUFD along the cross-section.

The process of identifying the UD ply in the cross-section of PFRP was carried out using image analysis, which was implemented using MATLAB 2019b. The image of the cross-section was divided into small slices to reflect local Vf over the entire section. Fig. 5 shows the step for analysing one slice. This strategy was based on sufficient contrast of UD and wound plies.

The image was first converted to a greyscale image, and a threshold was used to obtain a binary mask that contains the segmented UD ply. The image was then dilated using a built-in function to reduce the gap in the lines. The residual holes in the UD ply were then filled using 'imfill' function. Then, a complement image was created to eliminate misidentified areas in the wound ply. The segment detected in the previous step in the wound ply will become the holes in the complement image. The holes in the complement image were then filled again. After the misidentified areas were eliminated, the complement image was reversed. The UD ply was marked as green areas in Fig. 5(a). The code is supplied as supplementary material to this paper.

The samples produced through the pull-winding delivery process maintain a consistent total number of UD and wound tows across different winding tensions, resulting in uniform fibre Vf of different profiles. This fibre Vf for each sample is measured by conducting a burn-out test in accordance with ISO 1172 (Table 1). This value serves as the basic fibre Vf (V_{Basic}) for the entire cross-section area. It should be noticed that UD ply and off-axis ply have the same fibre Vf in this profile, according to the product sheet. When ignoring the variation in the gap between fibres in the UD ply, the fibre Vf of ith slice V_i can be estimated as follows:

$$V_i = (1+\alpha)V_{Basic} \tag{2}$$

The coefficient α is the rate of change in the proportion of identified UD ply area compared to the average proportion of UD ply area in the cross-section.

The uniformity of the defects along the pultrusion direction is indicated by the stability of the UD ply's cross-section area of the profile. Fig. 6(a) shows that four sections were selected at one-metre intervals along the pultrusion direction. The local cross-sections with UD fibre missing were chosen to show the UD ply distribution, as shown in Fig. 6 (b). Each slice has identical defects with out-of-plane waviness of off-axis ply and UD fibre discontinuity. The ratio of UD ply's cross-sectional area to the total area (RA_{UD}) is consistent with a standard deviation of 1.3%. The uniformity of the defects along the pultrusion direction is indicated by the stability of the UD ply's cross-section area of the profile. This demonstrates the stability of NUFD along the pultrusion direction, with no observed significant out-of-plane waviness in the UD ply and only lateral movement.

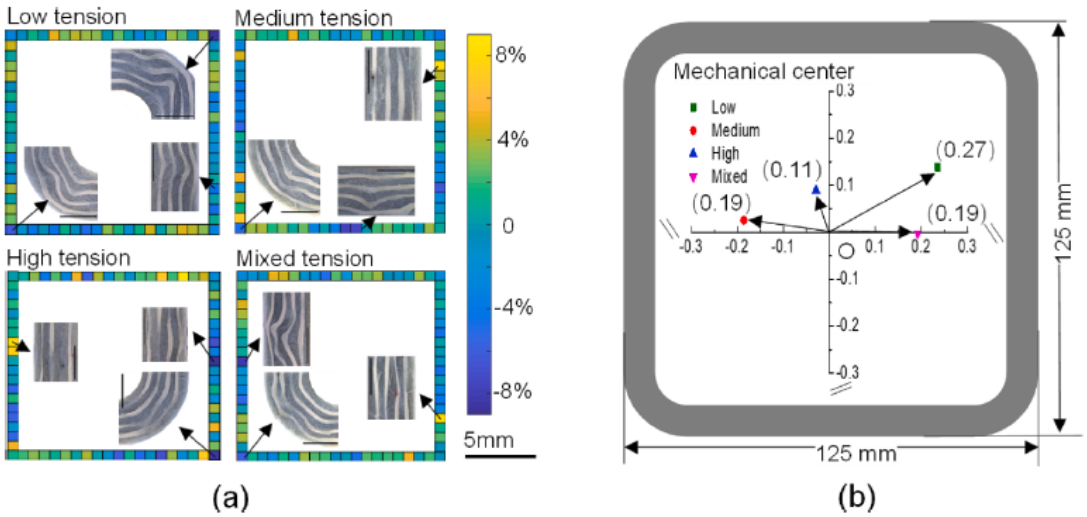

Fig. 8. Experiment measurement of (a) relative fibre Vf deviations (R_i) of the UD ply of PFRP sections and (b) its mechanical centre and eccentric distance.

4. Results and discussion

4.1. Effect of non-uniform fibre distribution on material compressive behaviour

The defective coupon in this research is defined as a discontinuity in the outermost UD ply caused by the out-of-plane waviness of the off-axis ply. This can be seen as a visible imperfection in the top surface and cross-section of the coupon, as shown in Fig. 6(c). The most extensive discontinuous piece, found in the columns at four-winding tensions, is selected as a test coupon. The discontinuous length has been marked on the top surface, as shown in Fig. 6(c). The mixed-tension samples have the least discontinuity, while the low-tension samples have the most. For comparison, baseline samples are randomly selected from the columns without significant waviness and discontinuity.

4.1.1. Effect of non-uniform fibre distribution on failure mode

The presence of NUFD in a coupon leads to early initiation of failure, particularly if there is a fibre discontinuity. This early failure initiation was observed during the experiment in the defective coupons, as shown in Fig. 7(a). The displacement-stress curve was interrupted at point A with an audible crack, resulting in a 2.5% drop in stress and a continued increase. The initial failure occurred due to partial delamination in the outermost ply, where the UD fibres were missing. However, the baseline sample exhibited a brittle behaviour until the final fracture. The final failure mode can be characterised as a fibre fraction and delamination combination.

4.1.2. Effect of non-uniform fibre distribution on compressive strength

The off-axis ply provides increased lateral strength to the profiles [37]. Three profiles were manufactured with three different winding angles (20°, 30° and 50°) to examine the impact of the winding angle on compressive strength. Fig. 7(b) showed that a winding angle of 20° resulted in a 6% increase in compressive strength compared to a 50° winding angle. However, the effect of off-axis ply on longitudinal compression strength was negligible for winding angles above 30°, which is consistent with previous findings [38]. The winding angle in this study was designed to be 50°, so it can be concluded that the in-plane waviness of the off-axis ply did not affect the compressive strength of the coupon test, and any changes in compressive strength were due to the UD fibre alone.

The results of the defective coupon test indicated that NUFD has a significant impact on compressive strength. As seen in Fig. 7(c), the compressive strength of the defective coupons was reduced by up to 11%. The lowest reduction in compressive strength was observed in the mixed-tension coupons, which had smaller discontinuities, 0.6 mm versus 6.5 mm, in the UD fibre compared to the lowest tension coupons. These results highlight the importance of controlling NUFD in the pultrusion process to maintain the mechanical properties of the composite material.

The discontinuity length presented in Fig. 6(c) takes into account the outermost ply, which is an extreme case of NUFD. On the other hand, the Vf of the coupon can also reflect the distribution of other UD plies. The results in Fig. 7(c) show that the trend of the Vf is consistent with the trend in compressive strength for various tension coupons. A Pearson correlation coefficient of 0.96 was obtained, which indicates a linear relationship between the UD ply and compressive strength, as shown in Fig. 7(d). This finding is in agreement with [39].

Table 3
The ratio of the cross-sectional area of the UD plies to the total cross-sectional area.

Samples	Wall (%)					Corner (%)		Whole (%)
	Top	Bottom	Left	Right	Dev.	Average	Dev.	Average
Low	73.9 (1.6)	73.7 (1.7)	73.2 (2.3)	72.5 (2.0)	5.1	69.1 (2.1)	9.1	72.91(2.32)
Medium	72.7 (1.4)	71.8 (2.6)	72.3 (2.6)	72.2 (2.4)	7.7	70.7 (2.3)	5.0	72.12(2.31)
High	73.4 (2.8)	72.2 (3.0)	72.4 (2.6)	71.3 (3.2)	11.2	70.4 (3.1)	8.6	72.14(2.97)
Mixed	73.3 (1.9)	73.0 (2.5)	73.4 (1.7)	72.3 (2.3)	8.5	70.7 (1.6)	5.9	72.78(2.17)

*The number between parenthesis is the standard deviation.

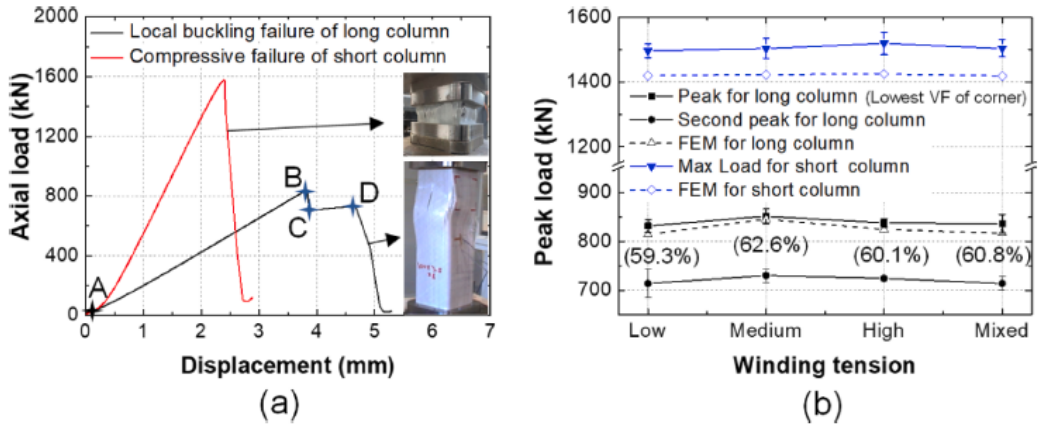

Fig. 9. Axial compression of short columns L91 and long columns L540; (a) load–displacement curves and (b) maximum peak loads, including numerical predictions and second peak loads.

4.2. Effect of non-uniform distribution on structural compressive behaviour

4.2.1. Characterisation of unidirectional fibre distribution across the section

The image analysis method is used to determine the fibre Vf across the entire cross-section. Fig. 8(a) shows 76 evenly-spaced sampling locations. Table 3 shows the ratio of the cross-sectional area of the UD ply to the total cross-sectional area for each location. The average cross-sectional area of the UD ply across all sections is similar, indicating that winding tension has no effect on the total cross-sectional area of the UD ply. This aligns with the volume of UD fibres used in the pull-winding delivery system at different winding tension manufacturing. The results demonstrate that the image analysis method effectively characterises the distribution of fibre volume across the cross-section, and its accuracy is supported by reasonable assumptions, as discussed in Section 3.3. The related cross-sectional area of the UD ply is then converted to fibre Vf using Eq. (2). The ratio of unidirectional fibres at the corner is lower compared to wall fibres, suggesting that the corner is more susceptible to NUFD.

The relative deviation of fibre Vf (R) is used to analyse the distribution of the UD ply across the PFRP cross-section through

$$R_i = \frac{V_i - V_{Basic}}{V_{Basic}} \tag{3}$$

Where R_i is the relative deviation of the Vf of ith sampling location; V_i is the calculated Vf at ith sampling location; and V_{Basic} is the average Vf of the PFRP cross-section. A negative R_i indicates that this region is probably impacted by the out-of-plane waviness of the off-axis ply, leading to the NUFD of the UD ply. The positive R_i indicates that the lateral moved UD fibres are filling the yarn space in off-axis plies. Zero means that there is a uniform distribution in this area.

Fig. 8(a) shows the relative distribution of UD fibre and its features at the extreme points for samples under different winding tensions. The results indicate the presence of the NUFD. It can be observed that the corners, particularly for the low-tension sample, are susceptible to out-of-plane waviness and discontinuity of the UD ply, resulting in a reduced fibre Vf. The accumulation of excess length is more prone to occur at the corner during the compaction of the preform [36]. The Vf of UD fibres increases near the corners as the UD fibres shift away from the corner. The low-tension sample shows the highest deviation at the corner, which is 9.1%, according to Table 3. On the other hand, the high-tension sample exhibits the highest deviation on the wall, which is around 11.2%.

Low-tension samples experience the greatest thickness change in the off-axis ply, resulting in the most severe UD ply discontinuity in the outermost ply and the lowest fibre Vf at the corner. High-tension samples have less severe out-of-plane waviness in the off-axis ply due to lower thickness changes (the lower initial excess length prior to compaction), as discussed in Section 3. The movement of UD fibres in high-tension is smoother than in low-tension samples. Mixed tension samples have less excess length in the outermost off-axis ply due to its high winding tension, but the inner plies exhibit out-of-plane waviness at the regions of minimal fibre Vf. The causes and manifestations of NUFD depend on the winding tension.

NUFD will increase the eccentricity of the cross-section, which is a factor in reducing the buckling load under axial compression. Fig. 8(b) shows the calculated mechanical centre and eccentric distance based on the fibre Vf distribution along the cross-section. The maximum eccentricity was observed in the sample with low winding tension, with an eccentric distance of 0.27 mm and a normalised value of 0.008 relative to the radius of gyration. As a comparison, the relative eccentric distance for the box section in [10] is 0.012, and the resistance reduction factor is 0.93 when the slenderness ratio is 70.

4.2.2. Compressive strength of columns

The load–displacement behaviour of columns with different slenderness ratios is depicted in Fig. 9(a). The considered ratios are 0.7 and 4.3, which result in compressive material failure and significant local buckling, respectively. The load–displacement curve for the short column exhibits a catastrophic failure, while the curve for the long column exhibits a progressive failure. The slope of the linear curve represents the axial stiffness of the column and varies with the column length. For the long column, a sudden drop in axial load resistance occurs between points B and C after the linear relationship, accompanied by local buckling in the walls. This decline from point B to C is around 12%. There is a delay between points C and D, indicating progressive failure due to the role of the wound fibre [40]. The load–displacement curve trend is similar for different winding tension samples.

Fig. 9(b) shows the experimental and numerical results for the axial compression of short columns L90 and long columns L540. For the short column, there is no significant variance in the maximum load both from experiments and numerical. For the long columns, the samples with medium tension have the highest peak load than others. Moreover, the samples with medium tension have the highest fibre Vf at the corner. The analysis of variance (ANOVA) was used to analyse differences in groups, and the calculated probability (P-value) for the maximum and second peak load was found to be 0.282 and 0.491, respectively, which is higher than the significance level (0.05). The null hypothesis is

Table 4
Elastic properties of fibre and matrix and strength limits and fracture energy values of the pultruded lamina.

Property	Description	Symbol	Value
Fibre	Young's elastic modulus/GPa	E_f	73
	Shear elastic modulus/GPa	G_f	30
	Poisson's ratio	υ_f	0.22
Matrix	Young's elastic modulus/GPa	E_m	3.4
	Shear elastic modulus/GPa	G_m	1.3
	Poisson's ratio	υ_m	0.35
Lamina strength limits (MPa)	Longitudinal tensile strength/	X^T	803
	Longitudinal compressive strength	X^C	548
	Transverse tensile strength	Y^T	43
	Transverse compressive strength	Y^C	187
	Longitudinal Shear strength	S^L	64
	Transverse Shear strength	S^T	50
Lamina fracture energy (N/mm)	Longitudinal tensile fracture energy	G_{LT}	92
	Longitudinal compressive fracture energy	G_{LC}	79
	Transverse tensile fracture energy	G_{TT}	5
	Transverse compressive fracture energy	G_{TC}	5

accepted, indicating that there is no significant difference between groups. A trend can still be found in which the maximum axial load is correlated with the lowest fibre Vf at the corner, although the variation between the samples at the corner is only about 3%. These samples in this research were optimised for industrial use, and the manufacturing process only took into account the effect of winding tension. Lower fibre Vf may be present in other pultruded composite profiles [7]. These findings will be further discussed in Section 5 using the FE model, including the analysis of worse cases and sensitive analysis of NUFD.

5. Finite element analysis of the composites with defects

5.1. Finite element modelling

Abaqus/CAE 2019 was employed to investigate the influence of the NUFD on the axial compression behaviour of composite structures. The explicit dynamic solver with the Hashin damage model was implemented to capture local buckling and prevent convergence issues. The FE analysis used 8-node quadrilateral general-purpose continuum shells (SC8R) with a mesh size of 5 mm and six elements through thickness. The strength limits and fracture energy values for the Hashin model are presented in Table 4 [41].

As shown in Fig. 10(a), the FE model accounts for the variation in fibre Vf by using a predefined field in Abaqus. The fibre Vf for each element is defined based on its coordinates. The fibre Vf remains consistent along the pultrusion direction due to the uniformity of the defects in this direction, as discussed in Section 3.3. This observation for pultruded profile is also supported by reference [7]. The properties of the fibre and resin are listed in Table 4 and obtained from [7,42]. The elastic modulus E_{11}, E_{22} and shear modulus G_{12}, G_{23} were calculated using the rule of mixture [5,43].

The results of the FE model show a good agreement with the experimental data. Fig. 10(c) shows the FE result of load–displacement curves for the low winding tension sample, which are consistent with the experimental results. The other three cases are depicted in Appendix A.

The Hashin damage initiation criteria for fibre compression (HSNFCCRT) is used to track the waviness extent, while the transverse shear damage in the matrix (DAMAGESHR) serves as an indication of delamination propagation. These criteria facilitate the tracking of the

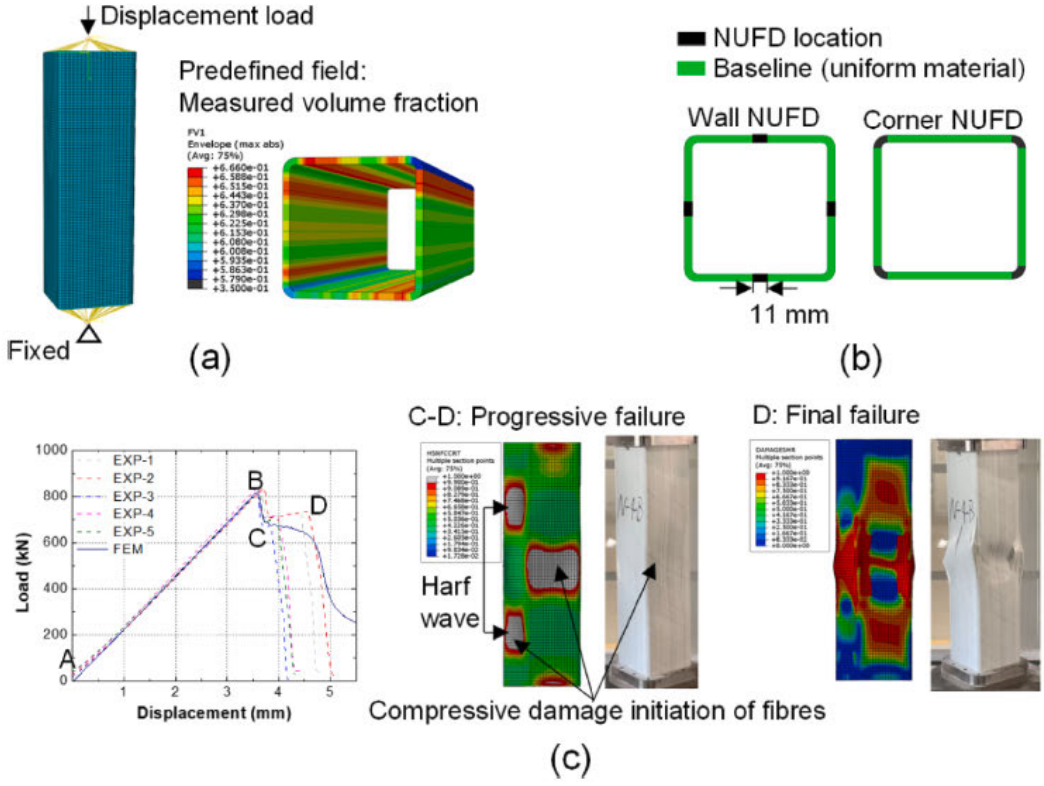

Fig. 10. (a) FE modelling of the pultruded column with NUFD, (b) defects position and (c) numerical and experimental load–displacement curves and the failure modes.

Table 5
Effect of the non-uniform fibre distribution on experimental and predicted compression strength of short columns and long columns.

Fibre distribution		Peak load- short columns L90 (kN)					Peak load- long columns L540 (kN)				
		FE model		Experiment			FE model		Experiment		
		No-Hasin	Hashin	Ave.	St.D.	COV(%)	Elastic	Hashin	Ave.	St.D.	COV(%)
Uniform		3494.2	1433.1	–	–	–	857.5	862.8	–	–	–
Non-uniform	Low	3103.2	1420.1	1496.5	21.0	1.4	813.4	817.2	832.1	12.9	1.5
	Medium	3124.2	1423.2	1503.5	30.2	2.0	849.5	850.0	851.8	14.8	1.7
	High	3053.5	1425.1	1519.2	35.1	2.3	825.4	827.5	838.0	8.9	1.1
	Mixed	3049.3	1418.9	1503.6	26.0	1.7	820.4	820.6	836.2	19.1	2.3

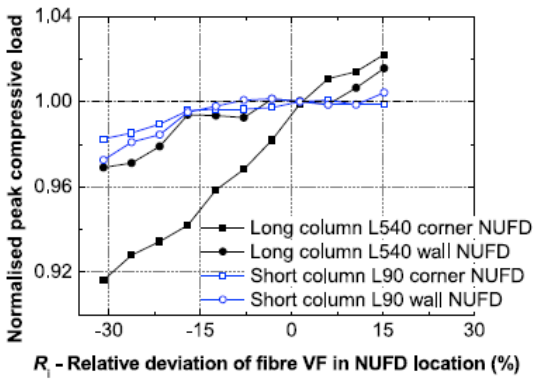

Fig. 11. Numerical analysis of defect sensitivity on the compressive peak load for the short columns L90 and the long columns L540.

respective failure modes, as described in reference [40]. Fig. 10(c) shows that this FE model can accurately capture the failure mode in comparison to the experimentally observed failure mode. The FE analysis results for buckling load under different winding tensions present the same trend as the experimental findings, even though the variation of the fibre Vf is 3%, as shown in Fig. 9(b). These results demonstrate that this FE model is reliable in predicting the buckling load of composites under axial compression.

5.2. Defect sensitivity analysis

The failure modes observed experimentally in the hollow column samples include compressive material failure for short column L90 and local buckling failure for long column L540, as shown in Fig. 9(a). The peak load in the simplified FE model without Hashin damage definition corresponds to the local structural buckling, as the material failure is suppressed. This provides a reference point to determine the failure mode when the Hashin damage is implemented. When both models predict the same peak load, the failure mode is local buckling. Otherwise, the failure mode is a compressive material failure.

Table 5 shows the comparison of these two models for the short

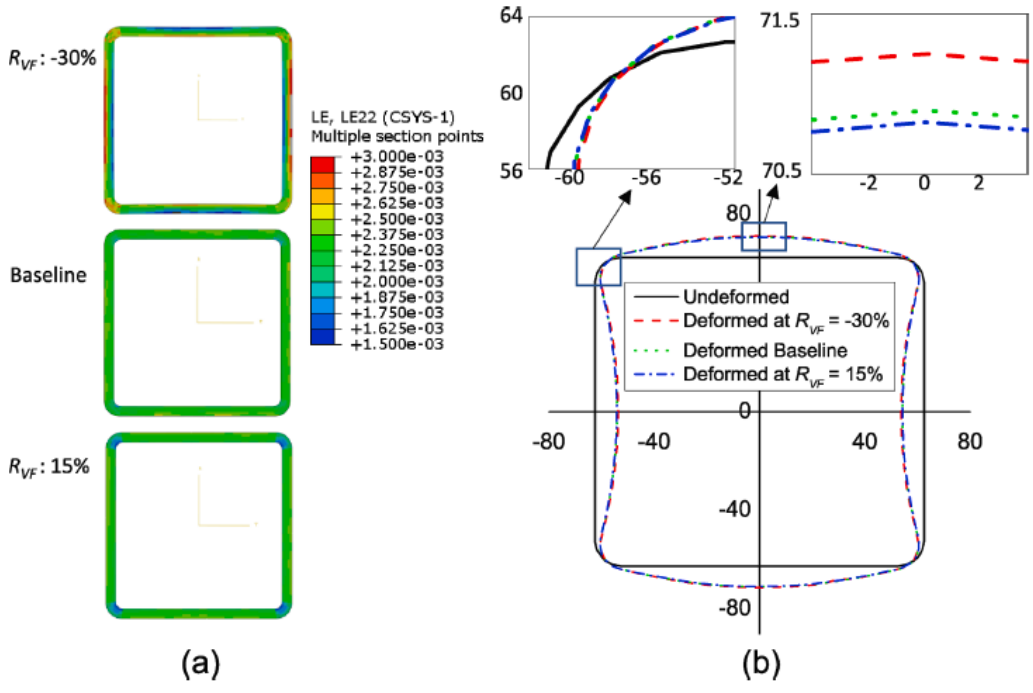

Fig. 12. Effects of corner NUFD on compressive response in the middle cross-section of the long columns L540 with corner defect; (a) logarithmic strain distribution and (b) deformation.

columns and long columns. For the short columns, the material has reached the limitation before the load capacity reaches the local buckling load from the FEM result, which is in accordance with the experimental result. For the long columns, the predicted peak values for the two models are equal, indicating that the failure is local structural buckling, as shown in Fig. 10(c).

The cross-sectional location of NUFD was a key factor in compressive performance experimentally. For example, the test samples with the medium tension have the highest peak load, of which the localised fibre Vf at the corner is the highest. In order to examine the relationship between the NUFD location and peak load, corner NUFD and wall NUFD are investigated separately. The NUFD locations in the FE model are shown in Fig. 10(b) and are marked in black. The NUFD is formed by changing the local fibre Vf in comparison to the adjacent area. The wall NUFD is 11 mm long, which has the same cross-sectional area as the corner NUFD. The baseline fibre Vf in the cross-section was 62.5%, while the relative deviation of fibre Vf in the NUFD area varies between −31% and 15%. The max load of the non-uniform material model is normalised by the max load from the baseline model ($R_{Vf} = 0$).

Fig. 11 shows the effect of the NUFD location on compressive material failure (short columns L90) and local buckling failure (long columns L540). For short column L90, NUFD location on both corners and walls has a limited effect on load capacity, which is consistent with previous findings [44]. The peak load reduction is 2% for corner NUFD and 3% for wall NUFD when the fibre Vf decreases by 30%. However, for long columns L540 with local buckling, the corner NUFD reduces the peak load by 9%, while the wall NUFD reduces the peak load by 3% when the local fibre Vf decreases by 30%. The results indicate that corner NUFD is a significant defect, as the majority of structural applications are considered as long columns and governed by local buckling failure. Furthermore, there is a linear relationship between the relative deviation of the local fibre Vf and the peak reduction factor.

The effect of corner NUFD on resistance to buckling load in hollow profiles can be assessed by the rotation stiffness of the corner [45]. A change in the fibre Vf at the corner resulted in a variation in the corner rotation stiffness. As shown in Fig. 12(a), there is a change in logarithmic strain with the fibre Vf at the corner in the tangential direction of the cylindrical coordinate at the same loading displacement point. It can be observed that the strain along the cross-section decreases with an increase in the fibre Vf due to the higher corner rotation stiffness. This observation aligns with the findings reported in the reference [46], which suggest that increasing the corner area can effectively reduce stress concentration. When local buckling occurs in the column, the deformation of the local buckling plane can be observed in Fig. 12(b). The lower corner fibre Vf leads to a larger displacement at the buckling plane. The results indicate that the rotation stiffness at the corner plays an important role in local buckling in the hollow profiles, which is consistent with the plate theory [47].

6. Conclusions

This paper investigates the formation of Non-uniform Fibre Distribution (NUFD) in Pultruded Fibre Reinforced Polymer (PFRP) and its effects on the material and structural behaviour under axial compression. The following conclusions are drawn from the study.

- The excess length of the off-axis layer generates fibre waviness due to compaction through the pultrusion die, leading to the formation of NUFD in the cross-section. A MATLAB-based image analysis was developed to measure the localised fibre Vf variation. Results show that the samples with the lowest winding tension exhibit the largest reduction in fibre content, with a decrease of up to 9% at the corner. In addition, the fibre distribution remains consistent along the axial pultrusion direction.
- The influence of the NUFD on the material compressive strength was investigated by testing coupons with visible surface fibre discontinuities. Results showed that fibre discontinuities had a negative effect on material strength under axial compression. Specifically, when the fibre Vf decreased by 12%, the load capacity of the coupon decreased by 11%.
- A FE model with measured localised fibre Vf was developed to evaluate the effect of the NUFD on compressive material failure and local buckling failure in short columns and long columns. The NUFD has a limited effect on the load-bearing capacity of short columns. However, for the corner NUFD in long columns, the reduction peak load is significant, up to 9%. The modelling highlights that the variation in rotational stiffness at the corner is crucial to the local buckling load capacity of hollow composite columns.

CRediT authorship contribution statement

Songming Qi: Conceptualization, Methodology, Software, Investigation, Writing – original draft, Writing – review & editing. **Omar Alajarmeh**: Formal analysis, Methodology, Writing – review & editing. **Tristan Shelley**: Methodology, Writing – review & editing. **Peter Schubel**: Supervision, Writing – review & editing. **Kendric Rendle-Short**: Formal analysis, Investigation, Resources. **Xuesen Zeng**: Supervision, Conceptualization, Methodology, Writing – review & editing.

Declaration of Competing Interest

The authors declare that they have no known competing financial interests or personal relationships that could have appeared to influence the work reported in this paper.

Data availability

No data was used for the research described in the article.

Acknowledgements

The work was funded through a Cooperative Research Centres Projects (CRC-P) Grant (CRCPSIX000117).

Appendix A. FEM vs experimental load-displacement curves

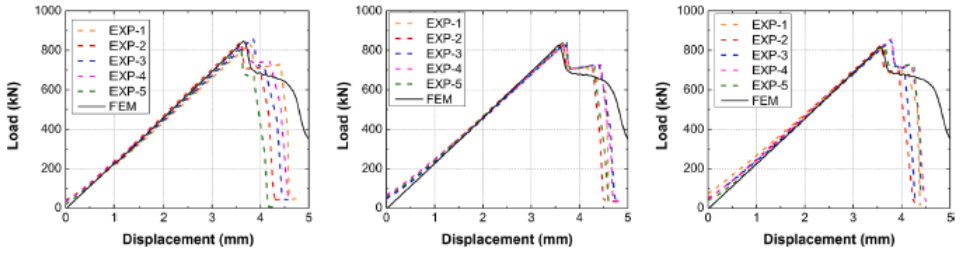

(a) Samples with Medium Tension (b) Samples with High Tension (c) Samples with Mixed Tension

Appendix B. Supplementary data

Supplementary data to this article can be found online at https://doi.org/10.1016/j.compositesa.2023.107659.

References

[1] Guades E, Aravinthan T, Islam M, Manalo A. A review on the driving performance of FRP composite piles. Compos Struct 2012;94(6):1932–42.
[2] Hollaway L. A review of the present and future utilisation of FRP composites in the civil infrastructure with reference to their important in-service properties. Constr Build Mater 2010;24(12):2419–45.
[3] Hassan MH, Othman AR, Kamaruddin S. A review on the manufacturing defects of complex-shaped laminate in aircraft composite structures. Int J Adv Manuf Technol 2017;91(9):4081–94.
[4] Mahadik Y, Hallett SR. Effect of fabric compaction and yarn waviness on 3D woven composite compressive properties. Compos A Appl Sci Manuf 2011;42(11):1592–600.
[5] Barbero EJ. Introduction to composite materials design. CRC Press; 2010.
[6] Poulton M, Sebastian W. Taxonomy of fibre mat misalignments in pultruded GFRP bridge decks. Composites Part A: Applied Science and Manufacturing; 2021. p. 142.
[7] Feng P, Wu Y, Liu T. Non-uniform fiber-resin distributions of pultruded GFRP profiles. Composites Part B: Engineering; 2021.
[8] Yuksel O, Sandberg M, Hattel JH, Akkerman R, Baran I. Mesoscale process modeling of a thick pultruded composite with variability in fiber volume fraction. Materials (Basel) 2021;14(13).
[9] Bednarcyk BA, Aboudi J, Arnold SM. The effect of general statistical fiber misalignment on predicted damage initiation in composites. Compos B Eng 2014;66:97–108.
[10] Potter K, Khan B, Wisnom M, Bell T, Stevens J. Variability, fibre waviness and misalignment in the determination of the properties of composite materials and structures. Compos A Appl Sci Manuf 2008;39(9):1343–54.
[11] Ghayoor H, Marsden CC, Hoa SV, Melro AR. Numerical analysis of resin-rich areas and their effects on failure initiation of composites. Compos A Appl Sci Manuf 2019;117:125–33.
[12] Safonov A, Gusev M, Saratov A, Konstantinov A, Sergeichev I, Konev S, et al. Modeling of cracking during pultrusion of large-size profiles. Compos Struct 2020;235:111801.
[13] Ascione L, Berardi VP, Giordano A, Spadea S. Pre-buckling imperfection sensitivity of pultruded FRP profiles. Compos B Eng 2015;72:206–12.
[14] Baran I, Straumit I, Shishkina O, Lomov SV. X-ray computed tomography characterization of manufacturing induced defects in a glass/polyester pultruded profile. Compos Struct 2018;195:74–82.
[15] Mehdikhani M, Breite C, Swolfs Y, Wevers M, Lomov SV, Gorbatikh L. Combining digital image correlation with X-ray computed tomography for characterization of fiber orientation in unidirectional composites. Composites Part A: Applied Science and Manufacturing; 2021. p. 142.
[16] Nguyen NQ, Mehdikhani M, Straumit I, Gorbatikh L, Lessard L, Lomov SV. Micro-CT measurement of fibre misalignment: Application to carbon/epoxy laminates manufactured in autoclave and by vacuum assisted resin transfer moulding. Compos A Appl Sci Manuf 2018;104:14–23.
[17] Qi S, Alajarmeh O, Shelley T, Schubel P, Rendle-Short K, Zeng X. Fibre waviness characterisation and modelling by Filtered Canny Misalignment Analysis (FCMA). Compos Struct 2023;307:116666.
[18] Baran I. Pultrusion: state-of-the-art process models. Smithers Rapra 2015.
[19] Fairuz A, Sapuan S, Zainudin E, Jaafar C. Polymer composite manufacturing using a pultrusion process: A review. Am J Appl Sci 2014;11(10):1798.
[20] Ramôa Correia J. 9 - Pultrusion of advanced fibre-reinforced polymer (FRP) composites. In: Bai J, editor. Advanced Fibre-Reinforced Polymer (FRP) Composites for Structural Applications: Woodhead Publishing; 2013. p. 207-51.
[21] Struzziero G, Maistros GM, Hartley J, Skordos AA. Materials modelling and process simulation of the pultrusion of curved parts. Compos A Appl Sci Manuf 2021;144:106328.
[22] Alajarmeh O, Zeng X, Aravinthan T, Shelley T, Alhawamdeh M, Mohammed A, et al. Compressive behaviour of hollow box pultruded FRP columns with continuous-wound fibres. Thin-Walled Struct 2021;168:108300.
[23] Mindermann P, Witt M-U, Gresser GT. Pultrusion-winding: A novel fabrication method for coreless wound fiber-reinforced thermoset composites with distinct cross-section. Compos A Appl Sci Manuf 2022;154:106763.
[24] Sandberg M, Yuksel O, Baran I, Hattel JH, Spangenberg J. Numerical and experimental analysis of resin-flow, heat-transfer, and cure in a resin-injection pultrusion process. Compos A Appl Sci Manuf 2021;143:106231.
[25] Lightfoot JS, Wisnom MR, Potter K. A new mechanism for the formation of ply wrinkles due to shear between plies. Compos A Appl Sci Manuf 2013;49:139–47.
[26] Hallander P, Akermo M, Mattei C, Petersson M, Nyman T. An experimental study of mechanisms behind wrinkle development during forming of composite laminates. Compos A Appl Sci Manuf 2013;50:54–64.
[27] Nosrat Nezami F, Gereke T, Cherif C. Analyses of interaction mechanisms during forming of multilayer carbon woven fabrics for composite applications. Compos A Appl Sci Manuf 2016;84:406–16.
[28] Sjölander J, Hallander P, Åkermo M. Forming induced wrinkling of composite laminates: A numerical study on wrinkling mechanisms. Compos A Appl Sci Manuf 2016;81:41–51.
[29] Thompson AJ, Belnoue JPH, Hallett SR. Modelling defect formation in textiles during the double diaphragm forming process. Composites Part B: Engineering; 2020. p. 202.
[30] Naouar N, Vidal-Salle E, Schneider J, Maire E, Boisse P. Meso-scale FE analyses of textile composite reinforcement deformation based on X-ray computed tomography. Compos Struct 2014;116:165–76.
[31] Kulkarni P, Mali KD, Singh S. An overview of the formation of fibre waviness and its effect on the mechanical performance of fibre reinforced polymer composites. Composites Part A: Applied Science and Manufacturing; 2020. p. 137.
[32] Alves MP, Cimini Junior CA, Ha SK. Fiber waviness and its effect on the mechanical performance of fiber reinforced polymer composites: An enhanced review. Composites Part A: Applied Science and Manufacturing; 2021. p. 149.
[33] Carraro P, Maragoni L, Quaresimin M. Influence of manufacturing induced defects on damage initiation and propagation in carbon/epoxy NCF laminates. Adv Manuf Polym Compos Sci 2015;1(1):44–53.
[34] Guades E, Aravinthan T, Islam MM. Characterisation of the mechanical properties of pultruded fibre-reinforced polymer tube. Mater Des 2014;63:305–15.
[35] Al-saadi AU, Aravinthan T, Lokuge W. Effects of fibre orientation and layup on the mechanical properties of the pultruded glass fibre reinforced polymer tubes. Eng Struct 2019;198.
[36] Thompson AJ, McFarlane JR, Belnoue JPH, Hallett SR. Numerical modelling of compaction induced defects in thick 2D textile composites. Mater Des 2020;196.
[37] Haj-Ali R, Kilic H. Nonlinear behavior of pultruded FRP composites. Compos B Eng 2002;33(3):173–91.
[38] Zhang S, Caprani C, Heidarpour A. Influence of fibre orientation on pultruded GFRP material properties. Compos Struct 2018;204:368–77.
[39] Sitohang RDR, Grouve WJB, Warnet LL, Akkerman R. Effect of in-plane fiber waviness defects on the compressive properties of quasi-isotropic thermoplastic composites. Compos Struct 2021;272.
[40] Alhawamdeh M, Alajarmeh O, Aravinthan T, Shelley T, Schubel P, Kemp M, et al. Modelling hollow pultruded FRP profiles under axial compression: Local buckling and progressive failure. Compos Struct 2021;262.

[41] Sharma AP, Khan SH, Parameswaran V. Experimental and numerical investigation on the uni-axial tensile response and failure of fiber metal laminates. Compos B Eng 2017;125:259–74.
[42] Huang W, Causse P, Hu H, Belouettar S, Trochu F. Transverse compaction of 2D glass woven fabrics based on material twins - Part I: Geometric analysis. Compos Struct 2020;237:10.
[43] Huang ZM. Micromechanical strength formulae of unidirectional composites. Mater Lett 1999;40(4):164–9.
[44] Zhang L, Zhang S, Xu D, Chen X. Compressive behavior of unidirectional FRP with spacial fibre waviness and non-uniform fibre packing. Compos Struct 2019;224:111082.
[45] Liu T, Harries KA. Flange local buckling of pultruded GFRP box beams. Compos Struct 2018;189:463–72.
[46] Alhawamdeh M, Alajarmeh O, Aravinthan T, Shelley T, Schubel P, Mohammed A, et al. Design optimisation of hollow box pultruded FRP profiles using mixed integer constrained Genetic algorithm. Compos Struct 2022;302:116247.
[47] Kollár L, Springer G. Thin Plates. In: Springer GS, Kollár LP, editors. Mechanics of Composite Structures. Cambridge: Cambridge University Press; 2003. p. 89–168.

CHAPTER 5: PAPER 3 – FORMATION OF NON-UNIFORM FIBRE DISTRIBUTION AND ITS EFFECT ON THE FLEXURAL PERFORMANCE OF PULTRUDED GFRP BOX BEAMS

5.1. Introduction

Chapter 5 explores the effect of Non-Uniform Fibre Distribution (NUFD) on the flexural performance of pultruded GFRP box beams. Experimental and numerical analyses reveal that corner NUFD has a greater negative impact on local buckling capacity than flange NUFD, while the effect of NUFD location is insignificant to failure determined by material strength without buckling instability. A linear relationship between the rotational restraint coefficient and corner fibre volume fraction is established, providing insight into the influence of material imperfections on load capacity.

5.2. Links and implications

The findings in Chapter 5, focusing on the impact of NUFD on the flexural performance of pultruded GFRP box beams, can be connected with other chapters in the thesis to better understand the influence of manufacturing-induced defects on hollow box FRP structures. By incorporating the insights from Chapter 3 on fibre waviness and Chapter 4 on NUFD formation, a more comprehensive understanding of the complex interactions between these defects and their effects on FRP composite performance can be achieved. The implications of this chapter include the need for improved manufacturing processes to mitigate NUFD and refine the overall quality of FRP structures. Furthermore, integrating the effects of NUFD into the design and analysis of FRP structures can lead to enhanced design guidelines and standards that consider the impact of manufacturing-induced defects on structural behaviour and performance.

5.3. Published paper

Formation of non-uniform fibre distribution and its effect on the flexural performance of pultruded GFRP box beams

Songming Qi[1]*, Omar Alajarmeh[1], Mohammad Alhawamdeh[2], Tristan Shelley[1], Peter Schubel[1], Kendric Rendle-Short[3], Xuesen Zeng[1]

* Corresponding author: E-mail address: songming.qi@usq.edu.au

[1] University of Southern Queensland, Centre for Future Materials, Toowoomba Queensland Australia 4350

[2] Tafila Technical University, Department of Civil Engineering, Tafila Jordan 66110

[3] Wagners Composite Fibre Technologies, Wellcamp Queensland Australia 4350

Abstract

This study investigates the effect of non-uniform fibre distribution (NUFD) as a defect in the pull-winding manufacturing process on the mechanical properties of hollow pultruded glass fibre-reinforced polymer (GFRP) profiles. These profiles exhibit balanced mechanical properties but are susceptible to NUFD during production, negatively affecting local buckling capacity. Experimental and numerical analyses were conducted on pultruded GFRP profiles manufactured under three winding tension configurations, resulting in a 5% variance in load capacity during bending. Results show that corner NUFD influences local buckling capacity more than flange NUFD. Specifically, corner NUFD decreases load capacity by up to 20%, while flange NUFD increases it by up to 3%. Conversely, the effect of NUFD location is insignificant to the failure determined by the material strength without buckling instability. Moreover, a linear relationship between the rotational restraint coefficient and corner fibre volume fraction provides insight into the impact of material imperfections on load capacity.

Keywords: Defects, Flexural stability, Local buckling, Pultrusion, Fibre-reinforced polymer

1. Introduction.

Pultruded fibre-reinforced polymer (PFRP) profiles have gained widespread use in civil infrastructure applications due to their high strength-to-weight ratio, corrosion resistance and low maintenance requirements [1-4]. However, due to the low stiffness and anisotropic nature of PFRP, deflections and buckling instabilities are commonly observed in structures subjected to axial and flexural loading, particularly in thin-walled structures [5-7]. Local buckling, which

occurs prior to material failure, is a critical factor in predicting the structural capacity of the PFRP sections [8-10].

Local buckling analysis of the PFRP profile is typically performed using the plate theory [11-13], with separate calculations for the flange and web loading capacities and considering the flexibility of the flange-web connections. Qiao et al. [14] presented an explicit formulation and elastic constraint coefficient to determine the local buckling capacity of a box section under compression loading. Kollár [15] proposed a refined equation for the constraint coefficient at the corners. It should be noted that local buckling in PFRP profiles under compression loading differs from that under bending loading, as only the top flange and partial web buckle are under compression [16]. Liu et al. [17] investigated the contribution of the rotational stiffness at the flange-web junction to flange local buckling (FLB) under bending. They found that the fibre-matrix architecture would affect the stiffness of flange edge support. Further research is required to fully understand the impact of fibre-matrix architecture on local buckling behaviour in PFRP profiles.

Pull-winding technology, a combination of pultrusion and filament winding, is a high-volume and cost-effective production method [18, 19], as shown in Fig. 1(a). This process utilises continuous-wound fibres to reinforce the lateral properties of PFRP composites [20, 21]. The wound fibre increases the rotation stiffness at the corner to resist local buckling [22]. However, the wound fibres are susceptible to causing non-uniform fibre distribution (NUFD) across the cross-section of PFRP profiles. When the dry fibre preform produced in the pull-winding process passes into and through the pultrusion die, the associated compaction generates excess length in the wound fibres, leading to both in-plane and out-of-plane waviness [23]. The interaction between wavy fibres and unidirectional (UD) fibres leads to lateral shifting in the latter. As a result, the cross-section exhibits NUFD, particularly in the corner (Fig. 1(c)).

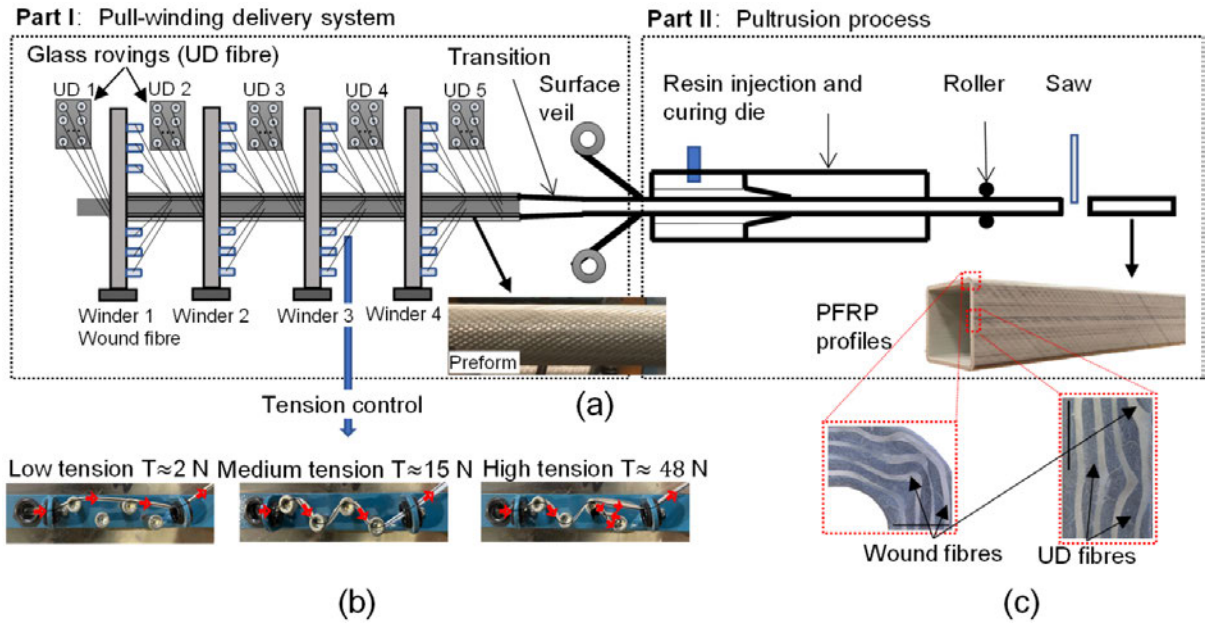

Fig. 1. Illustration of pull-winding pultrusion process and its products; (a) pull-winding technique, (b) winding tension control and (c) non-uniform fibre distribution.

Winding tension is a critical manufacturing factor influencing the initial thickness of the fibre preform [24]. The winding tension is controlled by the yarn path with steel pins [25] (Fig. 1(b)); higher tension generates a thinner preform but also increases the resin injection pressure and pulling force. This research used three different winding tensions to manufacture profiles to obtain varying degrees of NUFD.

The presence of NUFD in the PFRP profiles can negatively impact the structural integrity and mechanical performance. The influence of NUFD on mechanical strength is regulated in the Chinese standard GB/T 31539-2015 [26]. Zhang et al. [27] found that non-uniform fibre packing over a cross-section has a limited effect on compressive strength based on the finite element (FE) model. However, their study did not take into account the individual lamina in the preform and specific locations of defects in full-scale profiles. Feng. et al. [28] reported NUFD significantly impacts the global buckling of PFRP profiles. For I-sections with a slenderness ratio of 70, NUFD resulted in a reduction factor of 0.88. However, no study was found on the effect of NUFD on the flexural performance of PFRP profiles. This research will focus on the NUFD effect on flexural behaviour.

The characterisation of non-uniform fibre-resin distribution (e.g. fibre wrinkle, fibre flip, fibre waviness and resin-rich zone) has been discussed previously, and its influence on the performance of FRP composites has been examined. Wilhelmsson et al. [29] presented a high-

resolution misalignment analysis to identify the maximum fibre misalignment to predict the compressive strength of non-crimp fabrics, while Qi et al. [30] showed the effect of fibre misalignment on stress distribution using the FE method. Poulton and Sebastian [31] presented a taxonomy of mat misalignment by comparing the actual location to the idealised location using manually plotted points. Feng et al. [28] adopted the calcination test to measure the resin content in the specified locations from different FRP sections. In addition, X-ray micro-computed tomography was used to characterise the internal geometry of the resin-rich area [32]. Netzel et al. [33] quantified the wrinkling severity and material flow with an optical microscope. This research adopts an image analysis method to measure the UD fibre content along the cross-section, offering more details on the fibre distribution and facilitating a more accurate FE modelling.

In this research, box section PFRP profiles manufactured with various wound fibre tension were tested under bending to examine the effect of the NUFD on FLB experimentally and numerically. The NUFD was considered by changing the fibre volume fraction across the section, which is more convenient than the calcination method. A numerical model was built up and verified to study the sensitivity of the buckling load towards the NUFD under four-point bending based on the predefined fibre distribution. The results demonstrated the significance of considering the material imperfection effect on the flexural load capacity.

2. Experimental program

In this research, two different sizes of hollow box profiles, S100 and S125, were manufactured using pull-winding technology by Wagners Composite Fibre Technology (WCFT). The profiles were made from E-glass fibres with a density of 2.54 g/cm^3, impregnated via an injection die using vinyl ester resin. Fig. 2(a) shows the geometric and cross-sectional detail of the profile, and the specifications are listed in Table 1.

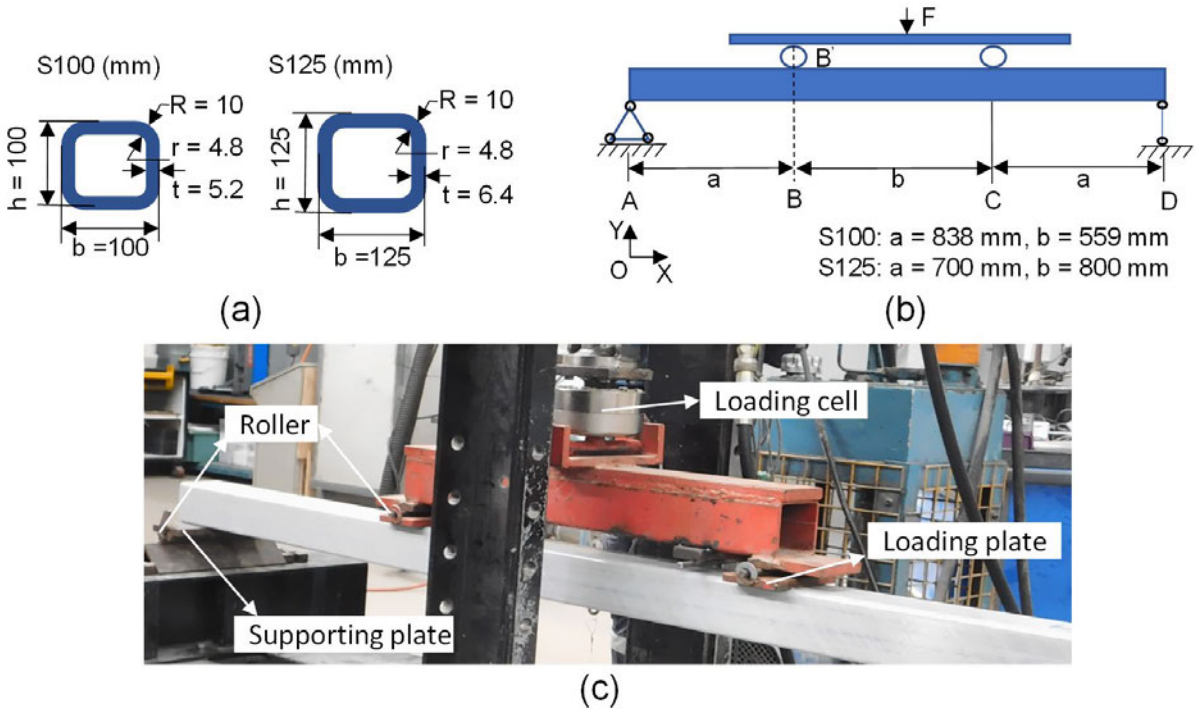

Fig. 2. Flexural test setup; (a) cross-sectional dimensions of S100 and S125, (b) dimensions of four-point bending test for different profiles and (c) four-point bending test configuration.

Table 1. Layup and geometric properties of hollow PFRP profiles.

Profile label	Dimensions (mm)	Layup properties		
		Fibre content (%)	Fibre VF (%)	Stacking sequence
S100	100 × 100 ×5.2	0°: 82.2 50°: 17.8	60.5	0/+50/-50/0/-50/+50/0
S125	125 × 125 × 6.4	0°: 78.1 50°: 21.9	62.5	0/+50/0/-50/0/-50/0/+50/0

As shown in Fig. 1(b), the winder regulates the yarn tension through the position of the yarn path and steel pins. The wound fibre tension was measured using a digital force gauge with a resolution of 0.1 N, resulting in three values of 2.2 N, 15.3 N and 48.3 N. These three yarn tensions corresponded to low, medium and high wound fibre tensions, respectively, and were used to manufacture S125 samples with varying degrees of NUFD. The S100 samples are manufactured at medium tension.

The material properties of the PFRP profiles are shown in Table 2. The selected coupons are free from noticeable fibre waviness across the cross-section, and each group has ten coupon replicates. The material properties will be used to predict the local buckling behaviour of the PFRP profiles, both theoretically and through the FE model.

Table 2. Mechanical properties of the hollow profiles.

Property			Standard	S125		S100	
				Ave.	St.D.	Ave.	St.D.
Compression		Modulus (Gpa)	ASTM D6641	49.1	2.4	50.9	1.5
Tensile	Longitudinal	Modulus (Gpa)	ISO 527-4	43.2	1.1	45.1	1.1
		Poisson's ratio		0.3	0.02	0.32	0.02
	Transverse	Modulus (Gpa)		13.3	0.6	12.3	0.6
In-plane shear		Modulus (Gpa)	ASTM D5379	6.71	0.4	4.70	0.6

The specimens were prepared for microscopic imaging using a Struers LaboPol by grinding and polishing with 1200 and 320 grit papers, followed by a three-step polishing process. The polishing process involved using DiaPro for 9 μm on MD-largo plate, DiaPro for 3 μm on MD-DAC cloth, and OP-U Nondry on Neoprene cloth. The cross-section of the sample was examined and imaged using a Leica DMS300 microscope.

A four-point bending test was conducted on the hollow box PFRP profiles to investigate their flexural behaviour. Two configurations for S125 and S100 with the span-to-depth ratio of 17.6 and 22.35, respectively, were established to observe pure bending behaviour, as shown in Fig. 2(b). It is worth highlighting that this range of span-to-depth ratio was selected to ensure flexural failure which has a lower bound of 16. The loading and supporting plates were equipped with pin-roller steel plates covering 100 mm of the beam length, as shown in Fig. 2(c). Five specimens of each profile were tested with a loading rate of 10 mm/min in accordance with ASTM D7249/D7249M [34]. The deflection of the beam was recorded using a Linear Variable Differential Transducer (LVDT) unit.

3. Material imperfection and its characterisation

A typical NUFD induced during the pull-winding process is shown in Fig. 3. There is an apparent fibre discontinuity of the outermost UD ply on the surface of the PFRP profile in Fig. 3(a), which manufacturers usually reject due to cosmetic and strength concerns. Fig. 3(b) provides multiple views of the cross-sections, each revealing typical defects such as fibre misalignment, in-plane waviness, fibre discontinuity, and out-of-plane waviness. The non-uniform fibre distribution is frequently accompanied by in-plane and out-of-plane waviness of the off-axis ply.

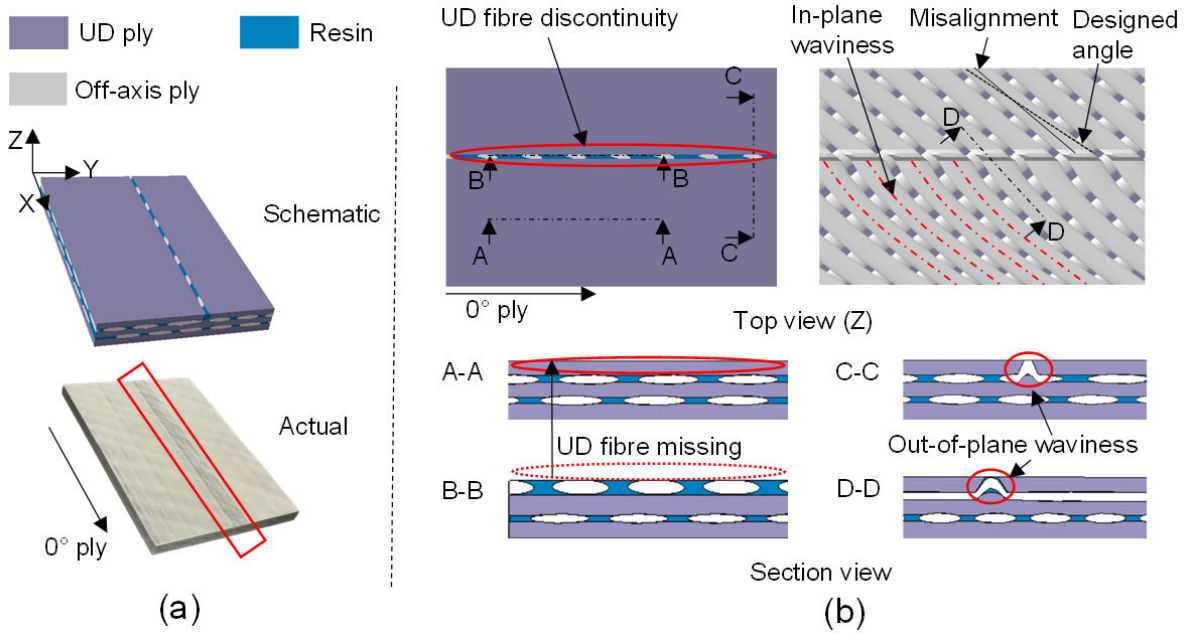

Fig. 3. Schematic of the UD fibre discontinuity; (a) defective sample of the GFRP profile and (b) a description of defects observed in different cutting sections.

3.1. Formation of fibre waviness

The compaction of the off-axis ply in the thickness direction generates excess length, which can cause in-plane waviness, fibre misalignment within the plane, and out-of-plane waviness outside of the plane. The magnitude of the excess length is related to the thickness change, which depends on the initial winding tension during the pull-winding process. Fibre waviness can occur during the preform passage through the entry bush into the pultrusion dies, contributing to the formation of the NUFD.

The Filtered Canny Misalignment Analysis (FCMA) method [30] evaluates the in-plane waviness of off-axis plies based on the image process. The off-axis plies were conducted by partially burning out the hollow composite profile, as shown in Fig. 4(a). This method computes the average local fibre angle relative to the X-axis, as well as the distribution of fibre angles along the Y-axis. According to the localised fibre angle, this ply is divided into three regions: zones A, B, and C. The results in Fig. 4(b) indicate the presence of fibre waviness in zone A, misalignment in zone B, and more severe waviness in zone C. Additionally, the interface between these zones is always accompanied by significant out-of-plane waviness, as indicated by the red square in Fig. 4(a).

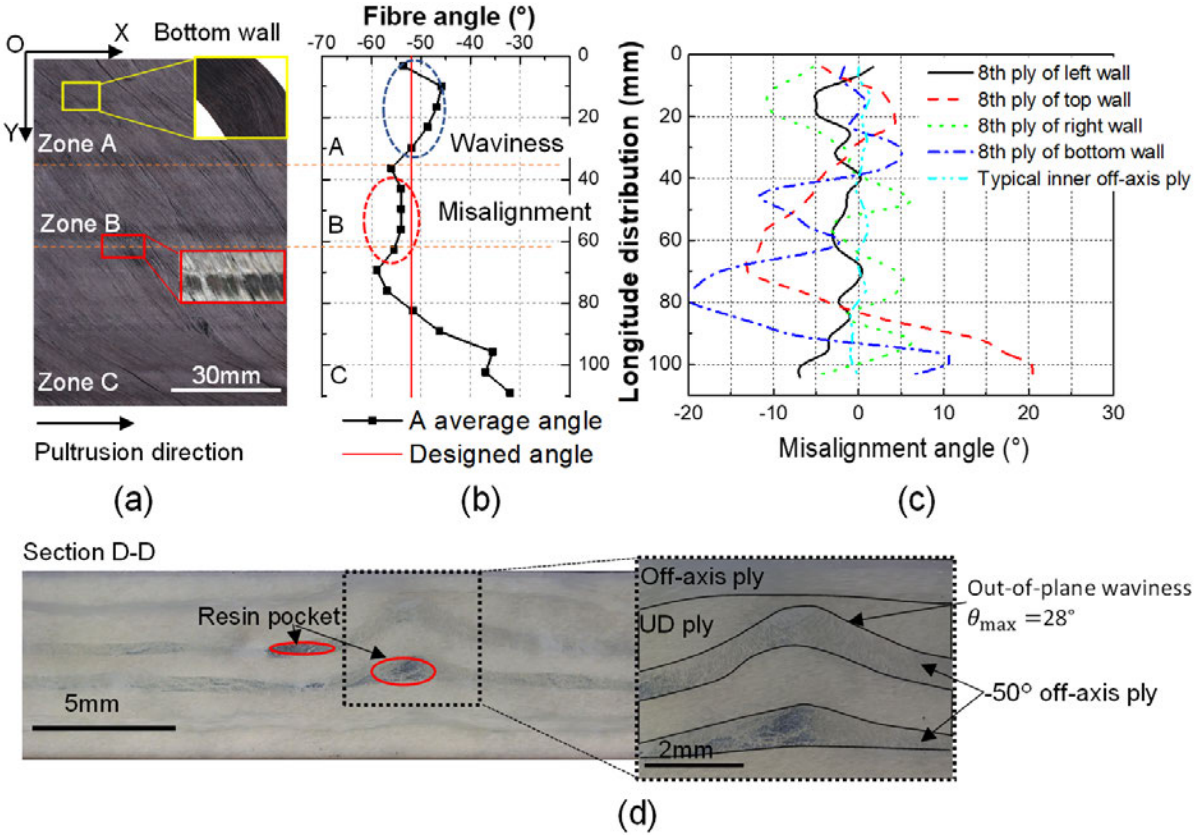

Fig. 4. A typical Fibre waviness in pultruded hollow profiles; (a) scanned image of the off-axis ply, (b) fibre orientation distribution, (c) fibre misalignment angles and (d) out-of-plane waviness of the off-axis ply (+50°).

Fig. 4© compares the misalignment angles of the outermost off-axis ply and a typical inner off-axis ply of a square profile obtained under low winding tension. The results reveal that the outermost ply experiences more significant fibre misalignment, with a maximum angle of around 20°, particularly on walls B and D, where the resin is injected into the pultrusion die. These results suggest that resin flow may contribute to the fibre misalignment.

The wound fibres will interact with UD ply when the out-of-plane waviness occurs. Fig. 4(d) shows a cross-section cut along the +50° direction (similar to section D-D of Fig. 3(b)), which highlights the high level of out-of-plane waviness, with a maximum misalignment reaching 28°. The spaces between the adjacent wound fibres form resin-rich zones. The region with maximum waviness has the outermost UD ply being pushed and split, resulting in discontinuity of UD ply. The absence of the UD ply leads to a reduced local fibre volume fraction in the cross-section, making it more prone to forming a resin-rich zone.

3.2. Discontinuity of UD ply

The NUFD is a result of the lateral movement of UD fibres, which is caused by the shear force between the UD and wound fibres [39]. Fig. 5 presents a comparison of the cross-sectional planes of the standard and defective profiles, taken at sections A-A and B-B (as indicated in Fig. 3(b)). The comparison shows that the outermost UD ply (UD5) is absent in the defective section, as shown in Fig. 5(b). The thickness of the fourth UD ply has decreased by around 70% in the black square of Fig. 5(b). The local fibre volume fraction of the UD fibre decreased in this area. Moreover, the resin is mainly accumulated in the off-axis ply.

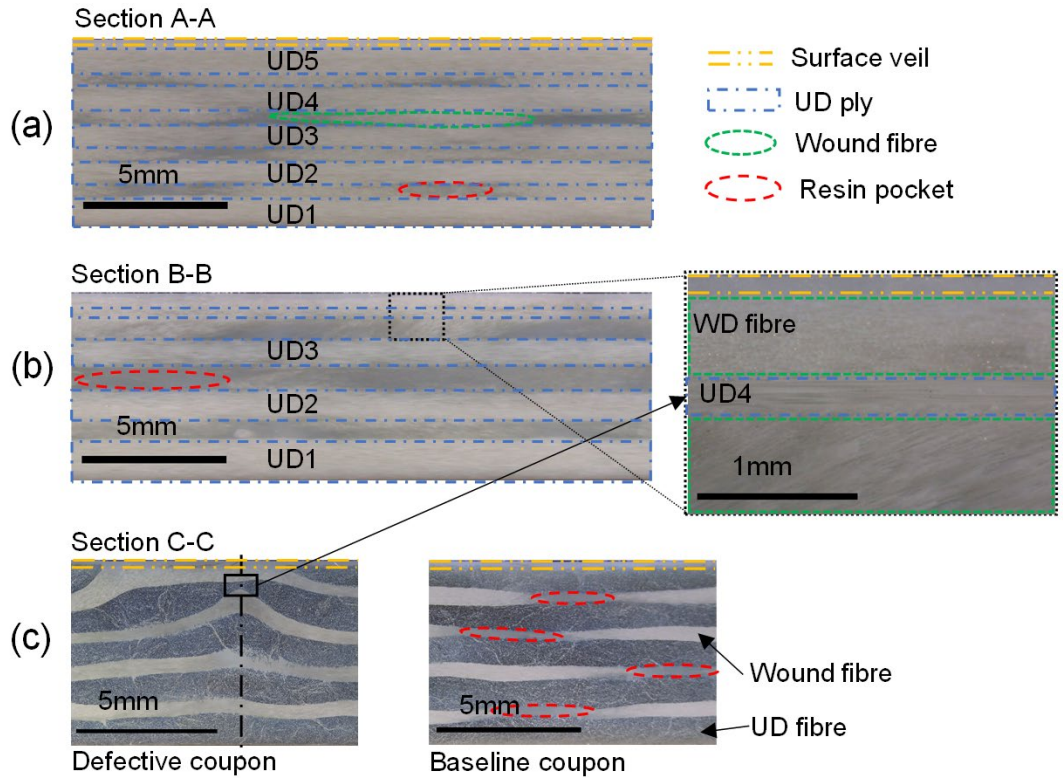

Fig. 5. Characterisation of the typical NUFD at different cutting sections; (a) section A-A, (b) section B-B, and (c) section C-C. The definition of section direction refers to Fig. (3)

Section C-C in Fig. 5© reveals that the off-axis ply in the defective coupon has more fibres and fewer resin-rich areas than the baseline coupon. The difference is primarily attributed to the material excess, which fills the yarn space between the adjacent wound fibres, particularly in the outer ply, where excess length is more prominent than the inner ply.

3.3. Characterisation of the non-uniform fibre distribution

The change in the area of the UD ply along the cross-section was used to characterise the NUFD. As observed in Fig. 5, the resin mainly accumulates in the off-axis ply due to its local lower

volume fraction, which contributes less to the change in the UD ply area. Only the literal movement of the UD fibres causes the area of the UD ply, assuming that the gap between the UD fibres remains stable. Therefore, the area of the UD ply serves the same purpose as the UD fibre volume fraction in describing the NUFD along the cross-section. When the local grid across the section is small (Fig. 6(b)), the local fibre volume fraction can be assessed by Eq. (1).

$$V_i = (1 + \alpha)V_{Basic} \tag{1}$$

where α is the rate of change in the proportion of identified UD ply area compared to the average proportion of UD ply area in the cross-section. V_{Basic} is the average fibre volume fraction of the cross-section.

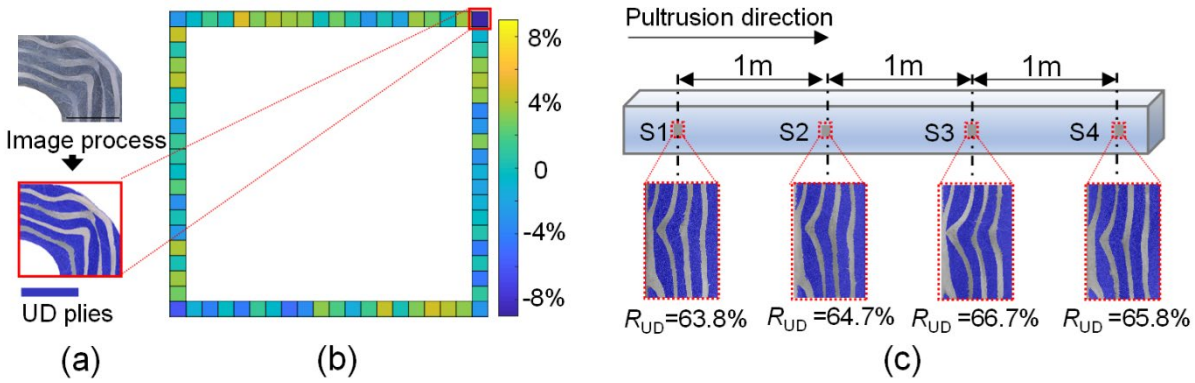

Fig. 6. Measurements of the non-uniform fibre distribution; (a) Segmented UD plies in a single measurement grid, (b) relative V_f deviation of the profile cross-section, and (c) segmented UD plies in the same cross-sectional grid but the different locations along the pultrusion direction.

The pultruded profile's cross-section was ground, polished, and then imaged. Image analysis was performed using MATLAB to identify the UD ply based on the contrast between UD fibre and wound fibres. Fig. 6(a) shows the identified UD fibre ply at the corner, marked in blue, as a measurement grid of the cross-section. Seventy-six evenly spaced locations (grid) along the cross-section were sampled and processed using this methodology. Fig. 6(b) shows the relative deviation of the *i*th UD ply area R_i that is calculated by Eq. (2) across the whole box section.

$$R_i = \frac{S_i - S_A}{S_A} \tag{2}$$

where S_i is the ith area of the identified UD ply; and S_A is the average area of the UD ply. A negative R_i indicates that this region has fewer UD fibres, leading to the NUFD. The positive R_i indicates that the lateral moved UD fibres are filling the yarn space in off-axis plies.

Fig. 6© illustrates the stability of the UD fibre distribution along the pultrusion direction. Four grids of the defective area were observed at one-metre intervals, and the distributions of the UD fibre were shown. Each grid has an identical UD ply area with out-of-plane waviness and UD fibre discontinuity. The UD ply area ratio (R_{UD}) is close to each other, with a standard deviation of 1.3%. Therefore, the defects along the pultrusion direction were uniform.

4. Rotational restraint of the flange support

The contribution of the flange-web junction to the elastic rotational stiffness of flange edge support has been ignored in conventional methods [35]. However, the impact of this junction on the FLB behaviour of FRP sections has been demonstrated in some studies, which showed that a weak junction could lead to premature failure of the entire profile [17, 36]. In this study, the defect that occurs in the flange-web junction will be investigated to assess the influence on the constraint coefficient.

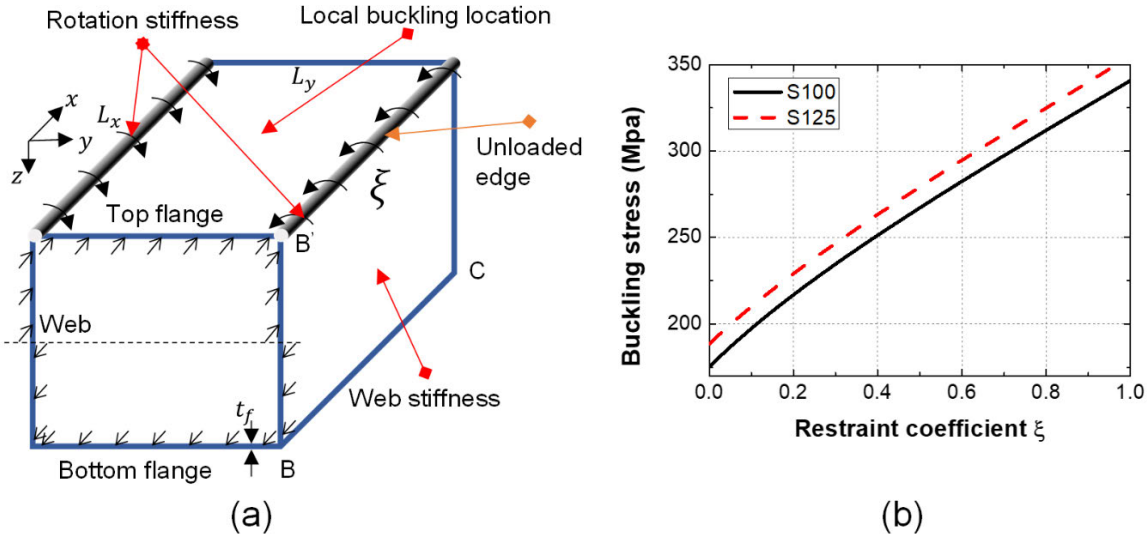

Fig. 7. Elastically restrained plate under the bending test; (a) schematic loading condition of section BC, and (b) the relationship between rotational restraint coefficient and buckling stress.

Fig. 7(a) shows the isolated segment BC (Fig. 2 (b)) of the box section to demonstrate the FLB according to elastic plate theory. When the length of L_x is much larger than L_y, the analytic solution for critical buckling stress can be calculated by Eq. (3) [35].

$$\sigma_{cr} = \frac{\pi^2}{t_f L_y^2}\left[\alpha\sqrt{D_{11}D_{22}} + \beta(D_{12} + 2D_{66})\right] \quad (3)$$

Where D_{ij} is the plate flexural stiffness parameter and can be calculated based on Appendix A and Table 2; t_f is the wall thickness; α and β are dependent on the boundary condition of the edge, which accounts for the rotational stiffness of the flange support. When the long edge of the plate is rotationally restrained, α and β are calculated by Eq. (4) and Eq. (5), respectively.

$$\alpha = 2\sqrt{1 + 4.139\xi} \tag{4}$$

$$\beta = 2 + 0.62\xi^2 \tag{5}$$

Then,

$$\sigma_{cr} = \frac{\pi^2}{t_f L_y^2}\left[2\sqrt{1 + 4.139\xi}\sqrt{D_{11}D_{22}} + (2 + 0.62\xi^2)(D_{12} + 2D_{66})\right] \tag{6}$$

ξ is a parameter that reflects the restrain of the unloaded edge. When $\xi = 0$, the unloaded edge is seen as simply supported. When $\xi = 1$, the unloaded edge is fully clamped. Fig. 7(b) displays the correlation curve between the rotational restraint coefficient and the buckling stress. This curve can be utilised to determine the inverse coefficient when provided with the buckling stress value.

5. Finite element modelling and validation

5.1. Modelling

The material non-linearity due to the inhomogeneous fibre distribution posed a challenge for converging the FE model. To overcome this, Abaqus/Explicit was employed to study the local buckling and post-local buckling behaviour under bending. The loading rate was controlled with a smooth step to increase the accuracy of the simulation, which aimed to replicate the results of a pseudo-static test [37].

The composite profiles were modelled, neglecting the delamination between plies due to the computational cost and accurately matched experimental results [22, 38, 39]. This is because the profiles are confined by continuous inclined fibre plies and closed geometry; hence, the inter-laminar failure analysis in this model was neglected. Transverse shear and tensile damage in the matrix were used to track the delamination propagation [40], and the Hashin damage model was used to simulate the intra-laminar failure. Table 3 lists the strength limits and fracture energy values [41]. The *X*, *Y*, and S refer to the longitudinal, transverse, and shear strength values, respectively, and subscripts *T* and *C* indicate tension and compression, respectively. In the double subscript notation of the fracture energy, the first subscript refers to

the longitudinal or transverse directions, and the second subscript refers to tension or compression.

Table 3. lamina mechanical properties of the hollow box pultruded FRP profiles.

Elastic properties Fibre and matrix		Strength limits (Mpa)		Fracture energy (N/mm)	
E_f (Gpa)	73	X^T	803	G_{LT}	92
G_f (Gpa)	30	X^C	548	G_{LC}	79
υ_f	0.22	Y^T	43	G_{TT}	5
E_m (Gpa)	3.4	Y^C	187	G_{TC}	5
G_m (Gpa)	1.3	S^L	64		
υ_m	0.35	S^T	50		

The simulation employed 8-node quadrilateral in-plane general-purpose continuum shells (SC8R) and used a 5 mm mesh with six elements through the thickness according to the mesh sensitivity study. A rigid body was employed and tied to the beam to simulate the loading plate. The surface between the supporting plate and beam is defined in normal and tangential directions. A friction coefficient of 0.3 was adopted to simulate friction between the beam and the steel plate [42]. The boundary and loading conditions were applied through the reference point of the rigid body, as shown in Fig. 8(a).

The material properties of the composites discussed in Section 3, such as modulus and strength, were not uniform along the cross-section due to the NUFD. The simulation considered this inhomogeneity by defining a coordinate-related fibre volume fraction in the predefined field in Abaqus, as shown in Fig. 8(a). The NUFD along the pultrusion direction is observed to be consistent in Section 4. Therefore, the material properties along the *Z* direction were kept constant. The relationship between the fibre volume fraction and elastic and shear moduli is calculated using the mixture rule [40], which is provided in Appendix B. The fibre and matrix material properties are listed in Table 3 [28, 43].

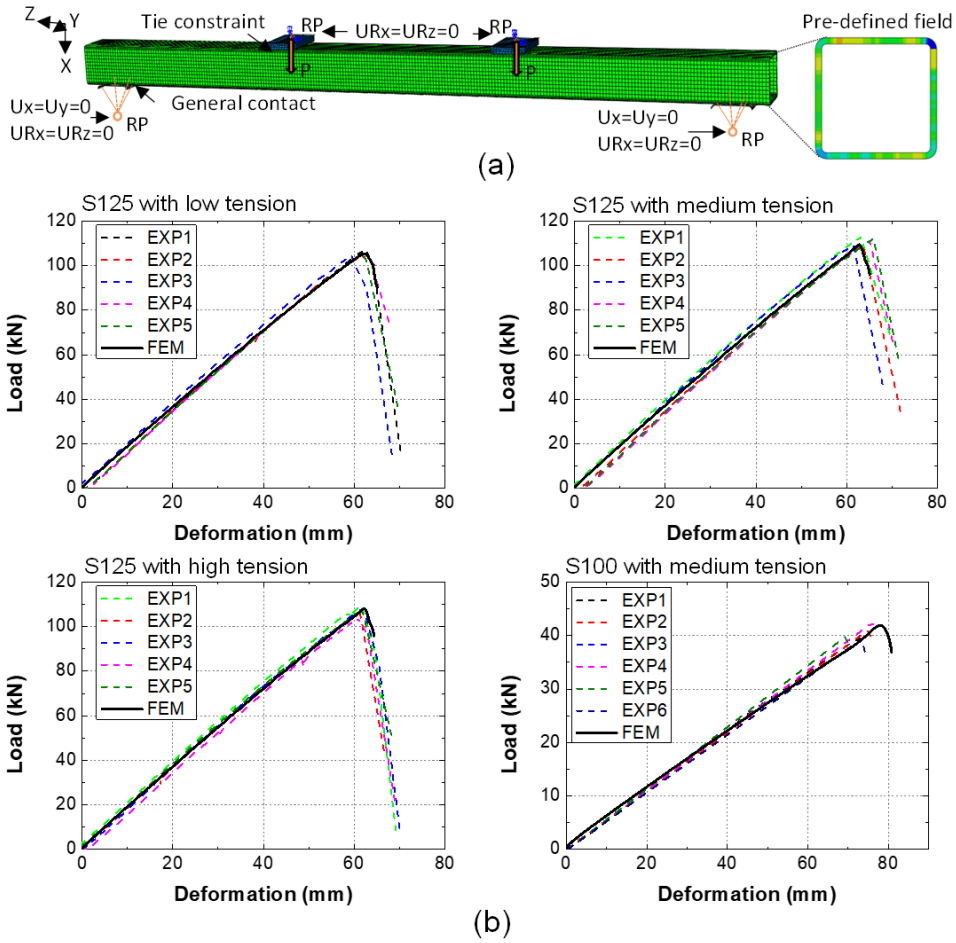

Fig. 8. FE analysis; (a) boundary condition and predefined field of fibre volume fraction, and (b) FE modelling vs experimental load-deflection curves.

5.2. Model verification

The FE model was validated against experimental results, including load-deflection curves and failure modes. The flange of the S125 profile was observed to buckle before the web, as the flange ratio of buckling stress-to-longitudinal modulus $(\sigma_{cr})/(E_L)$ was lower than the web ratio. Both the experiments and FE model confirmed this phenomenon.

The FE model results align with the experimental results, as depicted in Fig. 8(b). The load-deflection curves of S125 and S100 profiles with varying winding tensions are shown, exhibiting linear elastic behaviour until reaching the maximum load. The trend seen in both the slope of the load curve and load capacity supports the use of the changing fibre volume fraction to reflect the mechanical performance change.

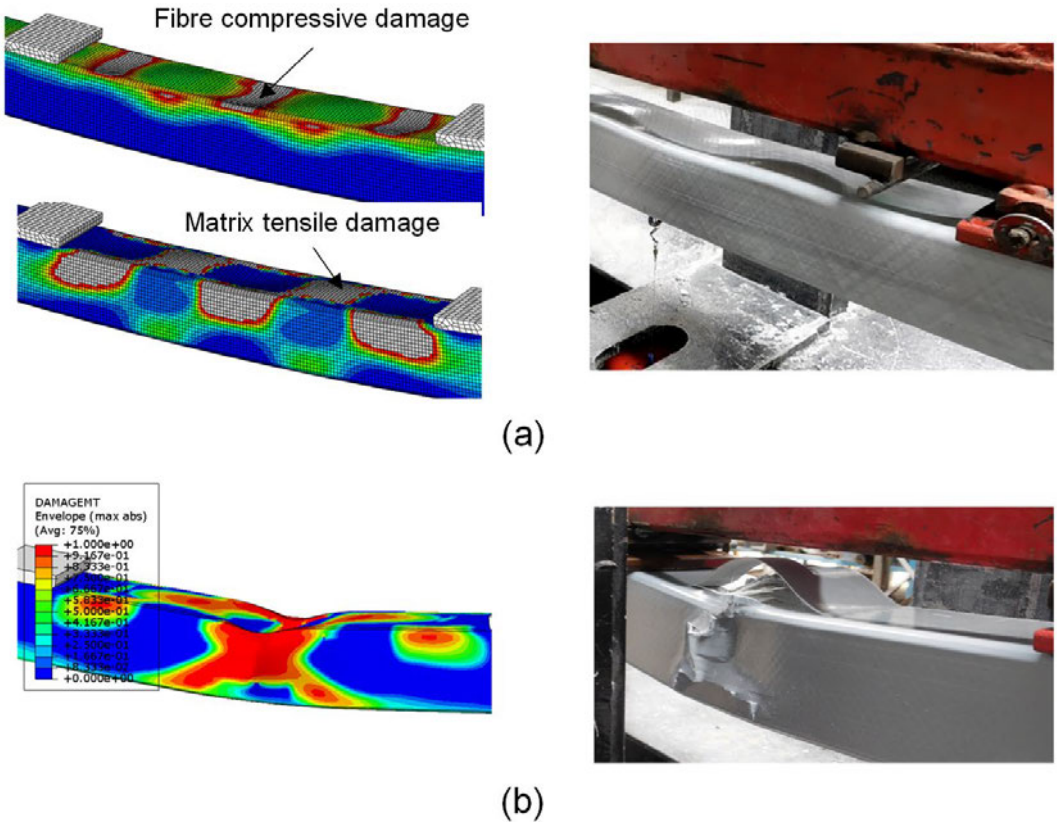

Fig. 9. Numerical vs experimental failure mode of the S125 beam at (a) the ultimate load point and (b) collapse.

The local buckling of the top flange can be seen in the experimental and numerical results at the ultimate load point, as shown in Fig. 9(a). The waviness indicates this local buckling observed before the beam collapses. The numerical result of the localised waviness can be traced by the compressive damage of the fibres and tensile damage of the matrix, which aligns with the experimental result. Afterwards, the fibre damage on the top flange causes the collapse and subsequent spalling and delamination of the top flange and webs. The damage-shear envelope of the FE model (DAMAGEMT) is used to capture the delamination process, as shown in Fig. 9(b). Both the numerical and experimental results indicate that the collapse occurs at the mid-span of the beam.

6. Results and discussion

6.1. Influence of wound fibre tension on NUFD development

The NUFD in the profiles is a result of various winding tension during the pull-winding process. The image analysis results with three different degrees of NUFD are shown in Table 4. The average UD ply ratio *R* of three sets of samples is similar across the whole section, despite the

different winding tensions. This is because the fibre delivery in the pull-winding process (Fig. 1(a)) is consistent among the three samples, meaning they contain the same amount of fibre. Therefore, using the image analysis method to evaluate the variation of the UD fibre volume fraction along the cross-section is reasonable. It can be observed that the ratio of UD fibres at the corner is lower compared to wall fibres, suggesting that the UD fibres at the corner are prone to moving away during compaction.

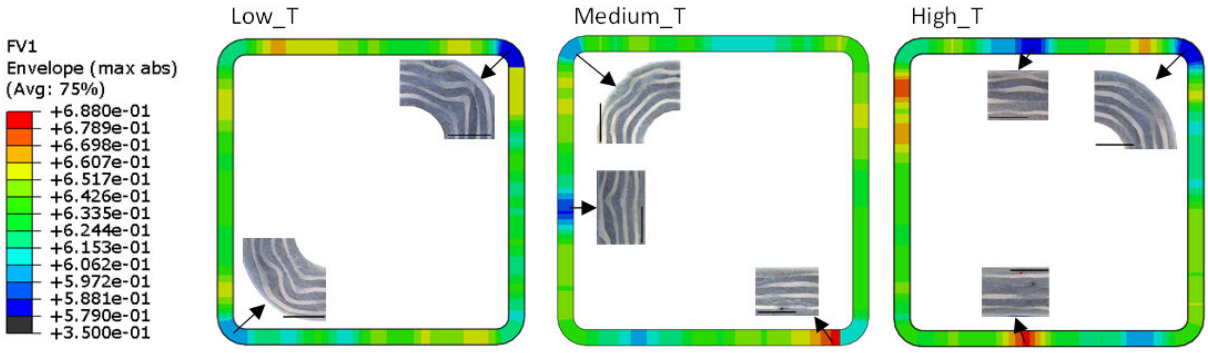

Fig. 10. The fibre volume fraction distribution in the cross-sections of the experimental samples with low, medium, and high winding tension.

Table 4. The ratio of the UD ply area to the profile cross-sectional area.

Samples	Wall (%)		Corner (%)		Whole (%)	Thickness change (mm) (St.D.)
	Average (St.D.)	Maximum deviation	Average (St.D.)	Maximum deviation	Average (St.D.)	
Low	73.3 (2.0)	5.1	69.1 (2.1)	9.1	72.91 (2.32)	3.2 (0.1)
Medium	72.3 (2.3)	7.7	70.7 (2.3)	5.0	72.12 (2.31)	2.5 (0.2)
High	72.3 (2.9)	11.2	70.4 (3.1)	8.6	72.14 (2.97)	2.0 (0.2)

The fibre volume fraction distribution along the cross-section is depicted in Fig. 10, which is calculated based on the change in the UD ply area. The minimum fibre volume fraction occurs at the corners for low and high-tension samples, while it occurs at the web for samples under medium tension. The outermost off-axis ply experiences the most severe out-of-plane waviness, resulting in more server NUFD in the outer UD ply than the inner UD ply. This phenomenon is attributed to the greater excess length generated by the outermost off-axis ply during the pultrusion process. The excess length can be assessed by the thickness change between the dry preform and the final product, as shown in Table 4. When the winding tension is lower, the thickness change is greater. With the movement of UD fibres, the accumulation of neighbour UD fibres results in a high local fibre volume fraction. These results were defined as a field variable in the Abaqus subroutine to reflect changes in mechanical performance.

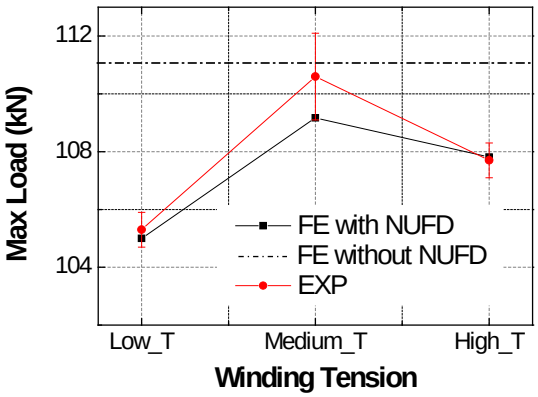

Fig. 11. Comparison of load capacity between FE model and experiment of S125 profiles with different NUFDs.

The ultimate loads with different NUFDs in Fig. 11 demonstrate the ability of the FE model to accurately reflect the impact of NUFD on the mechanical performance of the profiles. The impact of NUFD on the ultimate load of the low-tension sample is around 5%, while the corresponding variation in fibre volume fraction is around 13%. The existence of NUFD results in a decrease in load capacity compared to the FE mode with a homogenous fibre distribution. The medium-tension sample has the least load capacity reduction, as no significant NUFD occurs at the corner, as seen in Fig. 10.

6.2. Rotation stiffness at the corner

The rotational restraint coefficient ξ is a crucial parameter for determining the buckling behaviour of box section beams under axial compression. According to Qiao et al. [44], the analytical solution for ξ can be calculated for box section beams under axial compression. In their study, it was found that ξ equals 0 when the width of flange and web is equal, indicating that buckling occurs simultaneously in the flange and web. However, in the case of S125 and S100 beams used in this research, which have equal widths for the flange and web, the experimental results were found to be closer to the predicted value of $\xi = 1$. This observation is based on the comparison (pred/exp) between the experimental data shown in Table 5. This analytical solution ξ for axial compression can not be applied directly because only the top flange and partial web are under the axial compression in the four-point bending test.

Table 5. The critical buckling stress determined by experiment and analytical prediction.

Label	Exp.	Analytical				Inversed
		$\xi = 0$		$\xi = 1$		
	σ_{cr} (MPa)	σ_{cr}	pred/exp	σ_{cr}	pred/exp	ξ
S125 Low_T	322.6	188.5	0.58	354.7	1.1	0.79
S125 Medium_T	338.8	188.5	0.55	354.7	1.05	0.89
S125 High_T	330.0	188.5	0.57	354.7	1.07	0.83
S100 Medium_T	308.4	175.7	0.57	340.9	1.10	0.78

This research evaluates the effect of NUFD on the rotational restraint coefficient ξ. The exact value of ξ is not determined, but rather a description of the reduction factor is provided when NUFD is introduced. Based on the experiment buckling value, the theoretical value of ξ can be calculated according to Fig. 7(b). The results in Table 5 show that the inverse values of both beams are far from zero, indicating that the unloaded edge L_y is partially constrained instead of simply supported. The constraint coefficient value is influenced by factors such as flange edge support [15], corner geometry [21], and imperfection [17]. This study assessed the effect of imperfection on buckling load by the change of fibre volume fraction.

6.3. Effect of NUFD on different failure modes

The samples of S125 and S100 exhibit FLB as a failure mode. According to previous research [39], increasing the wall thickness of S125 from 6.2 mm to 10 mm will convert the failure mode from FLB to compressive material failure. Fig. 12 illustrates the geometry of the thickened S125 profile and its failure due to the material strength limitation.

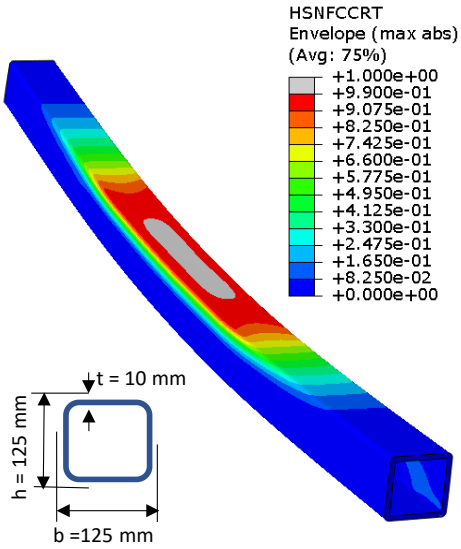

Fig. 12. The cross-sectional geometry of the thickened S125 profile and the compressive material failure mode.

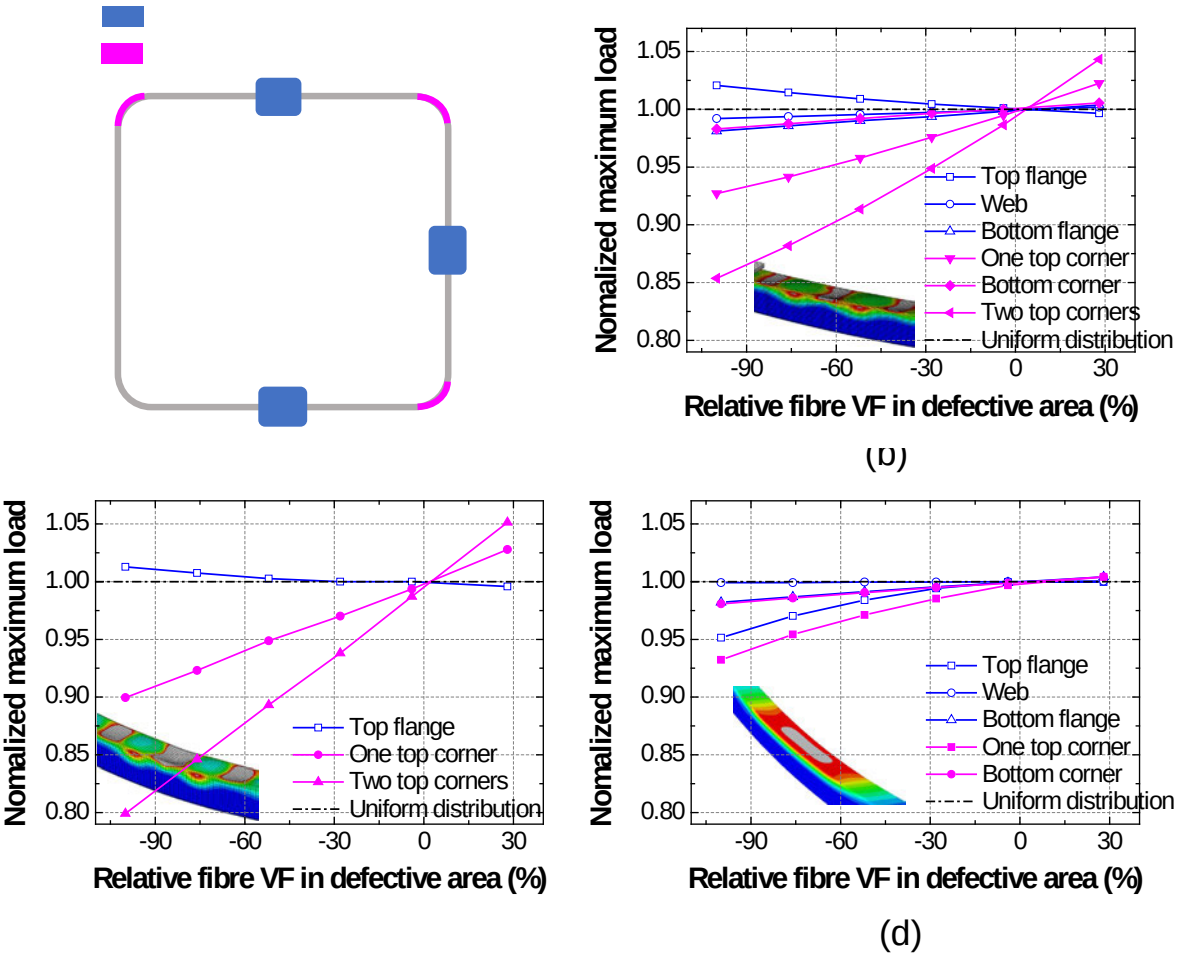

Fig. 13. The influence of local NUFD on the load capacity; (a) NUFD position; (b) effect on S125 beam, (c) S100 beam and (d) thickened S125 beam.

The study quantifies the impact of NUFD on the flexural strength of composite beams using the validated FE model, as discussed in Section 5. Fig. 13(a) shows the defect positions, including the wall and corner defects. The NUFD is represented by the relative decrease in UD fibre volume fraction in the defective area (V_{defect}), as below.

$$R_{Vf} = \frac{V_{defect} - V_{Basic}}{V_{Basic}} \times 100\% \tag{7}$$

where V_{Basic} is the basic fibre volume fraction of 0.625. The normalised maximum load for the hollow profiles with NUFD is calculated based on the maximum load obtained from a profile with uniform material ($R_{Vf} = 0$). A value of -100% for R_{Vf} indicates the complete absence of UD fibres in the defective area replaced by resin, while the wound fibres remain unchanged. The width of the wall defect area is 10 mm and has the same area as the corner defects. These defects are analysed separately, and all other areas are assumed to be uniform.

The result of the FE model, as shown in Fig. 13(b), demonstrates the influence of NUFD on the ultimate load of the S125 beam. The NUFD only affected the ultimate load without any change in the failure mode by FLB. Considering the worst-case scenario, when the fibre volume fraction decreases by 100%, the impact of flange and web defects is small, within 3%. However, the ultimate load decreases by 8% and 14%, respectively, when there are one and two top-corner defects. The difference highlights the contribution of top-corner defects to local buckling, as the NUFD at corners has a negative effect on the rotational restraint coefficient.

The results are similar for the S100 samples, with the corner defects having a greater impact on the ultimate load by a maximum 20% reduction compared to the top flange defects, as they exhibit the same failure mode, as shown in Fig. 13(c). The load capacity of S100 and S125 samples decreases linearly with the relative decrease in corner fibre volume fraction.

In order to examine the impact of NUFD on compressive material failure mode, the thickness of the S125 profile is increased to 10 mm, and the resulting structure is named 'thickened S125 beam'. The thickened S125 profile experiences a compressive material failure in the top flange due to the material strength limitation and reduced tendency to buckle. The load capacity of the thickened S125 beam with top corner and flange defects shows a decrease, which has a similar magnitude of decline with R_{Vf}, as shown in Fig. 13(d). The top flange performs differently from the basic S125 beam. The web and bottom NUFDs do not significantly affect load capacity as the basic S125 beam. Furthermore, when the fibre volume fraction at the corner increases ($R_{Vf} > 0$), the improvement in strength for compressive failure mode is 0.4%, while for local FLB mode, it is 3.1%. This improvement is due to an increase in the restraint coefficient for FLB. By comparing the effect of NUFD on different failure modes, it can be seen that local buckling is more sensitive to NUFD. This finding explains why non-uniform fibre packing over cross-section has a limited effect on compressive material strength [27].

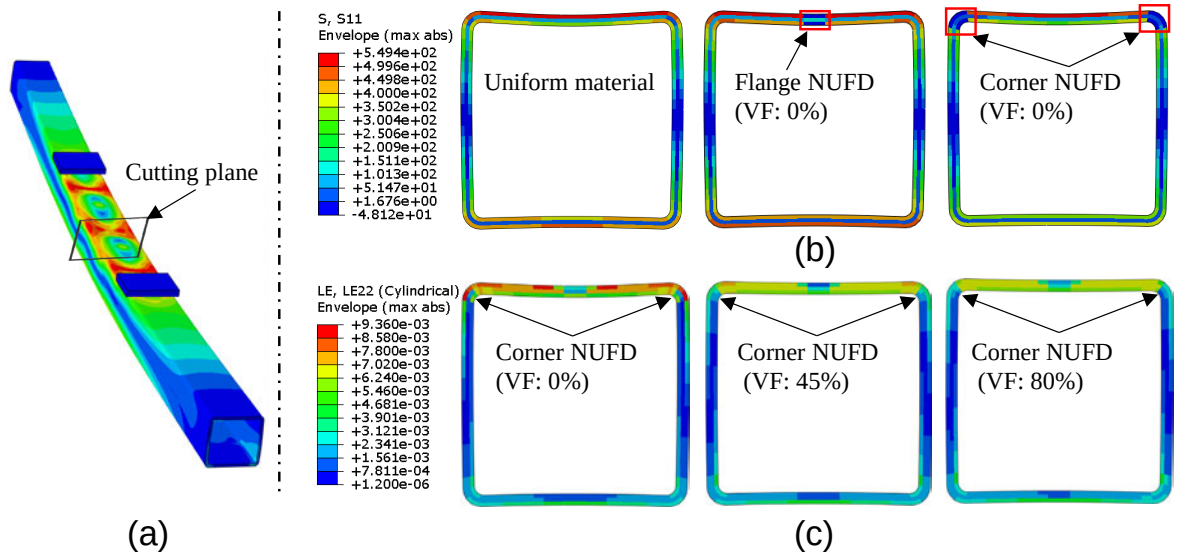

Fig. 14. The influence of local NUFD on the stress and strain of the S125 beam; (a) the position of the cutting plane, (b) stress comparison at different NUFD locations, and (c) strain distribution under the same loading displacement.

The axial stress distribution in the middle plane of the S125 beam, at 97% of the ultimate load (just before failure), is presented in Fig. 14(b). The presence of NUFD affects stress distribution. When the fibre volume fraction decreases in a defective area, the stress is lower in defective areas than in the uniform material beam. However, a top flange defect with a low fibre volume fraction causes a reduction in bending stiffness and moment, while a corner defect reduces the rotation stiffness. These factors contribute to a higher buckling load in the former case and a lower buckling load in the latter case, as demonstrated in Fig. 13(b) and Fig. 13(c).

Fig. 14(c) shows the change in logarithmic strain with the fibre volume fraction at the corner in the tangential direction of the cylindrical coordinate at the same loading displacement point. As the corner fibre volume fraction increases, the strain of the top flange decreases due to the growing rotational stiffness, which can obtain higher local buckling capacity. Therefore, avoiding a lower volume fraction at the corner is recommended to obtain a higher load capacity. Alternatively, the corner area can be increased to enhance the load capacity [45].

6.4. Rotational stiffness reduction factor for NUFD at corners

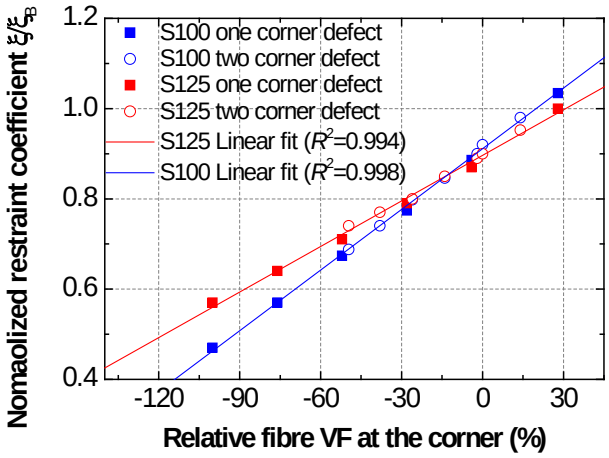

Fig. 15. The influence of corner NUFD on the rotational restraint coefficient of the S100 and S125 beams

The results of the ultimate load of the S125 and S100 beams obtained from the FE model can be transformed into rotational restraint coefficients (Fig. 7(b)). The normalised restraint coefficient is the ratio of the calculated coefficient from the non-uniform model and the uniform model, which can represent the resistance reduction factor. This relationship is presented in Fig. 15, where a linear correlation can be observed between the corner fibre volume fraction and the rotational restraint coefficient for both profiles.

A linear regression analysis was carried out on the S100 and S125 data to determine their slope and intercept values, as shown in Fig. 15. The slope represents the sensitivity of the hollow structure to the corner NUFD, while the intercept represents the rotational restraint coefficient when the corner material is uniform ($R_{Vf} = 0$). The analysis revealed that the S100 beam has a higher slope (0.44) than the S125 beam (0.34), primarily due to its higher UD fibre content ratio (Table 1). Moreover, the intercept values for both profiles are similar, 0.91 for S100 and 0.90 for S125, indicating that the two different profiles have the same rotational restraint coefficient in a uniform material, despite their different layups and geometries. For reference, a decrease of 30% in the corner fibre volume fraction results in an approximate reduction of 21% of the rotational restraint coefficient for both profiles. This regression model can be utilised during the early stages of material design evaluation and manufacturing quality control.

7. Conclusion

This study aims to investigate the impact of non-uniform fibre distributions (NUFD) on the load capacity of box-section composite profiles under bending, with a focus on the flange local buckling (FLB) failure mode and compressive material failure. The samples manufactured by

using different winding tensions exhibit a 9% NUFD deviation at the corner. Based on the classic plate theory, the study highlights that the rotational restraint coefficient under bending differs from that under axial compression. The rotational restraint coefficient for a square hollow profile during bending is close to 1.0, unlike the established value in literature, which is close to 0 during axial compression [44]. This difference is because not all flanges and webs are under axial compression during the four-point bending test. The results show the significance of considering this difference in the design-for-manufacturing stage.

The samples with different NUFDs were manufactured using different winding tensions, resulting in a 5% variance in load capacity. To better comprehend how NUFD influence the local buckling capacity, NUFD modelling was implemented by changing the fibre volume fraction along the cross-section and considering it as an input in the FE model. The model with NUFD more accurately predicts the local buckling load compared to the uniform material model. A parametric study was then conducted to analyse the effect of the NUFD location on the buckling load. Results indicate that corner NUFD decreases the FLB capacity by up to 20%, while flange NUFD increases it slightly by up to 3% in cases where the UD ply within the defective area is filled with resin. This reduction in load capacity is attributed to the decreased rotational restraint coefficient at the corner. Conversely, the effect of NUFD location across the section was found insignificant in beams dominated by a compressive failure of fibre, at which the ultimate material strength is reached without buckling instability

The decrease in local buckling load was proportional to the relative decrease in fibre volume fraction at the corner, as indicated by the regression model. This model can be used in the early stages of material design evaluation to estimate the effect of the NUFD on the flexural behaviour of hollow box PFRP beams. Numerical results from the S100 and S125 profiles indicate that the linear trend observed in the regression model is independent of profile geometry and fibre layup. Additionally, when the fibre volume fraction at the corner is reduced by 30%, it leads to an approximate 21% decrease in the rotational restraint coefficient for both profiles. This finding can be used as a reference for evaluating the effects of material imperfection. Considering the NUFD at the corner, it was concluded that using $\xi = 0$ (as established by EUR 27666 [46]) is a conservative prediction.

Further investigation would be required to incorporate the rotational restraint coefficient and its relationship with the associated NUFD in the laminated classical theory. This will provide

an accurate characterisation of PFRP profiles and their manufacturing defects, which will be helpful to the design of hollow PFRP profiles.

Acknowledgements

The work was funded through a Cooperative Research Centres Projects (CRC-P) Grant (CRCPSIX000117).

Appendix A. Plate flexural stiffness parameters

$$D_{11} = \frac{E_L t^3}{12(1-\upsilon_{12}.\upsilon_{21})} \quad \text{(A.1)}$$

$$D_{22} = \frac{E_T t^3}{12(1-\upsilon_{12}.\upsilon_{21})} \quad \text{(A.2)}$$

$$D_{12} = \upsilon_{12} D_{12} \quad \text{(A.3)}$$

$$D_{66} = \frac{G t^3}{12} \quad \text{(A.4)}$$

E_L : Longitudinal modulus of elasticity

E_T : Transverse modulus of elasticity

G : Shear modulus

t : Thickness

υ_{ij} : Poisson's ratio

Appendix B. The rule of the mixture of fibre and matrix

$$E_{11} = V_f E_f + (1 - V_f) E_m \quad \text{(B.1)}$$

$$E_{22} = \frac{E_f E_m [V_f + \eta_2 (1 - V_f)]}{E_m V_f + E_f \eta_2 (1 - V_f)} \quad \text{(B.2)}$$

$$\upsilon_{12} = \upsilon_f V_f + (1 - V_f) \upsilon_m \quad \text{(B.3)}$$

$$G_{12} = G_m \left(\frac{(1+V_f) G_f + (1-V_f) G_m}{(1-V_f) G_f + (1+V_f) G_m} \right) \quad \text{(B.4)}$$

$$G_{23} = G_m \left(\frac{V_f + (1-V_f)\eta_4}{\eta_4 (1-V_f) + V_f G_m / G_f} \right) \quad \text{(B.5)}$$

$$\eta_2 = \frac{0.2}{1-\upsilon_m} \left(1.1 - \sqrt{\frac{E_m}{E_f}} + \frac{3.5 E_m}{E_f} \right) (1 + 0.22 V_f) \quad \text{(B.6)}$$

$$\eta_4 = \frac{3 - 4\upsilon_m + G_m / G_f}{4(1-\upsilon_m)} \quad \text{(B.7)}$$

E_{11} : modulus of elasticity in the fibre direction

E_{22} : modulus of elasticity in the direction transverse to fibres

G_{12} : in-plane shear modulus

G_{23} : out-of-plane shear modulus

υ_{12} : in-plane Poisson's ratio

V_f : fibre volume fraction

E_f : Young's elastic modulus of the fibre

G_f : Shear elastic modulus of the fibre

υ_f : Poisson's ratio of the fibre

υ_m : Poisson's ratio of the matrix

E_m : Young's elastic modulus of the matrix

G_m : Shear elastic modulus of the matrix

References

[1] Guades E, Aravinthan T, Islam M, Manalo A. A review on the driving performance of FRP composite piles. Composite Structures. 2012;94:1932-42.
[2] Uddin N. Developments in fiber-reinforced polymer (FRP) composites for civil engineering: Elsevier, 2013.
[3] Gand AK, Chan T-M, Mottram JT. Civil and structural engineering applications, recent trends, research and developments on pultruded fiber reinforced polymer closed sections: a review. Frontiers of Structural and Civil Engineering. 2013;7:227-44.
[4] Fangueiro R. Fibrous and composite materials for civil engineering applications: Elsevier, 2011.
[5] Madenci E, Onuralp Özkılıç Y, Gemi L. Buckling and free vibration analyses of pultruded GFRP laminated composites: Experimental, numerical and analytical investigations. Composite Structures. 2020;254.
[6] Debski H, Rozylo P, Teter A. Buckling and limit states of thin-walled composite columns under eccentric load. Thin-Walled Structures. 2020;149.
[7] Czapski P, Lunt AJG. The influence of manufacturing on the buckling performance of thin-walled, channel-section CFRP profiles—An experimental and numerical study. Thin-Walled Structures. 2023;184:110475.
[8] Ascione L, Berardi VP, Giordano A, Spadea S. Pre-buckling imperfection sensitivity of pultruded FRP profiles. Composites Part B: Engineering. 2015;72:206-12.
[9] Matthews FL, Davies G, Hitchings D, Soutis C. Finite element modelling of composite materials and structures: Elsevier, 2000.
[10] Cardoso DCT, Harries KA, Batista EdM. Compressive strength equation for GFRP square tube columns. Composites Part B: Engineering. 2014;59:1-11.
[11] Kollár L, Springer G. Thin Plates. In: Springer GS, Kollár LP, editors. Mechanics of Composite Structures. Cambridge: Cambridge University Press; 2003. p. 89-168.
[12] Arani AG, Maghamikia S, Mohammadimehr M, Arefmanesh A. Buckling analysis of laminated composite rectangular plates reinforced by SWCNTs using analytical and finite element methods. Journal of Mechanical Science and Technology. 2011;25:809-20.
[13] Cardoso DCT, Harries KA, Batista EdM. Closed-form equations for compressive local buckling of pultruded thin-walled sections. Thin-Walled Structures. 2014;79:16-22.

[14] Qiao P, Davalos JF, Wang J. Local buckling of composite FRP shapes by discrete plate analysis. Journal of Structural Engineering. 2001;127:245-55.
[15] Kollár LP. Local buckling of fiber reinforced plastic composite structural members with open and closed cross sections. Journal of Structural Engineering. 2003;129:1503-13.
[16] Ascione L, Caron J-F, Godonou P, van IJselmuijden K, Knippers J, Mottram T, et al. Prospect for new guidance in the design of FRP: Support to the implementation, harmonization and further development of the Eurocodes: Publications Office of the European Union, 2016.
[17] Liu T, Harries KA. Flange local buckling of pultruded GFRP box beams. Composite Structures. 2018;189:463-72.
[18] Baran I. Pultrusion: state-of-the-art process models: Smithers Rapra, 2015.
[19] Ramôa Correia J. 9 - Pultrusion of advanced fibre-reinforced polymer (FRP) composites. In: Bai J, editor. Advanced Fibre-Reinforced Polymer (FRP) Composites for Structural Applications: Woodhead Publishing; 2013. p. 207-51.
[20] Alajarmeh O, Zeng X, Aravinthan T, Shelley T, Alhawamdeh M, Mohammed A, et al. Compressive behaviour of hollow box pultruded FRP columns with continuous-wound fibres. Thin-Walled Structures. 2021;168:108300.
[21] Alhawamdeh M, Alajarmeh O, Aravinthan T, Shelley T, Schubel P, Mohammed A, et al. Review on local buckling of hollow box FRP profiles in civil structural applications. Polymers (Basel). 2021;13.
[22] Alhawamdeh M, Alajarmeh O, Aravinthan T, Shelley T, Schubel P, Kemp M, et al. Modelling hollow pultruded FRP profiles under axial compression: Local buckling and progressive failure. Composite Structures. 2021;262.
[23] Lightfoot JS, Wisnom MR, Potter K. A new mechanism for the formation of ply wrinkles due to shear between plies. Composites Part A: Applied Science and Manufacturing. 2013;49:139-47.
[24] Roy SS, Zou W, Potluri P. Influence of braid carrier tension on carbon fibre braided preforms. In: Kyosev Y, editor. Recent Developments in Braiding and Narrow Weaving. Cham: Springer International Publishing; 2016. p. 91-102.
[25] Kyosev Y. Advances in braiding technology: Specialized techniques and applications: Woodhead Publishing, 2016.
[26] GB/T 31539. Pultruded fiber reinforced polymer composites structural profiles. Standardization Administration of China. 2015 [in Chinese].
[27] Zhang L, Zhang S, Xu D, Chen X. Compressive behavior of unidirectional FRP with spacial fibre waviness and non-uniform fibre packing. Composite Structures. 2019;224:111082.
[28] Feng P, Wu Y, Liu T. Non-uniform fiber-resin distributions of pultruded GFRP profiles. Composites Part B: Engineering. 2021.
[29] Wilhelmsson D, Gutkin R, Edgren F, Asp LE. An experimental study of fibre waviness and its effects on compressive properties of unidirectional NCF composites. Composites Part A: Applied Science and Manufacturing. 2018;107:665-74.
[30] Qi S, Alajarmeh O, Shelley T, Schubel P, Rendle-Short K, Zeng X. Fibre waviness characterisation and modelling by Filtered Canny Misalignment Analysis (FCMA). Composite Structures. 2023;307:116666.
[31] Poulton M, Sebastian W. Taxonomy of fibre mat misalignments in pultruded GFRP bridge decks. Composites Part A: Applied Science and Manufacturing. 2021;142.
[32] Baran I, Straumit I, Shishkina O, Lomov SV. X-ray computed tomography characterization of manufacturing induced defects in a glass/polyester pultruded profile. Composite Structures. 2018;195:74-82.
[33] Netzel C, Mordasini A, Schubert J, Allen T, Battley M, Hickey CMD, et al. An experimental study of defect evolution in corners by autoclave processing of prepreg material. Composites Part A: Applied Science and Manufacturing. 2021;144.

[34] ASTM D7249/D7249M. Standard test method for facing properties of sandwich constructions by long beam flexure. Am Soc Test Mater. 2012.
[35] Kollar LP, Springer GS. Mechanics of composite structures: Cambridge university press, 2003.
[36] Feo L, Mosallam AS, Penna R. Mechanical behavior of web–flange junctions of thin-walled pultruded I-profiles: An experimental and numerical evaluation. Composites Part B: Engineering. 2013;48:18-39.
[37] Huang Z, Li D, Uy B, Thai H-T, Hou C. Local and post-local buckling of fabricated high-strength steel and composite columns. Journal of Constructional Steel Research. 2019;154:235-49.
[38] Al-saadi AU, Aravinthan T, Lokuge W. Effects of fibre orientation and layup on the mechanical properties of the pultruded glass fibre reinforced polymer tubes. Engineering Structures. 2019;198.
[39] Alhawamdeh M, Alajarmeh O, Aravinthan T, Shelley T, Schubel P, Mohammad A, et al. Modelling flexural performance of hollow pultruded FRP profiles. Composite Structures. 2021;276.
[40] Barbero EJ. Introduction to composite materials design: CRC Press, 2010.
[41] Sharma AP, Khan SH, Parameswaran V. Experimental and numerical investigation on the uni-axial tensile response and failure of fiber metal laminates. Composites Part B: Engineering. 2017;125:259-74.
[42] Van Paepegem W, De Geyter K, Vanhooymissen P, Degrieck J. Effect of friction on the hysteresis loops from three-point bending fatigue tests of fibre-reinforced composites. Composite Structures. 2006;72:212-7.
[43] Huang W, Causse P, Hu H, Belouettar S, Trochu F. Transverse compaction of 2D glass woven fabrics based on material twins - Part I: Geometric analysis. Composite Structures. 2020;237:10.
[44] Qiao P, Shan L. Explicit local buckling analysis and design of fiber–reinforced plastic composite structural shapes. Composite Structures. 2005;70:468-83.
[45] Alhawamdeh M, Alajarmeh O, Aravinthan T, Shelley T, Schubel P, Mohammed A, et al. Design optimisation of hollow box pultruded FRP profiles using mixed integer constrained Genetic algorithm. Composite Structures. 2022;302:116247.
[46] Ascione L, Caron J-F, Godonou P, van IJselmuijden K, Knippers J, Mottram T, et al. Prospect for new guidance in the design of FRP. Ispra: EC Joint Research Centre. 2016.

Chapter 6: Numerical Simulation and Experimental Investigation of the Braiding-pultrusion Process for Manufacturing Braided Composite Profiles

6.1. Introduction

In Chapter 6, the study develops a pull-braiding production line in the laboratory based on the advancement of pull-winding technology. A numerical simulation and experimental investigation of the pull-braiding process for manufacturing braided composite profiles are conducted. The developed numerical model accurately simulates the braiding process and predicts the geometrical features of the braided structures. The study identifies defects in composite profiles, such as non-uniform wall thickness, resin-rich area, and dry preform, providing a foundation for future research in the development of advanced composite materials with tailored mechanical properties.

6.2. Links and implications

The primary goal of this chapter is to create prototype composite profiles using this novel manufacturing technique. However, there are still several aspects of the process that require improvement, such as the presence of dry fibres in the product, non-uniform wall thickness, and other defects. The links and implications of Chapter 6's findings, focusing on the pull-braiding process and its outcomes, connect with other chapters in the thesis to provide a comprehensive understanding of the influence of manufacturing techniques on the properties and performance of hollow box FRP structures. The pull-braiding production line developed in this chapter can be further optimized by refining processing parameters, such as resin impregnation and fibre tension control. This would lead to improved product quality and reduced manufacturing-induced defects. Comparing the mechanical performance of pull-braiding products with those from the pull-winding process can highlight the advantages and disadvantages of each technique. Furthermore, this comparison can provide valuable insights for future research and development of advanced composite materials and manufacturing processes. By integrating the findings from other chapters, such as the impact of fibre waviness and Non-Uniform Fibre Distribution (NUFD), this work lays the foundation for a more in-depth understanding of the complex relationship between manufacturing-induced defects, material properties, and structural performance of FRP composites.

Chapter 6: Numerical Simulation and Experimental Investigation of the Braiding-pultrusion Process for Manufacturing Braided Composite Profiles

6.1. Introduction

In this study, a comprehensive investigation into the manufacturing of braided composite profiles using the pull-braiding and closed injection pultrusion process is presented. A bi-axial braiding technique is employed to produce preforms with balanced mechanical properties in two primary directions. The manufacturing process consists of preparing braiding bobbins, braiding the dry preform, pultrusion, and post-processing. A numerical model is developed to simulate the braiding process and predict the geometrical features of the braided structures. The model's accuracy is validated through comparison with experimental data, with results showing good agreement in terms of fibre paths and braiding angles. The study also investigates the observed defects in the composite profiles, such as resin-rich areas and dry preform. This research contributes to the understanding of the pull-braiding processes for manufacturing braided composite profiles and provides a solid foundation for future research in the development of advanced composite materials with tailored mechanical properties.

The primary goal of this chapter is to create prototype composite profiles using the pull-braiding manufacturing technique. However, there are still several aspects of the process that require improvement, such as the presence of dry fibres in the product, non-uniform wall thickness, and other defects (as this manufacturing trial was on a lab scale not a commercial production scale similar to the specimens used in previous chapters). The links and implications of Chapter 6's findings, focusing on the pull-braiding process and its outcomes, connect with other chapters in the thesis to provide a comprehensive understanding of the influence of manufacturing techniques on the properties and performance of hollow box FRP structures. The pull-braiding production line developed in this chapter can be further optimised by refining processing parameters, such as resin impregnation and fibre tension control. This would lead to improve product quality and reduce manufacturing-induced defects. Comparing the mechanical performance of pull-braiding products with those from the pull-winding process can highlight the advantages and disadvantages of each technique.

The pull-braiding process combines a braiding machine and a pultrusion system to produce preforms with continuous fibres and controlled geometrical features, as shown in Figure 6.1. The pultrusion system is aligned with the braiding machine, allowing the braided

preform to be pulled directly into the heated die for curing. The first stage generates the dry braided preform, while the second stage involves resin infusion, curing and cutting. In the pull-braiding system, the preform is gripped by the pullers, and the mandrel is fixed, which differs from the traditional braiding process.

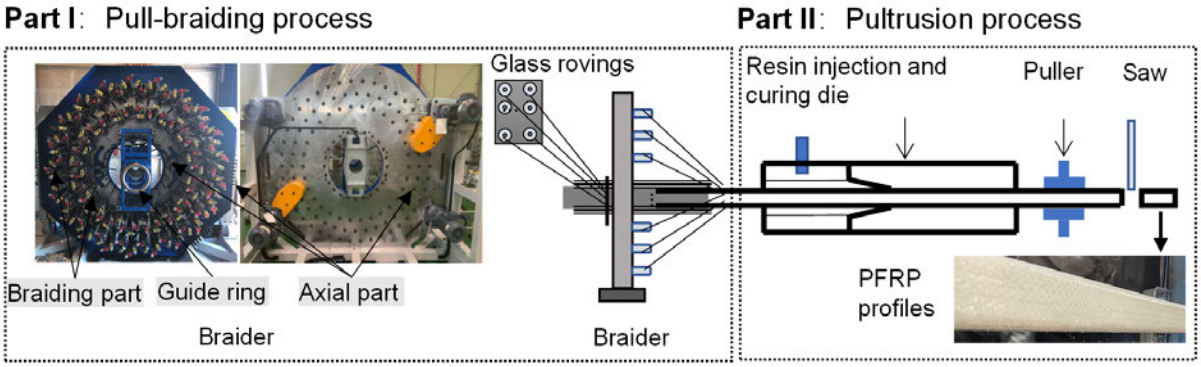

Figure 6.1. Illustration of the pull-braiding process

Braiding process simulation includes analytical and numerical predictions. Analytical methods have limitations with complex mandrel geometry and physical interactions due to the assumptions and approximations (Du & Popper, 1994; Guyader, Gabor, & Hamelin, 2013; Kessels & Akkerman, 2002). Although the FEM methods require significant computational time because of the large constructed models employed and small element size, the simulation results, considering the details such as friction and yarn cross-section, closely resemble the real counterpart (Hans, Cichosz, Brand, & Hinterhölzl, 2015; Pickett, Sirtautas, & Erber, 2009; Sun et al., 2018).

In this research, the study involved producing the braided dry preform numerically and experimentally to develop a comprehensive understanding of the pull-braiding process and its influence on the properties of the braided structures. The objectives of this research are as follows:

1. To investigate the pull-braiding process experimentally, focusing on the preparation of the braiding bobbin, bi-axial braiding, and the pultrusion process.

2. To develop a numerical model for simulating the braiding process and predicting the geometrical features of the braided structures.

3. To validate the numerical model against experimental data and optimise the process parameters for achieving desired preform geometries and properties.

6.2. Experiment setup

6.2.1. Preparation for the braiding bobbin

The braiding bobbin is a critical component in the pull-braiding process, as it holds the fibre tows and supplies them at a controlled rate during the braiding operation. In this study, the bobbins were loaded with ECR-glass fibres (4400 tex). Rewinding glass fibre from raw fibre roving to the braiding bobbin is critical for overall process stability, supplying the material in the braiding machine. The rewinding equipment is shown in Figure 6.2(a), provided by the T4L. Fibre material from the raw roving is pulled off through the guide and winding sensor and then wound onto the braiding bobbin.

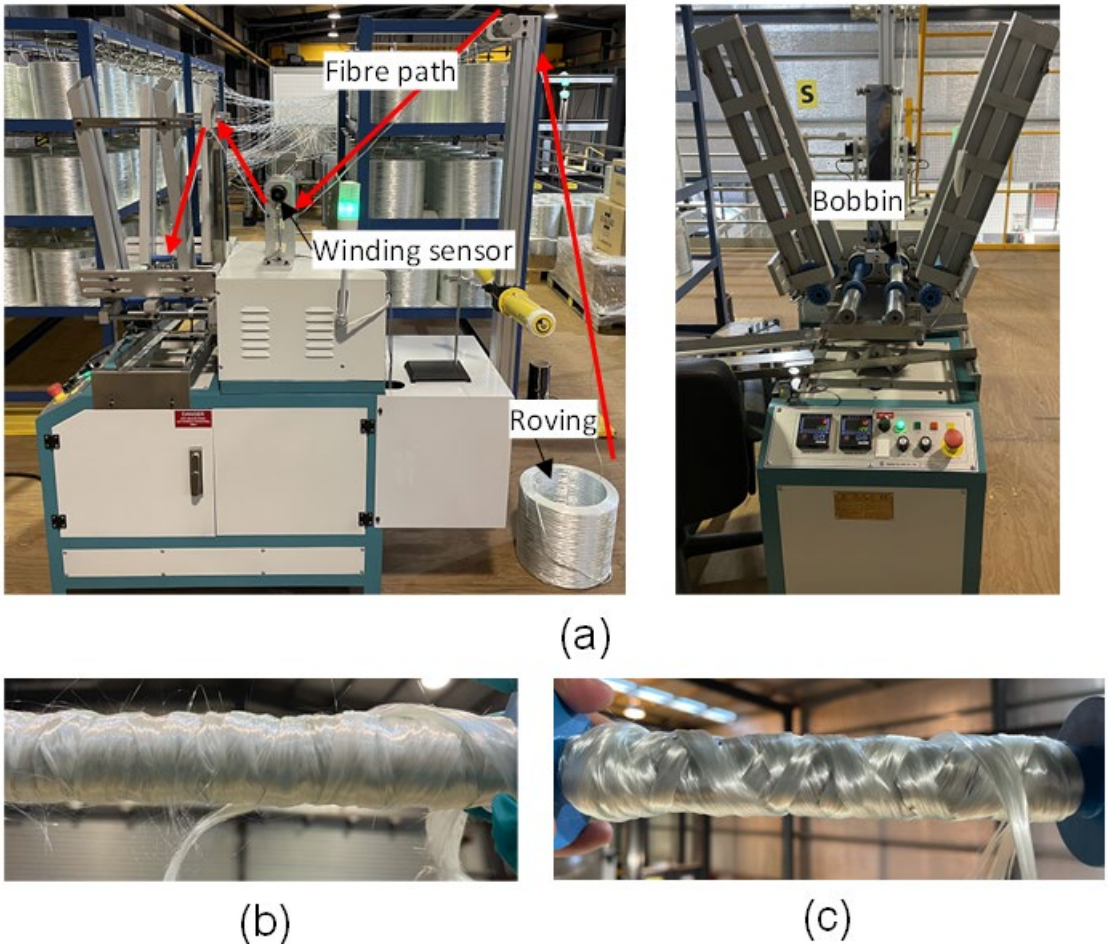

Figure 6.2. (a) Rewinding equipment, (b) rewinding result for glass fibres with yarn damage and (c) accepted bobbin with glass fibres

The key factors for the rewinding quality are the yarn tension and the winding speed. Due to the interference between the yarn and the guide, fibres may spread, and the coherence of the filaments can be damaged, especially for high yarn tension, as shown in Figure 6.2(b). A lower roller speed and a long distance between the raw roving and the bobbin should be

adopted to avoid yarn damage. The acceptable bobbin with glass fibre should have minimal yarn damage, as shown in Figure 6.2(c).

6.2.2. Pull-braiding process

The pull-braiding process is a hybrid manufacturing technique that combines the principles of braiding and pultrusion. The T4L braiding machine is equipped with 60 and 84 fibre carriers that move in a regular direction to intertwine fibres from bobbins, resulting in a 3D-shaped tube with a constant braided fibre angle (off-axis ply) for continuous cross-section parts. The braided structure can be formed into various shapes, including square and circle cross-sections. Fibre can also be passed through the braider forming the 0° ply (pultruded as a 0° layer rather than a tri-axial structure). Figure 6.3 shows the main steps involved in the pull-braiding process, and one braiding layer and one unidirectional layer were adopted.

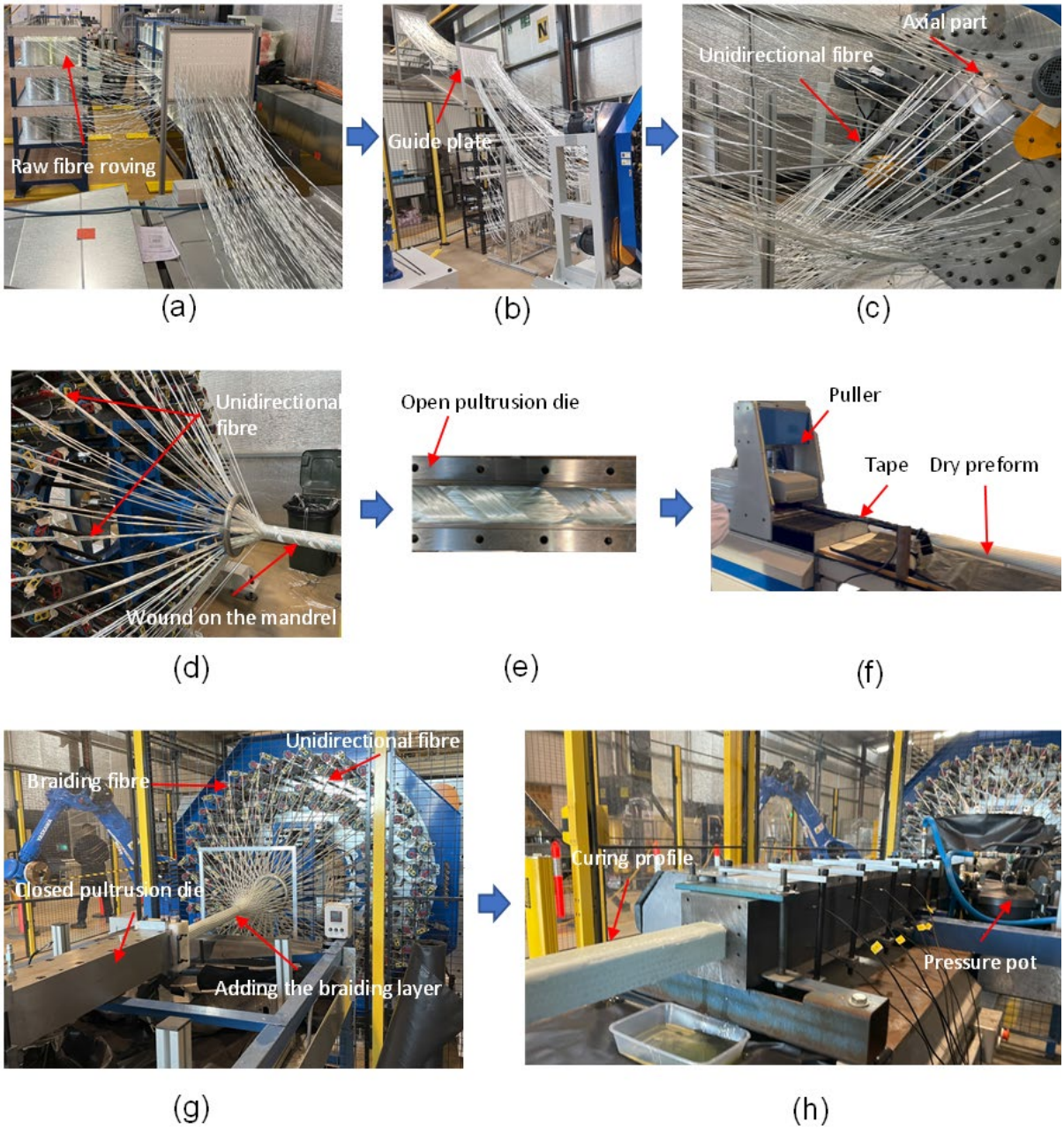

Figure 6.3. A typical pull-braiding process at different stages.

(1) Unidirectional fibre: The raw glass rovings are pulled through the guide plate to the axial part of the braider, which comprises the inner layer of the composite profile, as shown in Figure 6.3(a), Figure 6.3(b), and Fig 6.3(c). The fibre path should be guided to avoid fibre tangling. The cross-sectional area of each yarn A occupied by the fibres can be evaluated as follows (Barbero, 2010):

$$A\ [\mathrm{cm}^2] = 10^{-5}\,\frac{TEX[\mathrm{g/cm}]}{\rho_f\ [\mathrm{g/cm}^3]} \tag{6.1}$$

where TEX is the desired weight per unit length, and ρ_f is the fibre density.

(2) Braiding layer: As discussed in Section 6.2.1, the prepared braiding bobbin is mounted on the carrier of the braiding machine. To fix the unidirectional fibre, a portion of braiding fibres was wound around the bobbin. Next, braiding machine is simultaneously operated and dry fibres are pulled through the open pultrusion die, as illustrated in Figure 6.3(d and e). Concurrently, the puller is activated to pull the dry preform, as depicted in Figure 6.3(f).

Once the dry preform with partially wound fibres is stable, the pultrusion die is closed and all the braiding fibres are introduced, as depicted in Figure 6.3(g). To achieve the desired braiding angle, the braiding parameters and pulling speed are adjusted, which will be further discussed in Section 6.2.3.

(3) Pultrusion process: Following the completion of the braiding operation, the braided preform is directly transferred into a pultrusion system, which is in alignment with the braiding machine. In this study, closed injection pultrusion is employed, which has the advantage of minimising harmful volatile resin emissions. The pultrusion system is composed of two key elements: a resin injection die and a curing die. The connection section (Figure 6.4(b)) incorporates a tapered design to compact the impregnated preform effectively. When the injection die is coupled with the pressure pot, the resin penetrates the dry preform, impregnating the fibres before the curing process takes place within the pultrusion die, as shown in Figure 6.3(h). The vinyl ester polymer resin is used in this project.

The temperature of the curing die, the pulling speed, and the curing duration are all optimised to guarantee sufficient resin curing without causing thermal degradation to the fibres or resin. Ensuring proper curing is crucial for attaining the desired mechanical properties in the final composite material.

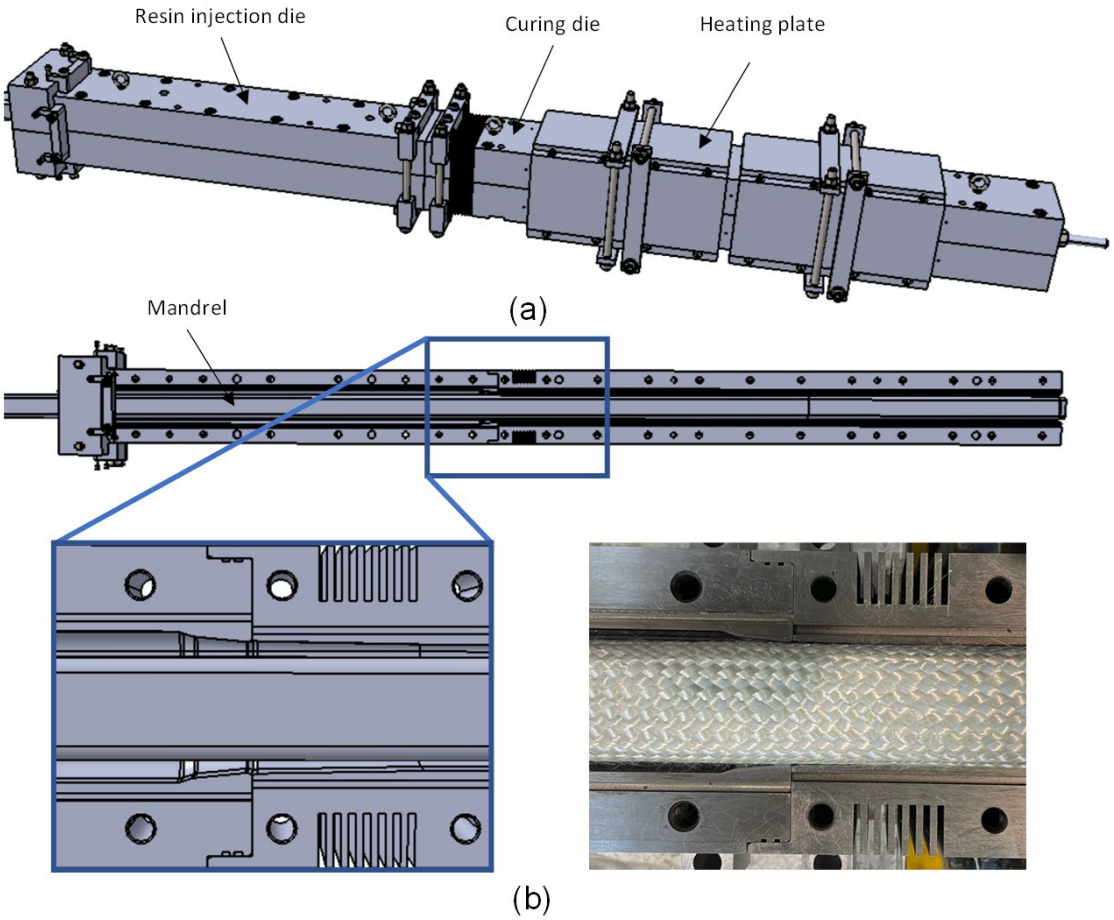

Figure 6.4. Pultrusion die including the resin injection die and the curing die.

(4) Post-processing: When the composite profile is cured, it is extracted from the die using the puller system. The composite profiles are then cut to the required dimensions by the saw.

Figure 6.5 shows that the various forms of the dry preform in the die were examined during the experiment. The pultrusion die process involves three primary stages for the dry preform. In the first stage, the unidirectional layer is pulled through the pultrusion die. The second stage involves completing the braiding layer and adjusting manufacturing parameters to achieve the desired dry preform. Lastly, the third stage consists of injecting the resin and heating the curing die to produce the final composite profiles.

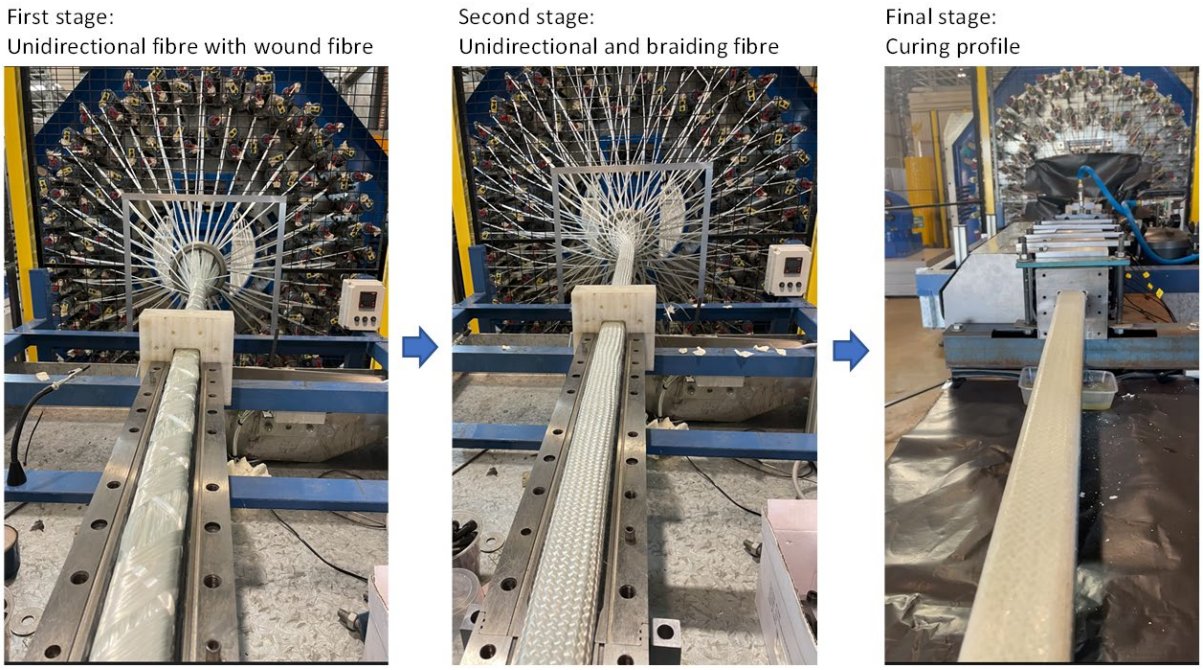

Figure 6.5. The different forms of the dry preform in the die during the experimental preparation process.

6.2.3. Bi-axial braiding

The braiding machine's carriers are mounted with loaded bobbins and configured to perform the desired braiding pattern, such as bi-axial or tri-axial braiding, based on application requirements. This study employs bi-axial braiding, a widely used technique for fabricating preforms with balanced mechanical properties in two primary directions.

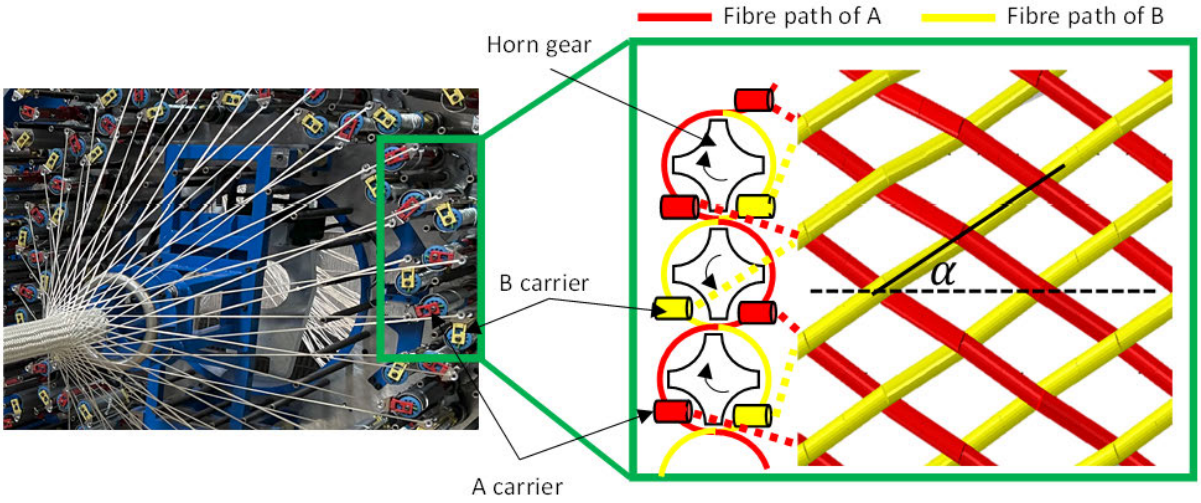

Figure 6.6. Continuous fibres are interlaced at a braided angle.

As illustrated in Figure 6.6, the braiding machine features two colour-coded carriers: Carrier A in yellow and Carrier B in red. The yellow carrier rotates clockwise, while the red carrier rotates counterclockwise. Each colour system can operate independently to form the winding preform, as discussed in Chapters 4 and 5. When used simultaneously, they create a braided preform. In this process, continuous fibres are interlaced at a controlled angle (braiding angle), typically $\pm\alpha$, resulting in a braided structure with enhanced performance under multi-directional loads.

The bobbin carrier rotates at a constant angular velocity ω_h and move along the circular path of the machine's centre. The two different colour-coded carriers move in opposite directions with the velocity ω around the machine's centre, forming the braiding angle α, as shown in Figure 6.6. The braiding angle can be calculated as follows (Sun et al., 2018):

$$\omega = \frac{2\omega_{\mathrm{h}}}{N_c} \tag{6.2}$$

$$\alpha = tan^{-1}\left(\frac{2\omega_{\mathrm{h}}R}{N_{\mathrm{c}}v}\right) \tag{6.3}$$

where R is the radius of the cylindrical mandrel; v is take-up speed; N_{c} is the number of yarn carriers. The desired angle can be adjusted according to user preferences by altering parameters such as braiding speed and take-up speed.

Two theoretical braiding angles, 30° and 45°, are designed by adjusting the settings of the braiding machine and pultrusion speed, as shown in Table 6.1.

Table 6.1. Theoretical design of the braiding angle.

Designed parameter	Value (Design 1)	Value (Design 2)
Number of yarns	84	84
Take-up speed, v (mm/min)	100	100
The radius of the mandrel (mm)	24	24
Rotation speed of carries ω_h (RPM)	16	28
Theoretical braiding angle	29.9°	45.2°

6.3. Braiding simulation

6.3.1. Model description

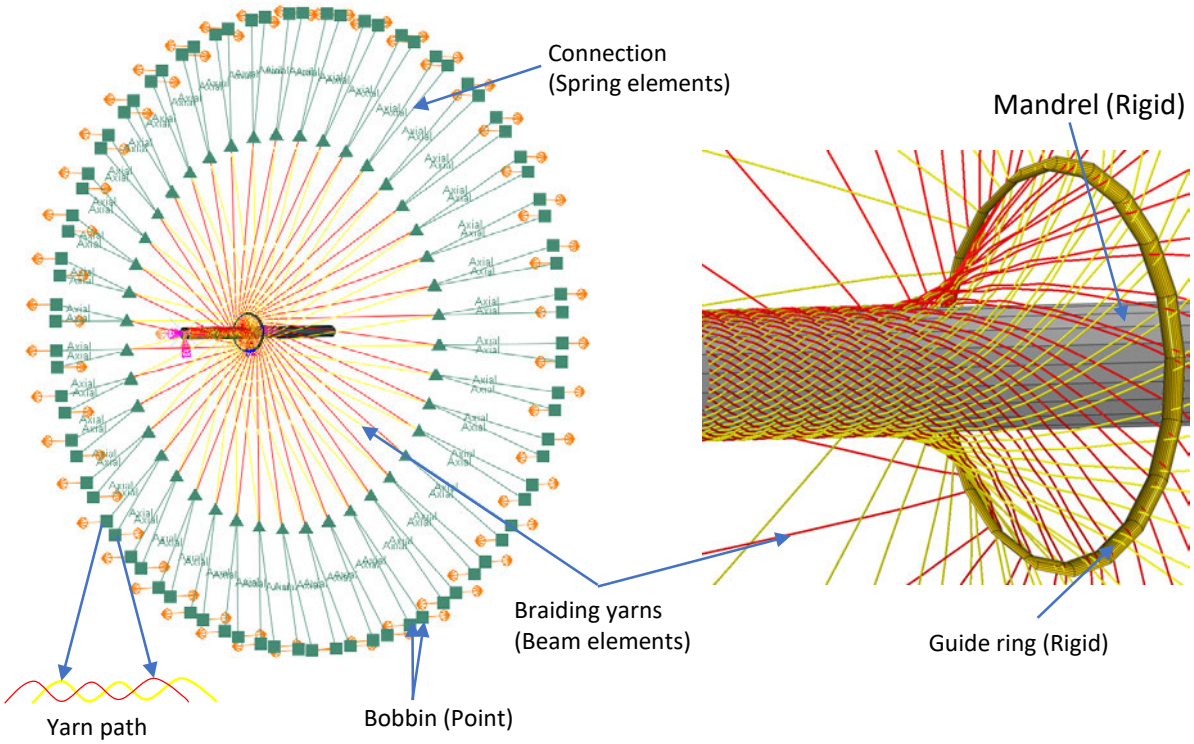

Figure 6.7. Simulation of the braiding process.

A numerical model was developed to simulate the braiding process and predict the geometrical features of the braided structures. The model was implemented using Abaqus 2019, as shown in Figure 6.7. An explicit solver was employed to address convergence issues (Qi et al., 2023; Hans et al., 2015). The mandrel and guide ring were both treated as rigid bodies. The bobbin carrier was simulated by moving points, which included rotation around the machine's centre and an out-of-phase sinusoidal mandrel direction motion for interlacing, as shown in Figure 6.7. It should be noted that the mandrel in the pull-braiding process is fixed, and the dry preform is pulled at a constant take-up speed.

One end of the yarn is connected to the bobbin carrier point using a spring element, which maintains constant yarn tension. The yarn is simulated by truss elements neglecting the bending stiffness, which is closer to the actual properties of the yarn (Hans et al., 2015). Additionally, the truss elements significantly reduce computational time compared to solid elements. However, this model only describes the yarn path and does not account for the yarn deformation. The input parameters for the model are provided in Table 6.2. The yarn properties refer to Table 4 in Chapter 4.

Table 6.2. Specification of the braiding setup in the FEM model.

Property	Value (Case 1)	Value (Case 2)
Yarn properties	ECT 469 PH-4400	ECT 469 PH-4400
The radius of the mandrel (mm)	24	24
Take-up speed, V (mm/min)	100	100
Rotation speed of carries ω_h (RPM)	16	28
Number of yarns	84	84

6.3.2. Characterisation of friction properties

To accurately represent the friction behaviour in the braiding simulation, friction properties were experimentally characterised. This model accounts for the friction coefficient between contacting yarns μ_{YY}, and the friction coefficient between yarns and the mandrel μ_{YM}. The experimental setup to measure the friction coefficient is illustrated in Figure 6.8. An initial load (F_0) is applied on one end of the yarn, and the other end is pulled at a constant speed. The pulling force (F) is then measured using a scale with a resolution of 0.1 N.

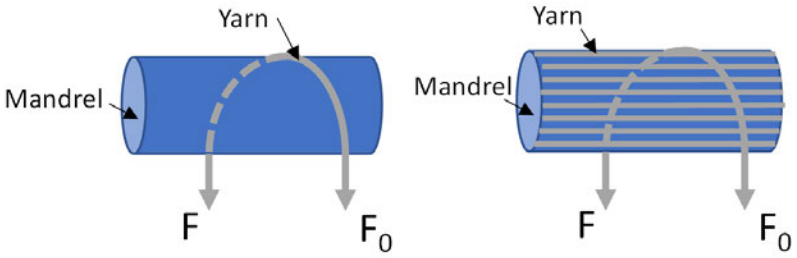

Figure 6.8. Illustration of the measurement of the friction coefficient.

According to the Capstan relation (Cornelissen, Rietman, & Akkerman, 2013), the friction coefficient can be derived as equation 6.5.

$$\mu = \frac{1}{\beta} \ln \left(\frac{F}{F_0}\right) \tag{6.5}$$

where β is the wrapping angle of the yarn on a different surface. The measurement result is shown in Table 6.3.

Table 6.3. Measurement data from the Capstan experiments

Friction interface	Angle	F (N)	F_0 (N)	μ
Yarn and mandrel	180°	6.3	11.3	0.186
	180°	16.05	28.4	0.181
Yarn and yarn	180°	6.3	0.98	0.127

6.3.3. Model validation

To validate the braiding simulation's accuracy, predictions from the model were compared with experimental data obtained during the pull-braiding process. These comparisons focused on geometrical features, such as fibre paths and braiding angles. Figure 6.9 shows the fibre paths from both simulation and experimental results. It can be observed that the simulation and experimental outcomes show similar fibre orientations and distributions, despite neglecting yarn deformation in the model.

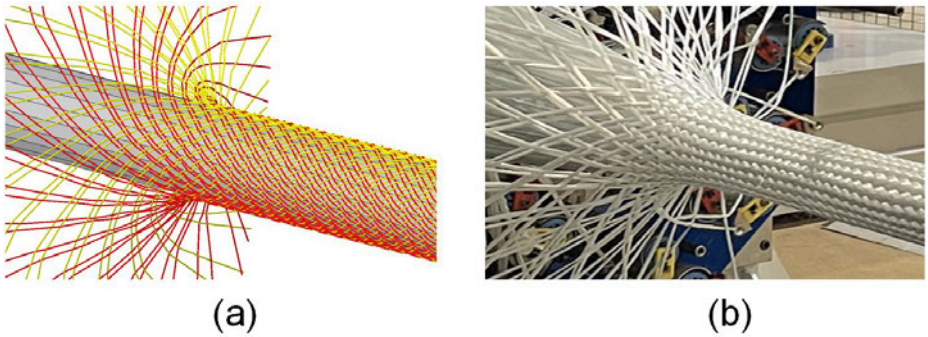

Figure 6.9. Comparison of fibre path between (a) simulation and (b) experimental result.

The braiding angles for both cases are illustrated in Figure 6.10. The validation results demonstrate a good agreement ($\pm 2°$) between the simulation and experimental data, with discrepancies falling within acceptable limits. Given the accurate predictions of fibre paths and braiding angles, this FEM model can be reliably used to predict braided structures.

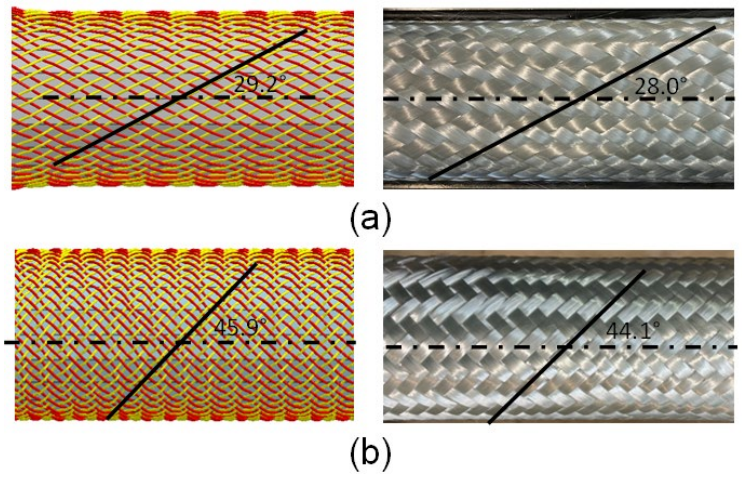

Figure 6.10. Comparison of braiding angles between experimental and simulation results.

6.4. Results and discussion

6.4.1. Simulation of the braided structures

The simulation of braided structures was carried out based on the verified model to analyse the effects of varying process parameters, such as take-up speed and rotation speed of the carrier, on the braiding angle. The main goal of this study was to investigate the relationships between these parameters and the braiding angle, as well as to optimise the braiding process for improved mechanical properties and reduced manufacturing defects at the design stage.

The take-up speed plays an important role in the mechanical performance. The resin can achieve a higher degree of polymerisation at a lower take-up speed. Results showed that as the take-up speed decreased from 200 mm/min to 100 mm/min, the braiding angle increased, leading to a more tightly braided structure, as shown in Figure 6.11. This tighter braided structure can result in a higher volume fraction and higher in-plane stiffness of the composite. However, excessively lower take-up speeds may cause fibre misalignments and other manufacturing defects, which can negatively impact the mechanical performance of the final composite (Potluri, Rawal, Rivaldi, & Porat, 2003).

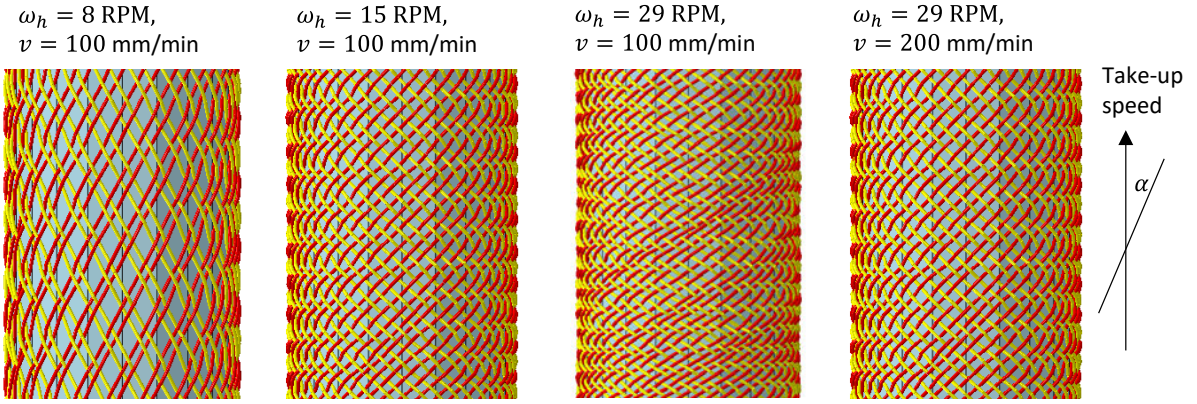

Figure 6.11. Simulations with changes in the angular velocity ω_h of the bobbin carrier and take-up speed.

As the take-up speed is mainly determined by the curing time, the braiding angle is often changed by the angular velocity ω_h of the bobbin carrier. It was observed that increasing the angular velocity led to an increase in the braiding angle, resulting in a more closed braided structure. Based on the simulation results, an optimal combination of take-up speed and rotation speed was identified to achieve the desired braiding angle for the composite preforms.

6.4.2. Common defects in the final braided composite profiles

In this section, the defects observed in the final braided composite profiles manufactured by the pull-braiding technique are discussed, as shown in Figure 6.12(a), particularly concerning the presence of dry fibres in the inner layers and resin-rich areas at the corners. These defects can significantly affect the mechanical performance and long-term durability of the composite material. Drawing upon the analysis of defects observed in the pull-winding technique as discussed in Chapters 4 and 5, it's evident that the defects are more pronounced in the composite profile generated by the pull-braiding technique. This is because the pull-winding technique has been optimised for industrial production, yielding only minor non-uniform fibre distribution within an acceptable range (contributing less than 5% to the final mechanical performance). The pull-braiding production line is in its nascent stages. Consequently, multiple manufacturing factors still require optimisation.

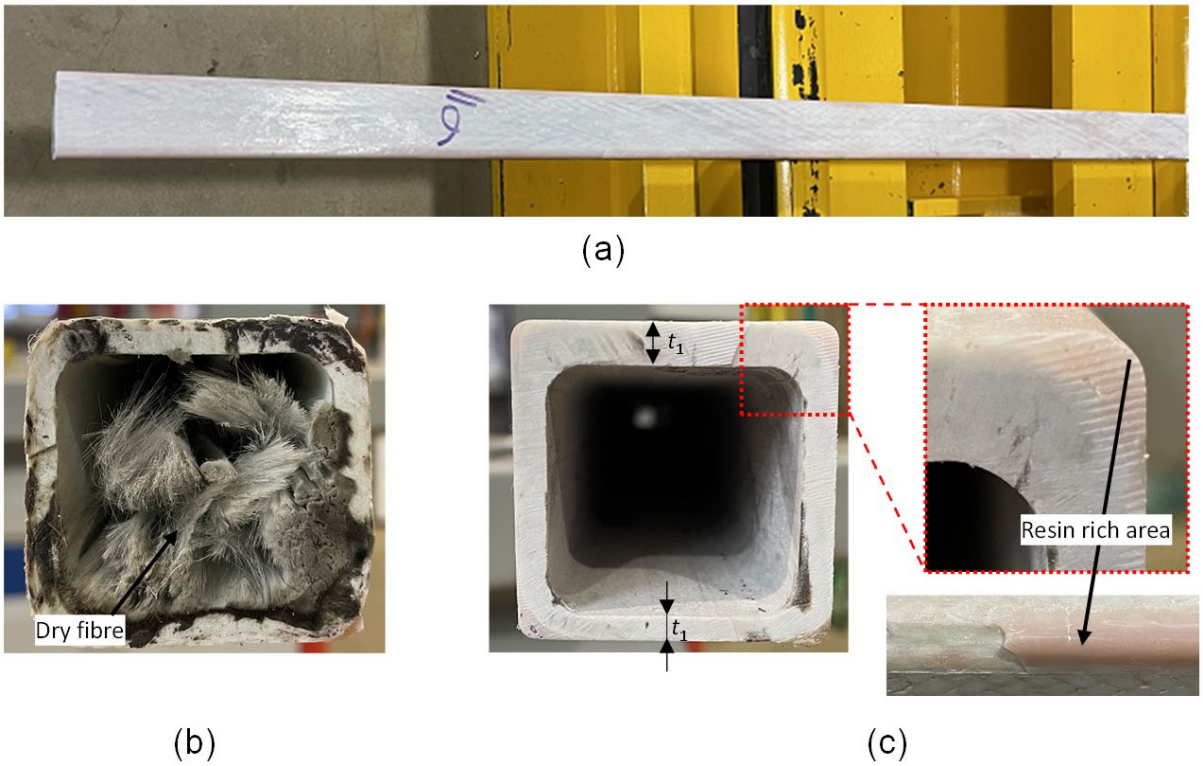

Figure 6.12. Defects in the composite profiles; (a) composite profile manufactured by pull-braiding technique, (b) dry fibres in the inner layer and (c) resin-rich area at the corner.

It was observed that some dry fibres were present in the final composite profiles, especially in the inner layers, as shown in Figure 6.12(b). This phenomenon can be attributed to incomplete impregnation of the fibres due to insufficient resin injection pressure. The

inadequate injection pressure prevents the resin from fully infiltrating the inner layers, resulting in areas where the fibres remain uncoated with the matrix material.

To mitigate this issue, it is recommended to optimise the resin injection die, which can provide high resin injection pressure. Increase the compaction ratio at the entrance of the injection die to avoid the leakage of the resin. Optimise the chambers, such as 'tear drop' geometry (Koppernaes, Nolet, & Fanucci, 1991), ensuring that the fibres in the inner layers are fully impregnated with the resin.

Figure 6.12(c) shows the non-uniform wall thickness throughout the profile. This variation in thickness may have resulted from inconsistencies in the braiding process, rotational movement of the unidirectional fibre, or uneven resin distribution during the pultrusion process. The non-uniform wall thickness can lead to variations in mechanical properties, potentially affecting the overall performance of the composite material in its intended application. To mitigate this issue, further investigation into the process parameters and improved process control may be necessary to ensure consistent wall thickness and optimal composite performance.

Another defect observed in the final composite profiles was the presence of resin-rich areas at the corners, characterised by low fibre volume fractions, as shown in Figure 6.12. This can be attributed to the uneven distribution of fibres during the braiding and pultrusion processes, leading to a concentration of resin at the corners without adequate reinforcement from the fibres.

To address this problem, the fibre distribution and alignment during the braiding and pultrusion processes should be carefully controlled. This may include adjusting the braiding angle, modifying the preform design, or increasing the fibre volume fraction at the corner to ensure a more uniform fibre distribution throughout the composite profile. Moreover, adding another layer of unidirectional fibres can achieve the desired fibre volume and fill the resin-rich gaps at corners.

6.5. Summary and conclusions

This study focused on the manufacturing of braided composite profiles using the pull-braiding and closed injection pultrusion process, with an emphasis on understanding the process parameters and developing a numerical model to predict the geometrical features of the braided structures. A bi-axial braiding technique was employed to create preforms with balanced mechanical properties in two primary directions. The manufacturing process involved four main steps: preparing braiding bobbins, braiding the dry preform, pultrusion, and post-processing.

A numerical model was developed to simulate the braiding process, and its accuracy was validated by comparing the predicted fibre paths and braiding angles with experimental data. This model can be utilized to evaluate manufacturing parameters effectively.

Additionally, defects such as non-uniform fibre distribution, inconsistent wall thickness and resin-rich areas were investigated in the manufacturing process. These defects could potentially impact the mechanical properties and overall performance of the composite material in its intended application. Recommendations for further investigation into process parameters and improved process control were provided to mitigate these defects.

CHAPTER 7: CONCLUSION AND FUTURE WORK

7.1. Conclusions

This thesis has presented a comprehensive investigation into the manufacturing processes, characterisation, and performance of pultruded fibre-reinforced polymer (FRP) composite profiles under compression and bending loads. The focus has been on the effects of defects, such as non-uniform fibre distribution (NUFD) and fibre waviness, on the mechanical behaviour of these structures, specifically in terms of local buckling capacity, compressive strength, and flexural performance. The main findings are as follows:

- **Review on the effect of fibre distribution imperfections on the buckling characteristics of hollow box FRP structures**

This study presents a comprehensive review of the literature on fibre-reinforced polymer (FRP) composites, their manufacturing processes, characterisation methods, and the effects of defects on their mechanical properties. It starts with an overview of FRP composites and their applications in various industries. The review then explores the pultrusion manufacturing process, as well as advancements including pull-winding and pull-braiding that aim to enhance the transverse properties of FRP composites. Next, it discusses the characterisation methods for FRP composites, focusing on techniques to quantify defects such as fibre waviness and non-uniform fibre distribution (NUFD).

Following this, the study reviews the effects of defects on the mechanical properties of FRP composites, including their impact on compressive strength, flexural performance, and local buckling capacity. Lastly, it identifies research gaps and opportunities in the field of FRP composites, setting the stage for the subsequent chapters of this thesis.

- **Fibre waviness characterisation and modelling by Filtered Canny Misalignment Analysis (FCMA)**

The Filtered Canny Misalignment Analysis (FCMA) method was introduced as a novel approach for quantifying in-plane and out-of-plane fibre waviness. FCMA is capable of analysing fibre waviness in a large composite structure. The specimen area in the current research was around 100 cm^2. The FCMA method saved the computational time by about 60% compared with the HRMA method.

The results obtained using the FCMA method were used to develop a finite element model to simulate the effects of fibre waviness on stress distribution in hollow composite columns under axial compression.

- **Formation of Non-uniform Fibre Distributions in Winding-Pultrusion Process and Its Effect on Axial Compressive Properties of Hollow GFRP Profiles**

This study explored the formation and impact of Non-Uniform Fibre Distribution (NUFD) in Pultruded Fibre Reinforced Polymer (PFRP) composite profiles. The winding-pultrusion technique was used to fabricate the profile, and image analysis was employed to measure its NUFD. Results show that the samples with the lowest winding tension generate the largest fibre content variation of 9% at the corner. In addition, the fibre content along the pultrusion is consistent.

A finite element model was used to assess the effect of NUFD on compressive and local buckling failure in short and long columns. The NUFD has a limited effect on the load-bearing capacity of short columns, with a reduction of only 0.98 when the local fibre volume fraction decrease by 30%. However, the reduction factor for buckling failure was lower, with values of 0.91 and 0.97 for the corner NUFD and wall NUFD, respectively, when the local fibre volume fraction decreased by 30%.

- **Formation of non-uniform fibre distribution and its effect on the flexural performance of pultruded GFRP box beams**

This study investigates the effects of non-uniform fibre distributions (NUFD) on the load capacity of box-section composite profiles under bending, focusing on the flange local buckling (FLB) failure mode and compressive material failure. The research highlights the importance of considering the rotational restraint coefficient during bending.

The study also shows that the effect of NUFD location across the section is insignificant in beams dominated by a compressive failure of fibre, where ultimate material strength is reached without buckling instability. Numerical results indicate that the linear trend observed in the regression model is independent of profile geometry and fibre layup for FLB. Additionally, when the fibre volume fraction at the corner is reduced by 30%, it leads to an approximate 21% decrease in the rotational restraint coefficient for S125 and S100 profiles.

- **Numerical simulation and experimental investigation of the braiding-pultrusion process for manufacturing braided composite profiles**

This study focused on manufacturing braided composite profiles using pull-braiding and closed injection pultrusion processes, emphasizing process parameters and developing a numerical model to predict braided structures' geometrical features. A bi-axial braiding technique was used to create preforms with balanced mechanical properties in two primary directions. The manufacturing process consisted of preparing braiding bobbins, braiding the

dry preform, pultrusion, and post-processing. The numerical model, validated by comparing predicted fibre paths and braiding angles with experimental data, effectively evaluates manufacturing parameters.

7.2. Future work

Several areas of future research can be explored to advance the understanding of fibre-reinforced polymer (FRP) composites and their manufacturing processes, including pultrusion and braiding techniques:

- Manufacturing process optimisation: Investigate and optimise the manufacturing process, including resin injection dies, to ensure better impregnation of fibres and minimise defects in the final composite product. Addressing this challenge will improve the overall quality of the pultruded FRP composites.
- Characterisation of fibre defects: Conduct comprehensive experimental studies to characterise the nature of fibre defects and their impact on the mechanical properties of composite materials. Understanding the relationship between fibre defects and material performance is crucial for improving material design and manufacturing processes.
- Theoretical analysis of fibre distribution on buckling: Develop advanced theoretical models to predict the effects of non-uniform fibre distribution on the buckling behaviour of composite structures. These models should account for various types of fibre defects and their implications on structural performance.
- FEM method development: Enhance finite element methods (FEM) to accurately predict the presence and form of defects in composite materials during the manufacturing process. This would enable more accurate simulations and a better understanding of the effects of fibre defects on material performance.

By addressing these research areas, a more comprehensive understanding of FRP composites, their manufacturing processes, and the effects of fibre defects can be achieved, ultimately leading to the development of higher performing, more reliable, and cost-effective composite solutions for various industries.

REFERENCES

Abdurohman, K., Satrio, T., & Muzayadah, N. (2018). *A comparison process between hand lay-up, vacuum infusion and vacuum bagging method toward e-glass EW 185/lycal composites.* Paper presented at the Journal of Physics: Conference Series.

Advani, S. G., & Hsiao, K.-T. (2012). *Manufacturing techniques for polymer matrix composites (PMCs)*: Elsevier.

Advani, S. G., & Sozer, E. M. (2002). *Process modeling in composites manufacturing*: CRC press.

Al-saadi, A. U., Aravinthan, T., & Lokuge, W. (2019). Effects of fibre orientation and layup on the mechanical properties of the pultruded glass fibre reinforced polymer tubes. *Engineering Structures, 198*. doi:10.1016/j.engstruct.2019.109448

Alajarmeh, O., Zeng, X., Aravinthan, T., Shelley, T., Alhawamdeh, M., Mohammed, A., . . . Schubel, P. (2021). Compressive behaviour of hollow box pultruded FRP columns with continuous-wound fibres. *Thin-Walled Structures, 168*, 108300. doi:https://doi.org/10.1016/j.tws.2021.108300

Alhawamdeh, M., Alajarmeh, O., Aravinthan, T., Shelley, T., Schubel, P., Kemp, M., & Zeng, X. (2021). Modelling hollow pultruded FRP profiles under axial compression: Local buckling and progressive failure. *Composite Structures, 262*. doi:10.1016/j.compstruct.2021.113650

Alves, M. P., Cimini Junior, C. A., & Ha, S. K. (2021). Fiber waviness and its effect on the mechanical performance of fiber reinforced polymer composites: An enhanced review. *composites Part A: Applied Science and Manufacturing, 149*. doi:10.1016/j.compositesa.2021.106526

Arani, A. G., Maghamikia, S., Mohammadimehr, M., & Arefmanesh, A. (2011). Buckling analysis of laminated composite rectangular plates reinforced by SWCNTs using analytical and finite element methods. *Journal of Mechanical Science and Technology, 25*(3), 809-820. doi:10.1007/s12206-011-0127-3

Asadi, H., Eynbeygi, M., & Wang, Q. (2014). Nonlinear thermal stability of geometrically imperfect shape memory alloy hybrid laminated composite plates. *Smart materials and structures, 23*(7), 075012.

Ascione, L., Berardi, V. P., Giordano, A., & Spadea, S. (2014). Macro-scale analysis of local and global buckling behavior of T and C composite sections. *Mechanics Research Communications, 58*, 105-111. doi:https://doi.org/10.1016/j.mechrescom.2013.10.004

Ascione, L., Berardi, V. P., Giordano, A., & Spadea, S. (2015). Pre-buckling imperfection sensitivity of pultruded FRP profiles. *Composites Part B: Engineering, 72*, 206-212. doi:https://doi.org/10.1016/j.compositesb.2014.12.014

Ascione, L., Caron, J.-F., Godonou, P., van IJselmuijden, K., Knippers, J., Mottram, T., . . . Tromp, L. (2016). *Prospect for new guidance in the design of FRP: Support to the implementation, harmonization and further development of the Eurocodes*: Publications Office of the European Union.

Avila, A. F., & Morais, D. T. (2005). A multiscale investigation based on variance analysis for hand lay-up composite manufacturing. *Composites Science and Technology, 65*(6), 827-838.

Azeem, M., Ya, H. H., Alam, M. A., Kumar, M., Stabla, P., Smolnicki, M., . . . Ma, Q. (2022). Application of filament winding technology in composite pressure vessels and challenges: a review. *Journal of Energy Storage, 49*, 103468.

Bakis, C. E., Bank, L. C., Brown, V., Cosenza, E., Davalos, J., Lesko, J., . . . Triantafillou, T. (2002). Fiber-reinforced polymer composites for construction—State-of-the-art review. *Journal of Composites for Construction, 6*(2), 73-87.

Banerjee, A., Sun, L., Mantell, S. C., & Cohen, D. (1998). Model and experimental study of fiber motion in wet filament winding. *composites Part A: Applied Science and Manufacturing*, *29*(3), 251-263. doi:https://doi.org/10.1016/S1359-835X(97)00091-2

Bank, L. C. (2006). *Composites for construction: structural design with FRP materials*: John Wiley & Sons.

Baran, I. (2015). *Pultrusion: state-of-the-art process models*: Smithers Rapra.

Baran, I., Straumit, I., Shishkina, O., & Lomov, S. V. (2018). X-ray computed tomography characterization of manufacturing induced defects in a glass/polyester pultruded profile. *Composite Structures*, *195*, 74-82. doi:https://doi.org/10.1016/j.compstruct.2018.04.030

Baran, I., Tutum, C. C., Nielsen, M. W., & Hattel, J. H. (2013). Process induced residual stresses and distortions in pultrusion. *Composites Part B: Engineering*, *51*, 148-161.

Barati, M. R., & Zenkour, A. M. (2017). Post-buckling analysis of refined shear deformable graphene platelet reinforced beams with porosities and geometrical imperfection. *Composite Structures*, *181*, 194-202.

Barbero, E. J. (2010). *Introduction to composite materials design*: CRC press.

Bayat, Y., & EkhteraeiToussi, H. (2017). Exact solution of thermal buckling and post buckling of composite and SMA hybrid composite beam by layerwise theory. *Aerospace Science and Technology*, *67*, 484-494.

Bednarcyk, B. A., Aboudi, J., & Arnold, S. M. (2014). The effect of general statistical fiber misalignment on predicted damage initiation in composites. *Composites Part B: Engineering*, *66*, 97-108. doi:https://doi.org/10.1016/j.compositesb.2014.04.014

Belnoue, J. P. H., & Hallett, S. R. (2020). A rapid multi-scale design tool for the prediction of wrinkle defect formation in composite components. *Materials & Design*, *187*. doi:10.1016/j.matdes.2019.108388

Belnoue, J. P. H., Nixon-Pearson, O. J., Thompson, A. J., Ivanov, D. S., Potter, K. D., & Hallett, S. R. (2018). Consolidation-Driven Defect Generation in Thick Composite Parts. *Journal of Manufacturing Science and Engineering*, *140*(7). doi:10.1115/1.4039555

Boisse, P. (2015). Advances in Composites Manufacturing and Process Design.

Boisse, P., Colmars, J., Hamila, N., Naouar, N., & Steer, Q. (2018). Bending and wrinkling of composite fiber preforms and prepregs. A review and new developments in the draping simulations. *Composites Part B: Engineering*, *141*, 234-249. doi:10.1016/j.compositesb.2017.12.061

Boisse, P., Hamila, N., & Madeo, A. (2016). Modelling the development of defects during composite reinforcements and prepreg forming. *Philos Trans A Math Phys Eng Sci*, *374*(2071), 20150269. doi:10.1098/rsta.2015.0269

Bunsell, A. R. (2009). *Handbook of tensile properties of textile and technical fibres*: Elsevier.

Cai, Z., Gutowski, T., & Allen, S. (1992). Winding and Consolidation Analysis for Cylindrical Composite Structures. *Journal of Composite Materials*, *26*(9), 1374-1399. doi:10.1177/002199839202600908

Calius, E. P., & Springer, G. S. (1990). A model of filament-wound thin cylinders. *International Journal of Solids and Structures*, *26*(3), 271-297. doi:https://doi.org/10.1016/0020-7683(90)90041-S

Callister, W. D., & Rethwisch, D. G. (2007). *Materials science and engineering: an introduction* (Vol. 7): John wiley & sons New York.

Cantwell, W. J., & Morton, J. (1991). The impact resistance of composite materials—a review. *composites*, *22*(5), 347-362.

Cardoso, D. C. T., Harries, K. A., & Batista, E. d. M. (2014a). Closed-form equations for compressive local buckling of pultruded thin-walled sections. *Thin-Walled Structures*, *79*, 16-22. doi:https://doi.org/10.1016/j.tws.2014.01.013

Cardoso, D. C. T., Harries, K. A., & Batista, E. d. M. (2014b). Compressive strength equation for GFRP square tube columns. *Composites Part B: Engineering, 59*, 1-11. doi:https://doi.org/10.1016/j.compositesb.2013.10.057

Carraro, P., Maragoni, L., & Quaresimin, M. (2015). Influence of manufacturing induced defects on damage initiation and propagation in carbon/epoxy NCF laminates. *Advanced Manufacturing: Polymer & Composites Science, 1*(1), 44-53.

Centea, T., & Hubert, P. (2011). Measuring the impregnation of an out-of-autoclave prepreg by micro-CT. *Composites Science and Technology, 71*(5), 593-599. doi:https://doi.org/10.1016/j.compscitech.2010.12.009

Cheng, Q., Wang, J., Wen, J., Liu, C., Jiang, K., Li, Q., & Fan, S. (2010). Carbon nanotube/epoxy composites fabricated by resin transfer molding. *Carbon, 48*(1), 260-266.

Clyne, T. W., & Hull, D. (2019). *An introduction to composite materials*: Cambridge university press.

Cornelissen, B., Rietman, B., & Akkerman, R. (2013). Frictional behaviour of high performance fibrous tows: Friction experiments. *composites Part A: Applied Science and Manufacturing, 44*, 95-104. doi:https://doi.org/10.1016/j.compositesa.2012.08.024

Correia, J. R. o. (2023). Pultrusion of advanced composites. In *Advanced Fiber-Reinforced Polymer (FRP) Composites for Structural Applications* (pp. 137-177): Elsevier.

Croft, K., Lessard, L., Pasini, D., Hojjati, M., Chen, J., & Yousefpour, A. (2011). Experimental study of the effect of automated fiber placement induced defects on performance of composite laminates. *composites Part A: Applied Science and Manufacturing, 42*(5), 484-491. doi:10.1016/j.compositesa.2011.01.007

De Lorenzis, L., & La Tegola, A. (2005). Effect of the actual distribution of applied stresses on global buckling of isotropic and transversely isotropic thin-walled members: Numerical examples. *Composite Structures, 71*(1), 83-100. doi:https://doi.org/10.1016/j.compstruct.2004.09.022

Debski, H., Rozylo, P., & Teter, A. (2020). Buckling and limit states of thin-walled composite columns under eccentric load. *Thin-Walled Structures, 149*. doi:10.1016/j.tws.2020.106627

Dodwell, T. J., Butler, R., & Hunt, G. W. (2014). Out-of-plane ply wrinkling defects during consolidation over an external radius. *Composites Science and Technology, 105*, 151-159. doi:10.1016/j.compscitech.2014.10.007

Du, G. w., & Popper, P. (1994). Analysis of a Circular Braiding Process for Complex Shapes. *The Journal of The Textile Institute, 85*(3), 316-337. doi:10.1080/00405009408631277

Eduljee, R. F., & Gillespie, J. W. (1996). Elastic response of post- and in situ consolidated laminated cylinders. *composites Part A: Applied Science and Manufacturing, 27*(6), 437-446. doi:https://doi.org/10.1016/1359-835X(95)00063-8

El Said, B., Green, S., & Hallett, S. R. (2014). Kinematic modelling of 3D woven fabric deformation for structural scale features. *composites Part A: Applied Science and Manufacturing, 57*, 95-107. doi:10.1016/j.compositesa.2013.11.006

Elhajjar, R. F., & Shams, S. S. (2014). Compression testing of continuous fiber reinforced polymer composites with out-of-plane fiber waviness and circular notches. *Polymer Testing, 35*, 45-55. doi:10.1016/j.polymertesting.2014.02.004

Emerson, M. J., Jespersen, K. M., Dahl, A. B., Conradsen, K., & Mikkelsen, L. P. (2017). Individual fibre segmentation from 3D X-ray computed tomography for characterising the fibre orientation in unidirectional composite materials. *composites Part A: Applied Science and Manufacturing, 97*, 83-92. doi:https://doi.org/10.1016/j.compositesa.2016.12.028

Epsilon Composite. Pullwinging Techinique. Retrieved from https://www.epsilon-composite.com/en/our-solutions/technologies-manufacturing-processes/pullwinding

Fairuz, A., Sapuan, S., Zainudin, E., & Jaafar, C. (2014). Polymer composite manufacturing using a pultrusion process: A review. *American Journal of Applied Sciences, 11*(10), 1798.

Feng, P., Wu, Y., & Liu, T. (2021). Non-uniform fiber-resin distributions of pultruded GFRP profiles. *Composites Part B: Engineering*. doi:10.1016/j.compositesb.2021.109543

Feo, L., Mosallam, A. S., & Penna, R. (2013). Mechanical behavior of web–flange junctions of thin-walled pultruded I-profiles: An experimental and numerical evaluation. *Composites Part B: Engineering, 48*, 18-39. doi:https://doi.org/10.1016/j.compositesb.2012.11.001

Gand, A. K., Chan, T.-M., & Mottram, J. T. (2013). Civil and structural engineering applications, recent trends, research and developments on pultruded fiber reinforced polymer closed sections: a review. *Frontiers of Structural and Civil Engineering, 7*(3), 227-244.

Garcea, S., Wang, Y., & Withers, P. (2018). X-ray computed tomography of polymer composites. *Composites Science and Technology, 156*, 305-319.

Ghayoor, H., Marsden, C. C., Hoa, S. V., & Melro, A. R. (2019). Numerical analysis of resin-rich areas and their effects on failure initiation of composites. *composites Part A: Applied Science and Manufacturing, 117*, 125-133. doi:10.1016/j.compositesa.2018.11.016

Gibson, R. F. (2010). A review of recent research on mechanics of multifunctional composite materials and structures. *Composite Structures, 92*(12), 2793-2810.

Gibson, R. F. (2016). *Principles of composite material mechanics*: CRC press.

Green, S. D., Long, A. C., El Said, B. S. F., & Hallett, S. R. (2014). Numerical modelling of 3D woven preform deformations. *Composite Structures, 108*, 747-756. doi:10.1016/j.compstruct.2013.10.015

Guades, E., Aravinthan, T., Islam, M., & Manalo, A. (2012). A review on the driving performance of FRP composite piles. *Composite Structures, 94*(6), 1932-1942. doi:https://doi.org/10.1016/j.compstruct.2012.02.004

Gupta, M. (2007). *Polymer composite*: New Age International.

Guyader, G., Gabor, A., & Hamelin, P. (2013). Analysis of 2D and 3D circular braiding processes: Modeling the interaction between the process parameters and the pre-form architecture. *Mechanism and Machine Theory, 69*, 90-104. doi:https://doi.org/10.1016/j.mechmachtheory.2013.04.015

Hahn, H. T., Kempner, E. A., & Lee, S. S. (1993). The stress development during filament winding of thick cylinders. *Composites Manufacturing, 4*(3), 147-156. doi:https://doi.org/10.1016/0956-7143(93)90099-T

Hallander, P., Akermo, M., Mattei, C., Petersson, M., & Nyman, T. (2013). An experimental study of mechanisms behind wrinkle development during forming of composite laminates. *composites Part A: Applied Science and Manufacturing, 50*, 54-64. doi:10.1016/j.compositesa.2013.03.013

Hans, T., Cichosz, J., Brand, M., & Hinterhölzl, R. (2015). Finite element simulation of the braiding process for arbitrary mandrel shapes. *composites Part A: Applied Science and Manufacturing, 77*, 124-132. doi:10.1016/j.compositesa.2015.06.003

Haselbach, P. U., Bitsche, R. D., & Branner, K. (2016). The effect of delaminations on local buckling in wind turbine blades. *Renewable Energy, 85*, 295-305.

Hassan, M. H., Othman, A. R., & Kamaruddin, S. (2017). A review on the manufacturing defects of complex-shaped laminate in aircraft composite structures. *The International*

Journal of Advanced Manufacturing Technology, 91(9), 4081-4094. doi:10.1007/s00170-017-0096-5
Heinecke, F., & Willberg, C. (2019). Manufacturing-induced imperfections in composite parts manufactured via automated fiber placement. *Journal of Composites Science, 3*(2), 56.
Hoa, S. V. (2009). *Principles of the manufacturing of composite materials*: DEStech Publications, Inc.
Hollaway, L. (2010). A review of the present and future utilisation of FRP composites in the civil infrastructure with reference to their important in-service properties. *Construction and building materials, 24*(12), 2419-2445.
Hollaway, L. C. (2001). *Advanced polymer composites and polymers in the civil infrastructure*: Elsevier.
Hörrmann, S., Adumitroaie, A., Viechtbauer, C., & Schagerl, M. (2016). The effect of fiber waviness on the fatigue life of CFRP materials. *International Journal of Fatigue, 90*, 139-147.
Isart, N., El Said, B., Ivanov, D. S., Hallett, S. R., Mayugo, J. A., & Blanco, N. (2015). Internal geometric modelling of 3D woven composites: A comparison between different approaches. *Composite Structures, 132*, 1219-1230. doi:10.1016/j.compstruct.2015.07.007
Jeong, H. (1997). Effects of voids on the mechanical strength and ultrasonic attenuation of laminated composites. *Journal of Composite Materials, 31*(3), 276-292.
Jones, R. M. (2006). *Buckling of bars, plates, and shells*: Bull Ridge Corporation.
Journoud, P., Bouvet, C., Castanié, B., & Ratsifandrihana, L. (2022). Experimental analysis of the effects of wrinkles in the radius of curvature of L-shaped carbon-epoxy specimens on unfolding failure. *composites Part A: Applied Science and Manufacturing, 158*, 106975.
Karbhari, V. M. (2007). Introduction: The use of composites in civil structural applications. In *Durability of composites for civil structural applications* (pp. 1-10): Elsevier.
Kessels, J., & Akkerman, R. (2002). Prediction of the yarn trajectories on complex braided preforms. *Composites Part a-Applied Science and Manufacturing, 33*, 1073-1081.
Kollár, L., & Springer, G. (2003). Thin Plates. In G. S. Springer & L. P. Kollár (Eds.), *Mechanics of Composite Structures* (pp. 89-168). Cambridge: Cambridge University Press.
Kollár, L. P. (2003). Local buckling of fiber reinforced plastic composite structural members with open and closed cross sections. *Journal of Structural Engineering, 129*(11), 1503-1513. doi:10.1061/(ASCE)0733-9445(2003)129:11(1503)
Kollar, L. P., & Springer, G. S. (2003). *Mechanics of composite structures*: Cambridge university press.
Koppernaes, C., Nolet, S., & Fanucci, J. (1991). Method and Apparatus for Wetting Fiber Reinforcements With Matrix Materials in the Pultrusion Process Using Continuous In-Line Degassing. *Patent NumberUS 5073413*.
Kubiak, T., Kolakowski, Z., Swiniarski, J., Urbaniak, M., & Gliszczynski, A. (2016). Local buckling and post-buckling of composite channel-section beams–Numerical and experimental investigations. *Composites Part B: Engineering, 91*, 176-188.
Kugler, D., & Moon, T. J. (2002). The effects of Mandrel material and tow tension on defects and compressive strength of hoop-wound, on-line consolidated, composite rings. *composites Part A: Applied Science and Manufacturing, 33*(6), 861-876. doi:https://doi.org/10.1016/S1359-835X(02)00018-0
Kulkarni, P., Mali, K. D., & Singh, S. (2020). An overview of the formation of fibre waviness and its effect on the mechanical performance of fibre reinforced polymer composites.

composites Part A: Applied Science and Manufacturing, 137. doi:10.1016/j.compositesa.2020.106013
Li, Y., Stier, B., Bednarcyk, B., Simon, J.-W., & Reese, S. (2016). The effect of fiber misalignment on the homogenized properties of unidirectional fiber reinforced composites. *Mechanics of Materials, 92*, 261-274. doi:10.1016/j.mechmat.2015.10.002
Liang, B., Hamila, N., Peillon, M., & Boisse, P. (2014). Analysis of thermoplastic prepreg bending stiffness during manufacturing and of its influence on wrinkling simulations. *composites Part A: Applied Science and Manufacturing, 67*, 111-122. doi:10.1016/j.compositesa.2014.08.020
Lightfoot, J. S., Wisnom, M. R., & Potter, K. (2013a). Defects in woven preforms: Formation mechanisms and the effects of laminate design and layup protocol. *composites Part A: Applied Science and Manufacturing, 51*, 99-107. doi:10.1016/j.compositesa.2013.04.004
Lightfoot, J. S., Wisnom, M. R., & Potter, K. (2013b). A new mechanism for the formation of ply wrinkles due to shear between plies. *composites Part A: Applied Science and Manufacturing, 49*, 139-147. doi:10.1016/j.compositesa.2013.03.002
Liu, P., Hou, S., Chu, J., Hu, X., Zhou, C., Liu, Y., . . . Yan, L. (2011). Finite element analysis of postbuckling and delamination of composite laminates using virtual crack closure technique. *Composite Structures, 93*(6), 1549-1560.
Liu, T., & Harries, K. A. (2018). Flange local buckling of pultruded GFRP box beams. *Composite Structures, 189*, 463-472. doi:10.1016/j.compstruct.2018.01.101
Liu, T., Yang, J.-Q., Feng, P., & Harries, K. A. (2020). Determining rotational stiffness of flange-web junction of pultruded GFRP I-sections. *Composite Structures, 236*. doi:10.1016/j.compstruct.2019.111843
Long, A. C. (2005). *Design and manufacture of textile composites*: Elsevier.
Madenci, E., Onuralp Özkılıç, Y., & Gemi, L. (2020). Buckling and free vibration analyses of pultruded GFRP laminated composites: Experimental, numerical and analytical investigations. *Composite Structures, 254*. doi:10.1016/j.compstruct.2020.112806
Mahadik, Y., & Hallett, S. R. (2011). Effect of fabric compaction and yarn waviness on 3D woven composite compressive properties. *composites Part A: Applied Science and Manufacturing, 42*(11), 1592-1600. doi:10.1016/j.compositesa.2011.07.006
Matthews, F. L., Davies, G., Hitchings, D., & Soutis, C. (2000). *Finite element modelling of composite materials and structures*: Elsevier.
Mazumdar, S. (2001). *Composites manufacturing: materials, product, and process engineering*: CrC press.
Mizukami, K., Mizutani, Y., Kimura, K., Sato, A., Todoroki, A., & Suzuki, Y. (2016). Detection of in-plane fiber waviness in cross-ply CFRP laminates using layer selectable eddy current method. *composites Part A: Applied Science and Manufacturing, 82*, 108-118. doi:10.1016/j.compositesa.2015.11.040
Mouritz, A. P., Bannister, M. K., Falzon, P., & Leong, K. (1999). Review of applications for advanced three-dimensional fibre textile composites. *composites Part A: Applied Science and Manufacturing, 30*(12), 1445-1461.
Mouritz, A. P., & Gibson, A. G. (2007). *Fire properties of polymer composite materials* (Vol. 143): Springer Science & Business Media.
Mujahid, Y., Sallih, N., Mustapha, M., Abdullah, M. Z., & Mustapha, F. (2020). Effects of processing parameters for vacuum-bagging-only method on shape conformation of laminated composites. *Processes, 8*(9), 1147.
Mukhopadhyay, S., Jones, M. I., & Hallett, S. R. (2015). Compressive failure of laminates containing an embedded wrinkle; experimental and numerical study. *composites Part*

A: Applied Science and Manufacturing, 73, 132-142. doi:10.1016/j.compositesa.2015.03.012

Muralidhara, B., Babu, S. K., & Suresha, B. (2020). Utilizing vacuum bagging process to prepare carbon fiber/epoxy composites with improved mechanical properties. *Materials Today: Proceedings, 27*, 2022-2028.

Naouar, N., Vidal-Salle, E., Schneider, J., Maire, E., & Boisse, P. (2014). Meso-scale FE analyses of textile composite reinforcement deformation based on X-ray computed tomography. *Composite Structures, 116*, 165-176. doi:10.1016/j.compstruct.2014.04.026

Naouar, N., Vidal-Salle, E., Schneider, J., Maire, E., & Boisse, P. (2015). 3D composite reinforcement meso FE analyses based on X-ray computed tomography. *Composite Structures, 132*, 1094-1104. doi:10.1016/j.compstruct.2015.07.005

Netzel, C., Mordasini, A., Schubert, J., Allen, T., Battley, M., Hickey, C. M. D., . . . Bickerton, S. (2021). An experimental study of defect evolution in corners by autoclave processing of prepreg material. *composites Part A: Applied Science and Manufacturing, 144*. doi:10.1016/j.compositesa.2021.106348

Nishi, M. (2015). Forming Simulation of Textile Composites using LS-DYNA.

Nosrat Nezami, F., Gereke, T., & Cherif, C. (2016). Analyses of interaction mechanisms during forming of multilayer carbon woven fabrics for composite applications. *composites Part A: Applied Science and Manufacturing, 84*, 406-416. doi:10.1016/j.compositesa.2016.02.023

Pagani, A., & Sanchez-Majano, A. (2022). Influence of fiber misalignments on buckling performance of variable stiffness composites using layerwise models and random fields. *Mechanics of Advanced Materials and Structures, 29*(3), 384-399.

Pickett, A. K., Sirtautas, J., & Erber, A. (2009). Braiding Simulation and Prediction of Mechanical Properties. *Applied Composite Materials, 16*(6), 345-364. doi:10.1007/s10443-009-9102-x

Potluri, P., Rawal, A., Rivaldi, M., & Porat, I. (2003). Geometrical modelling and control of a triaxial braiding machine for producing 3D preforms. *Composites Part a-Applied Science and Manufacturing, 34*, 481-492.

Potter, K., Khan, B., Wisnom, M., Bell, T., & Stevens, J. (2008). Variability, fibre waviness and misalignment in the determination of the properties of composite materials and structures. *composites Part A: Applied Science and Manufacturing, 39*(9), 1343-1354. doi:10.1016/j.compositesa.2008.04.016

Poulton, M., & Sebastian, W. (2021). Taxonomy of fibre mat misalignments in pultruded GFRP bridge decks. *composites Part A: Applied Science and Manufacturing, 142*. doi:10.1016/j.compositesa.2020.106239

Qi, S., Alajarmeh, O., Shelley, T., Schubel, P., Rendle-Short, K., & Zeng, X. (2023). Fibre waviness characterisation and modelling by Filtered Canny Misalignment Analysis (FCMA). *Composite Structures, 307*, 116666. doi:https://doi.org/10.1016/j.compstruct.2023.116666

Qiao, P., Davalos, J. F., & Wang, J. (2001). Local buckling of composite FRP shapes by discrete plate analysis. *Journal of Structural Engineering, 127*(3), 245-255.

Rajak, D. K., Pagar, D. D., Kumar, R., & Pruncu, C. I. (2019). Recent progress of reinforcement materials: a comprehensive overview of composite materials. *Journal of Materials Research and Technology, 8*(6), 6354-6374.

Ramôa Correia, J. (2013). 9 - Pultrusion of advanced fibre-reinforced polymer (FRP) composites. In J. Bai (Ed.), *Advanced Fibre-Reinforced Polymer (FRP) Composites for Structural Applications* (pp. 207-251): Woodhead Publishing.

Raouf, R. A. (1996). Effect of Fiber Waviness on the Buckling of Composite Plates. In *Engineering, Construction, and Operations in Space V* (pp. 1102-1107).
Reddy, J. N. (2003). *Mechanics of laminated composite plates and shells: theory and analysis*: CRC press.
Rouf, K., Worswick, M. J., & Montesano, J. (2021). A multiscale framework for predicting the mechanical properties of unidirectional non-crimp fabric composites with manufacturing induced defects. *Journal of Composite Materials, 55*(6), 741-757.
Roy, S. S., Zou, W., & Potluri, P. (2016). Influence of braid carrier tension on carbon fibre braided preforms. In Y. Kyosev (Ed.), *Recent Developments in Braiding and Narrow Weaving* (pp. 91-102). Cham: Springer International Publishing.
Saenz-Castillo, D., Martín, M., Calvo, S., Rodriguez-Lence, F., & Güemes, A. (2019). Effect of processing parameters and void content on mechanical properties and NDI of thermoplastic composites. *composites Part A: Applied Science and Manufacturing, 121*, 308-320.
Safonov, A., Gusev, M., Saratov, A., Konstantinov, A., Sergeichev, I., Konev, S., . . . Akhatov, I. (2020). Modeling of cracking during pultrusion of large-size profiles. *Composite Structures, 235*, 111801. doi:https://doi.org/10.1016/j.compstruct.2019.111801
Shojaei, A., Ghaffarian, S. R., & Karimian, S. M.-H. (2003). Modeling and simulation approaches in the resin transfer molding process: a review. *Polymer Composites, 24*(4), 525-544.
Sitohang, R. D. R., Grouve, W. J. B., Warnet, L. L., & Akkerman, R. (2021). Effect of in-plane fiber waviness defects on the compressive properties of quasi-isotropic thermoplastic composites. *Composite Structures, 272*. doi:10.1016/j.compstruct.2021.114166
Sjölander, J., Hallander, P., & Åkermo, M. (2016). Forming induced wrinkling of composite laminates: A numerical study on wrinkling mechanisms. *composites Part A: Applied Science and Manufacturing, 81*, 41-51. doi:10.1016/j.compositesa.2015.10.012
Smith, R. A., Nelson, L. J., Mienczakowski, M. J., & Challis, R. E. (2009). Automated analysis and advanced defect characterisation from ultrasonic scans of composites. *Insight-Non-Destructive Testing and Condition Monitoring, 51*(2), 82-87.
Starr, T. F., & Ketel, J. (2000). 1 - Composites and pultrusion. In T. F. Starr (Ed.), *Pultrusion for Engineers* (pp. 1-18): Woodhead Publishing.
Staszewski, W., Mahzan, S., & Traynor, R. (2009). Health monitoring of aerospace composite structures–Active and passive approach. *Composites Science and Technology, 69*(11-12), 1678-1685.
Strongwell. Pultrusion process for composite materials. Retrieved from https://www.strongwell.com/
Sun, X., Kawashita, L. F., Wollmann, T., Spitzer, S., Langkamp, A., & Gude, M. (2018). Experimental and numerical studies on the braiding of carbon fibres over structured end-fittings for the design and manufacture of high performance hybrid shafts. *Production Engineering, 12*(2), 215-228. doi:10.1007/s11740-018-0824-1
Sutcliffe, M. P. F. (2013). Modelling the effect of size on compressive strength of fibre composites with random waviness. *Composites Science and Technology, 88*, 142-150. doi:10.1016/j.compscitech.2013.09.002
Thompson, A. J., Belnoue, J. P. H., & Hallett, S. R. (2020). Modelling defect formation in textiles during the double diaphragm forming process. *Composites Part B: Engineering, 202*. doi:10.1016/j.compositesb.2020.108357
Thompson, A. J., El Said, B., Belnoue, J. P. H., & Hallett, S. R. (2018). Modelling process induced deformations in 0/90 non-crimp fabrics at the meso-scale. *Composites Science and Technology, 168*, 104-110. doi:10.1016/j.compscitech.2018.08.029

Thompson, A. J., McFarlane, J. R., Belnoue, J. P. H., & Hallett, S. R. (2020). Numerical modelling of compaction induced defects in thick 2D textile composites. *Materials & Design, 196*. doi:10.1016/j.matdes.2020.109088

Trask, R. S., Hallett, S. R., Helenon, F. M. M., & Wisnom, M. R. (2012). Influence of process induced defects on the failure of composite T-joint specimens. *composites Part A: Applied Science and Manufacturing, 43*(4), 748-757. doi:10.1016/j.compositesa.2011.12.021

Uddin, N. (2013). *Developments in fiber-reinforced polymer (FRP) composites for civil engineering*: Elsevier.

Vaidya, U., & Chawla, K. (2008). Processing of fibre reinforced thermoplastic composites. *International Materials Reviews, 53*(4), 185-218.

Vasiliev, V. V., & Morozov, E. V. (2001). *Mechanics and analysis of composite materials*: Elsevier.

Wagners CFT n.d. Wagners-Composites Fibre Technologies (CFT). Retrieved from https://www.wagner.com.au/main/what-we-do/composite-fibre-technologies/cft-home/

Wilhelmsson, D., Gutkin, R., Edgren, F., & Asp, L. E. (2018). An experimental study of fibre waviness and its effects on compressive properties of unidirectional NCF composites. *composites Part A: Applied Science and Manufacturing, 107*, 665-674. doi:10.1016/j.compositesa.2018.02.013

Wisnom, M. (1999). Size effects in the testing of fibre-composite materials. *Composites Science and Technology, 59*(13), 1937-1957.

Wisnom, M. R., Gigliotti, M., Ersoy, N., Campbell, M., & Potter, K. D. (2006). Mechanisms generating residual stresses and distortion during manufacture of polymer–matrix composite structures. *composites Part A: Applied Science and Manufacturing, 37*(4), 522-529. doi:https://doi.org/10.1016/j.compositesa.2005.05.019

Wright, P., Fu, X., Sinclair, I., & Spearing, S. (2008). Ultra high resolution computed tomography of damage in notched carbon fiber—epoxy composites. *Journal of Composite Materials, 42*(19), 1993-2002.

Wu, C., Gu, Y., Luo, L., Xu, P., Wang, S., Li, M., & Zhang, Z. (2018). Influences of in-plane and out-of-plane fiber waviness on mechanical properties of carbon fiber composite laminate. *Journal of Reinforced Plastics and Composites, 37*(13), 877-891. doi:10.1177/0731684418765981

Yousaf, Z., Potluri, P., Withers, P. J., Mollenhauer, D., Zhou, E., & Duning, S. (2018). Digital element simulation of aligned tows during compaction validated by computed tomography (CT). *International Journal of Solids and Structures, 154*, 78-87. doi:10.1016/j.ijsolstr.2017.05.044

Yu, F., Chen, S., Viisainen, J. V., Sutcliffe, M. P. F., Harper, L. T., & Warrior, N. A. (2020). A macroscale finite element approach for simulating the bending behaviour of biaxial fabrics. *Composites Science and Technology, 191*. doi:10.1016/j.compscitech.2020.108078

Yuksel, O., Sandberg, M., Hattel, J. H., Akkerman, R., & Baran, I. (2021). Mesoscale process modeling of a thick pultruded composite with variability in fiber volume fraction. *Materials (Basel), 14*(13). doi:10.3390/ma14133763

Zhang, L., Zhang, S., Xu, D., & Chen, X. (2019). Compressive behavior of unidirectional FRP with spacial fibre waviness and non-uniform fibre packing. *Composite Structures, 224*, 111082. doi:https://doi.org/10.1016/j.compstruct.2019.111082

Zu, L. (2012). Design and optimization of filament wound composite pressure vessels.

Zweben, C. (1998). Advances in composite materials for thermal management in electronic packaging. *Jom, 50*(6), 47-51.

APPENDIX A: MATLAB SCRIPTS FOR THE FCMA METHOD

```
%#########################################################################%
% Written by : Songming Qi (Songming.qi@usq.edu.au)
% FCMA method
% V3
%#########################################################################%
clc,clear,close all;
%--------------------Input parameters -------------------------------------
Imagenamea = ('random_fibres_1_0_10deg');
Mode = 1;                       % 1: Continous mode 0: Discrete mode
Fibre_diam = 7 ;                % unit: pixel
Background = 1;                 % 1:Black  0:White   color of background
Cell_Size_X =200;               % unit : pixel
Cell_Size_Y = Cell_Size_X;
design_angle=0;
numOfBins=35;                   %number of bins
alpha = 1.1;                    %The maximum width of the fibre*1.1
beta = 0.5;                     %The minimum length of the fibre
sensative = 0.01;

% Filetering fibre is implemented by the pixel instead of real length
%-------------------------------------------------------------------------
Imagename = [Imagenamea,'.tif'];                            %format of the image
Minor_axis_length = alpha*Fibre_diam;                       %unit: pixel
Major_axis_length = beta*min(Cell_Size_X,Cell_Size_Y);      %The minimum length of the
fibre
if (Mode == 1)
   Grid_width=0.03; %the width of grid line
else
    Grid_width=1; %the width of grid line
end
%-------------------------------------------------------------------------
```

```
warning off
I=imread(Imagename);
fprintf('-------------------------------------------------------------\n')
fprintf(' The parameters should be considered and input:\n')
fprintf(' imagename = %s\n',Imagename)
fprintf(' Original image size in pixel = %i x %i\n',size(I,1),size(I,2));
%% step 1: Greyscale image
figure(1)
scrsz = get(groot,'ScreenSize');
IG=rgb2gray(I);
if Background == 1
   IG=imcomplement(IG);
end
imshow(IG)
IG_grid=IG;
title('Original picture')
%% step 2: Grids
[mx,ny]=size(IG);
Num_Xcell=floor(ny/Cell_Size_X); % the number of grid in X direction
Num_Ycell=floor(mx/Cell_Size_Y); % the number of grid in Y direction

ydeta=floor(mx/Num_Ycell);
xdeta=floor(ny/Num_Xcell);
GridX=1:xdeta:xdeta*(Num_Xcell+1);
GridY=1:ydeta:ydeta*(Num_Ycell+1);
for i=1:Num_Ycell   %  Longitude direction
   IG_grid(i*ydeta:i*ydeta+2*Grid_width,:)=255;
end
for j=1:Num_Xcell   %  Horizontal direction
   IG_grid(:,j*xdeta:j*xdeta+2*Grid_width,:)=255;
end
%%% plot grid
IG_grid_1 = IG_grid;
for i=1:Num_Ycell   %  Longitude direction
```

```
   IG_grid_1(i*ydeta:i*ydeta+2*Grid_width,:)=160;
end
for j=1:Num_Xcell   %  Horizontal direction
   IG_grid_1(:,j*xdeta:j*xdeta+2*Grid_width,:)=160;
end

IG_grid_RGB=repmat(IG_grid_1,[1,1,3]);

figure(2)
imshow(IG_grid)
title('Picture with Cell')
%% step 3 : Canny edge
figure(3)
BW=edge(IG_grid,'Canny',sensative);       %Threshold %%method: Prewitt Sobel    Roberts
approxcanny
imshow(BW)
title('Edge detect')

%-------------------------------------%
%%  step 4 ; Filter the fibre
BW_angle = 1.0*BW;
data = regionprops(BW,'MajorAxisLength','orientation','MinorAxisLength','pixelidxlist');
  % get orientation and pixels list of each region
Totalnum_edge = numel(data);

for i = 1:numel(data)
   idx = data(i).PixelIdxList;                  % pixel indices of current region
   MajoraxisL = data(i).MajorAxisLength;
   MinoraxisL = data(i).MinorAxisLength;
   ori = data(i).Orientation;
   if (MajoraxisL <Major_axis_length || MinoraxisL>Minor_axis_length )
    % filter the connected fibre and noise
      ori=NaN;
   end
```

```
    if (ori == 90 || ori == 0  || ori== 45 || ori == -45 )
        ori=NaN;
    end
%    if (ori>=-30) || (ori<=-75)                    % delete noise
%        ori=0;
%     end
    BW_angle(idx) = ori;                           % assign angle value
end
% delete the angle induced by the grid line.
Grid_width_angel=Grid_width+1;
for i=1:Num_Ycell     % Longitude
   BW_angle(i*ydeta-Grid_width_angel:i*ydeta+2*Grid_width_angel,:)=NaN;
end
for j=1:Num_Xcell     % Horizontal
   BW_angle(:,j*xdeta-Grid_width_angel:j*xdeta+2*Grid_width_angel,:)=NaN;
end
%statistic the number of the valid fibre
invalid_edge=0;
Data_Temp = regionprops(BW,'orientation','pixelidxlist');
% get orientation and pixels list of each region

for i = 1:numel(Data_Temp)
    ori_1 = data(i).Orientation;
    if (ori_1 == 90 || ori_1 == 0  || ori_1== 45 || ori_1 == -45 )
        invalid_edge=invalid_edge+1;
    end

end
Totalnum_edge_valid = Totalnum_edge - invalid_edge;

%% Project the fibre angle on the original picture.
BW_angle_NaN=BW_angle;
BW_angle_NaN(BW_angle_NaN==0)=NaN;   % used for image
BW_angle_NaNEx=BW_angle_NaN(find(~isnan(BW_angle_NaN)));
```

```
Angle_Valid=unique(BW_angle_NaN(~isnan(BW_angle_NaN)));  % Valid angle
Std_deva_global = std(Angle_Valid);
No_edge = size(Angle_Valid,1); % the number of the edge
Angle_project = figure('Position',[scrsz(3)*0.05 scrsz(4)*0.1 scrsz(3)*0.9 scrsz(4)*0.35]);
b=imshow(IG_grid_RGB);
set(b,'alphadata',1)
hold on
h=imagesc(BW_angle_NaN);                %% bandwith
ax1=gca;
axis image
% set(gca,'xtick',[])
% set(gca,'ytick',[])
set(gca, 'Color','none')
set(h,'alphadata',~isnan(BW_angle_NaN))        %NaN - Transparent
cc = colorbar(ax1);
colormap(jet)
cc.Label.String = 'Winding angle(¡ã)';
%caxis([-80,-10])
% saveas(gcf,'aa.tif')
% title('Winding angle project')
%-------------------------------------------------------------------------------------------------
%% Step 5 : Grid mean angle
Num_Cell_Ver=size(GridY,2)-1;
Num_Cell_Hor=size(GridX,2)-1;
Cell_mean_Angle=zeros(Num_Cell_Ver*Num_Cell_Hor,1);
No_Cell=0;   % The number of grid
Fill_Hor=zeros(Num_Cell_Ver*Num_Cell_Hor,4);
Fill_Ver=zeros(Num_Cell_Ver*Num_Cell_Hor,4);
MeanTempX=zeros(Num_Cell_Ver,1);
y1=zeros(Num_Cell_Ver,1);   %
for m=1:Num_Cell_Ver
   for j=1:Num_Cell_Hor
      No_Cell=No_Cell+1;
      Temp= BW_angle_NaN((GridY(m):(GridY(m+1)-1)),GridX(j):GridX(j+1)-1);
```

```
        Temp1= Temp(~isnan(Temp));
%       Temp1 = unique(Temp1);
%        if size(Temp1,1)<1
%            Temp1 = NaN;
%        end
        Cell_mean_Angle(No_Cell) = mean(Temp1);
        Fill_Hor(No_Cell,:) = [GridX(j),GridX(j),GridX(j+1),GridX(j+1)];
        Fill_Ver(No_Cell,:) = [GridY(m),GridY(m+1),GridY(m+1),GridY(m)];
        if isnan(Cell_mean_Angle(No_Cell))
           MeanTempX(m,1)=MeanTempX(m,1);
        else
        MeanTempX(m,1)=(MeanTempX(m,1)+Cell_mean_Angle(No_Cell))/2;
    %% based on the vertical
        end
    end
     y1(m)=mean([GridY(m),GridY(m+1)]);

end
No_valid_Cell=size(Cell_mean_Angle(~isnan(Cell_mean_Angle)),1);
figure('Position',[scrsz(3)*0.05 scrsz(4)*0.1 scrsz(3)*0.9 scrsz(4)*0.35]);
for i=1:No_Cell
fill(Fill_Hor(i,:),Fill_Ver(i,:),Cell_mean_Angle(i,1));
hold on
end
set(gca,'YDir','reverse')
ca=colorbar;
ca.Label.String = 'Winding angle(¡ã)';
set(gca,'ytick',[])
set(gca,'xtick',[])
axis image
title('Fill cell')
set(gca,'LooseInset', max(get(gca,'TightInset'), 0.03))
theta_max= prctile(abs(Cell_mean_Angle),99);
% 99% of the misalignment
```

```
Cell_mean_Angle_AVE=Cell_mean_Angle(find(~isnan(Cell_mean_Angle)));
phi_bar = mean(Cell_mean_Angle_AVE);   %% mean
theta_bar = mean(abs(Cell_mean_Angle_AVE));   %%misalignment
Std_deva = std(Cell_mean_Angle_AVE);

% %% export cell mean angle to file for FEM
% Cell_mean_angle_Output = Cell_mean_Angle;
% fname=Imagenamea;
% fname(end-1:end)=[]; % removing .tif from end of file
% save_name=[fname,'_angles.txt'];
% fileID = fopen(save_name,'w');
% fprintf(fileID,', 0 \n'); % needed default value for first row in Abaqus
% for i=1:No_Cell
%     if isnan(Cell_mean_angle_Output(i)) == 1
%         Cell_mean_angle_Output(i) = 0;
%     end
%     fprintf(fileID,'%d , %6.2f  \n', i, -(Cell_mean_angle_Output(i)+50) );
% end
% fclose(fileID);
%%-----------------------distribution----------------------------------%%
% %% based on vertical
% figure
% plot( MeanTempX,y1, '-*', 'LineWidth', 1.5)
% hold on
% set(gca, 'XAxisLocation', 'origin', 'YAxisLocation', 'origin')
% set(gca,'YDir','reverse')
% set(gca, 'Color','none')
% % set(gca,'ytick',[])
% legend('Distribution of winding angle(¡ã)')
% % box off
% hold off
% % [histFreq, histXout] = hist(Cell_mean_Angle_AVE, numOfBins);
% % binWidth = histXout(2)-histXout(1);
% % figure
```

```
% % bar(histXout, histFreq/binWidth/sum(histFreq),'FaceColor','w');
% % hold on
% % PD = fitdist(Cell_mean_Angle_AVE, 'normal');
% % Gau=pdf(PD, histXout);
% % plot(histXout, Gau, '--m','linewidth',2);
% % xlabel('Winding angle(¡ã)')
% % ylabel('Probability density function')
% % legend('Histogram normalisation','Gaussian distribution')
% % hold off

% %% For FEM (structure level)
% Num_hor = 140;  %the number of elements along the horizental in FEM. Input parameter
% Num_ele = Num_hor*Num_Cell_Ver;
% Appro_angle = repmat(MeanTempX,Num_hor,1);
% fname=Imagenamea;
% fname(end-1:end)=[]; % removing .tif from end of file
% save_name=[fname,'_fullangles.txt'];
% fileID = fopen(save_name,'w');
% fprintf(fileID,', 0 \n'); % needed default value for first row in Abaqus
% for i=1:Num_ele
%     if isnan(Appro_angle(i)) == 1
%         Appro_angle(i) = 0;
%     end
%     fprintf(fileID,'%d , %6.2f  \n', i+38688,-(Appro_angle(i)+60) );
% end
% fclose(fileID);

figure
h=histogram(Cell_mean_Angle_AVE,'Normalization', 'pdf');
hold on
pd = fitdist(Cell_mean_Angle,'Normal'); % fit the Normal distribution. NaN removed
x_values = -20:0.01:20;
% A vector with x values of angles which determines the resolution and x limit.
y = pdf(pd,x_values); % y-values for the fitted pdf with all x-values
```

```
plot(x_values,y,'LineWidth',2) % plot of the pdf

%%----------------------------Output-----------------------------------------%%
%%
fprintf('\n')
fprintf(' The resulet of this image is:\n')
fprintf(' Total number of cells = %2.0f\n',No_Cell)
fprintf(' Number of cells vertically = %2.0f\n',Num_Ycell)
fprintf(' Number of cells longitudinally = %2.0f\n',Num_Xcell)
fprintf(' Number of pixels per cell = %2.0f\n',mx/Num_Ycell)
fprintf(' Number of detected fibres by Canny method = %2.0f\n',Totalnum_edge_valid)
fprintf(' Number of fibres measured = %2.0f\n',No_edge)
fprintf(' Number of Valid cell = %2.0f\n',No_valid_Cell)
fprintf(' Number of average fibres per cell = %2.0f\n',No_edge/No_valid_Cell)
fprintf(' Mean angle = %1.3f deg\n',phi_bar)
fprintf(' Mean misalignment angle = %1.3f deg\n',theta_bar)
fprintf(' Maximum misalignment angle = %1.3f deg\n',theta_max)
fprintf(' Standard deviation of angles based on gird = %1.3f deg\n',Std_deva)
% fprintf(' Standard deviation of angles based on identified fibre = %1.3f
deg\n',Std_deva_global)
fprintf('-------------------------------------------------------------\n')
```

APPENDIX B: MATLAB SCRIPT FOR ANALYSING NON-UNIFORM FIBRE DISTRIBUTION IN IMAGES

```
%#########################################################################%
% Written by Songming Qi (Songming.qi@usq.edu.au)
% Characterisation of non-uniform fibre distribution
%#########################################################################%

%% RGB to Gray
clc,clear;close all;
%-----Input Parameter ----------%
Num_Seg = 2;     %% Sepearate the picture with numbers
Sen_Delete = 500;
image = imread('Example.jpg');
% imshow(image)
% title('Original Image');
Iinteg=rgb2gray(image);
[nY,mX] = size(Iinteg);
xdeta =  floor(mX/Num_Seg);
Seg_x = 0:xdeta:(Num_Seg-1)*xdeta;
Seg_x(1)=1;
Seg_x(1+Num_Seg) = mX ;
V_UD = zeros (1,Num_Seg) ;
V_Total = zeros (1,Num_Seg);

for ii=1:Num_Seg
I1 = image(:,Seg_x(ii):Seg_x(ii+1),:);
I =  Iinteg(:,Seg_x(ii):Seg_x(ii+1));
[local_y,local_x] = size (I);
V_Total(ii) = local_y*local_x ;
% bc=imcomplement(BwdFinal);   %%convert
[~,threshold] = edge (I,'Sobel') ;
fudgeFactor = 0.5;
```

```
Bws = edge (I,'Sobel',threshold * fudgeFactor);
%-------Dilate-----------------------------------------------------
se90 = strel('line',2,90);
se0 = strel ('line',11,0);
% se2 = strel ('Disk',10);
Bwsdil = imdilate(Bws,[se0 se90]);
% figure, imshow(Bwsdil)
% title('Dilated Gradient Mask')
Bwdfill = imfill(Bwsdil,'holes');
% figure, imshow(Bwdfill)
% title('Binary Image with Filled Holes')

%---------erode-----------------------------------------------------
seD=strel('diamond',1);
BwdSmooth = imerode(Bwdfill,seD);
BwdSmooth = imerode(BwdSmooth,seD);
% figure,imshow(BwdSmooth)
% title('Segmented Image')

%--------------Delete small area-----------------------------------------
BwdFinal = bwareaopen(Bwdfill,Sen_Delete);
bc=imcomplement(BwdFinal);
bc_temp = bwareaopen(bc,Sen_Delete);
BwdFinal=imcomplement(bc_temp);

%----------------outline------------------------------
figure,imshow(I1)
figure,imshow(labeloverlay(I1,BwdFinal))
%% Regionproperty
% % s = regionprops (BwdFinal,I,{'Centroid','WeightedCentroid'});
% % numObj = numel (s);
% % for k= 1: numObj
% %     plot(s(k).WeightedCentroid(1),s(k).WeightedCentroid(2),'r*')
% %     plot(s(k).Centroid(1),s(k).Centroid(2),'bo')
```

```
% % end
V_UD(ii) = bwarea (BwdFinal);
end

Vf = V_UD./V_Total;
Vf_total = sum(V_UD)/sum(V_Total);
```

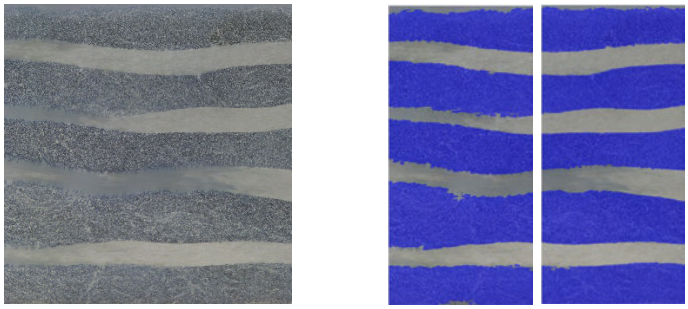

Original Image Processed Image

Figure B.1. An example of analysing images

APPENDIX C: OBSERVED OTHER DEFECTS IN THE COMPOSITE PROFILE

Several defects were observed in the 250 × 100 Joist compared to the standard structure, including dry veil, grooving, and cracks (Figure C.1). Dry veil occurs when a scraping action removes the surface resin in the veil layer, exposing more of the compressed veil and creating the appearance of a dry surface. This phenomenon may be caused by a high compaction rate. Custom build products must not have any visible dry veil, because the dry texture shows through the paint and will result in a cosmetic rejection. Grooving is a defect that can occur during the pultrusion process, rendering the product unacceptable. Consequently, it was crucial to test the mechanical properties of samples with grooving. Coupons were prepared and tested for compression, interlaminar shear, and flexural properties, as shown in Figure C.2.

The dry veil defect had no significant impact on flexural strength. However, it reduced the interlaminar shear strength by approximately 5%. Interestingly, the compression strength increased by about 10% due to the dry veil, as the resin pot was filled with fibre.

The grooving defect negatively affected compression and interlaminar strength, with reductions of 12% and 20%, respectively. On the other hand, the grooving structure positively impacted flexural properties, leading to a 30% increase in strength.

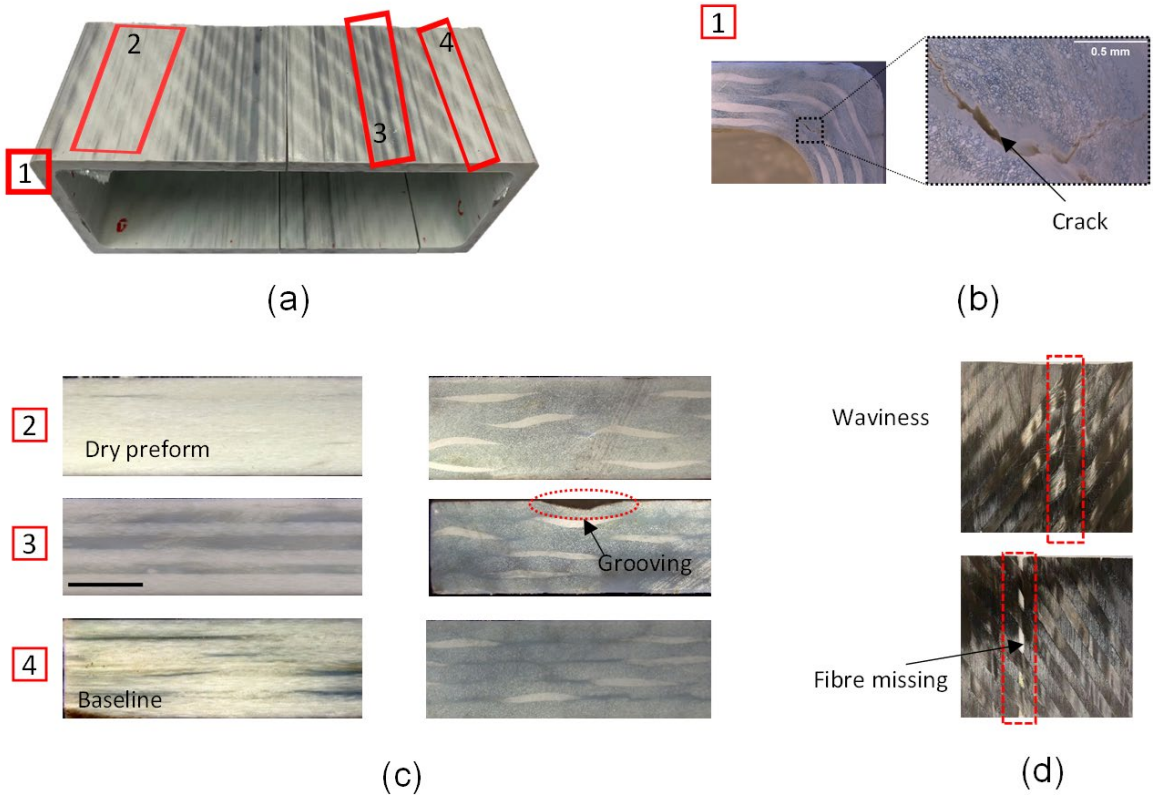

Figure C.1. Observed defects in girder profile.

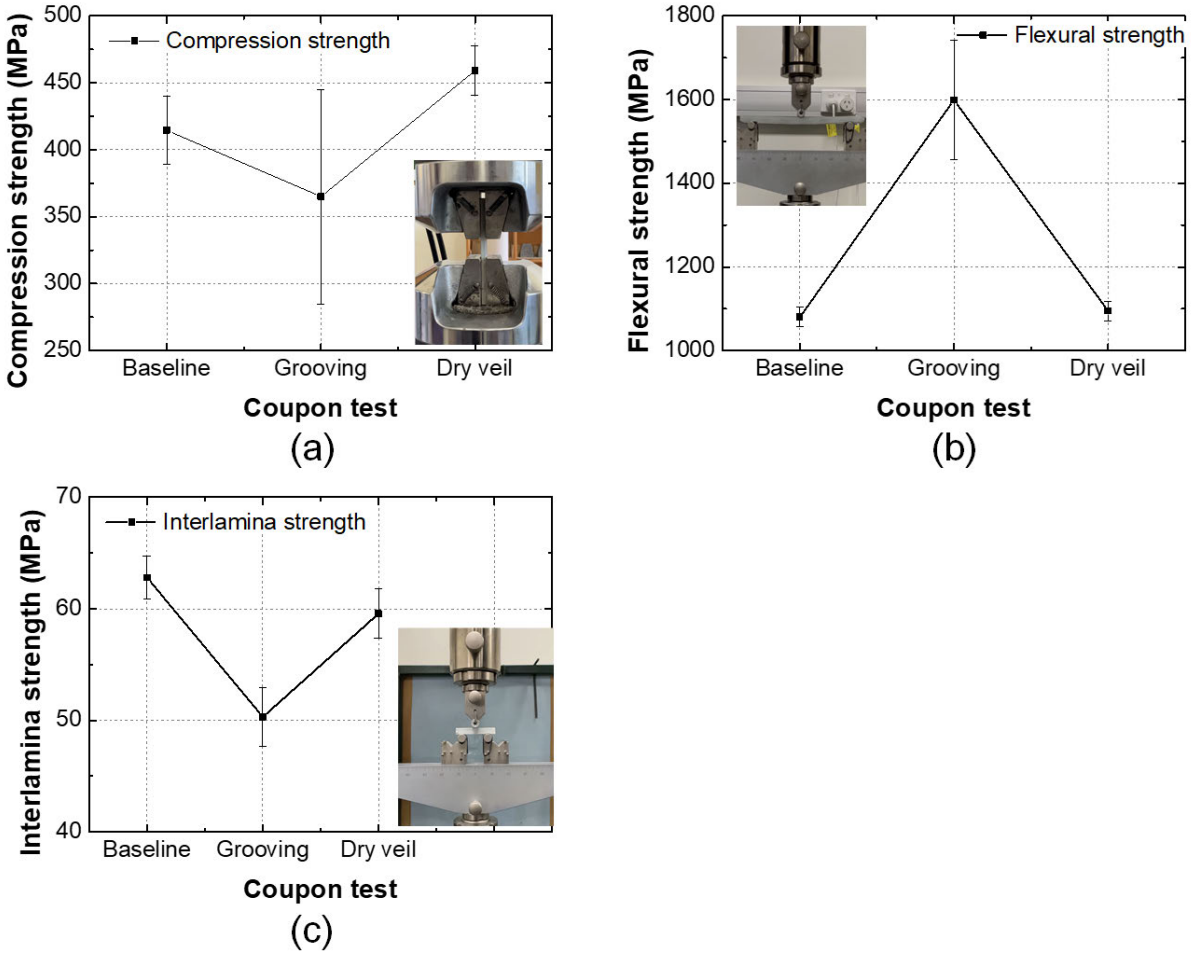

Figure C.2. Coupon test.